UNIVERSITÉ DU LUXEMBOURG

PhD-FSTM-2022-050

The Faculty of Science, Technology and Medicine

DISSERTATION

Presented on 22/04/2022 in Esch-sur-Alzette

to obtain the degree of

DOCTEUR DE L UNIVERSITÉ DU LUXEMBOURG

EN PHYSIQUE

by

Rutuja BHUSARI

Born on 03 May 1992 in Nagpur (India)

METAL-OXIDE NANOSTRUCTURES FOR LOW-POWER GAS SENSORS

Dissertation Defence Committee:

Dr. Renaud LETURCQ, dissertation supervisor

Lead R&T Associate, LIST

Prof. Dr. Ludger WIRTZ, Chairman

Professor, University of Luxembourg

Prof. Dr. Pedro Miguel Cândido BARQUINHA

Professor, NOVA School of Science and Technology (FCT-NOVA)

Prof. Dr. Elisabetta COMINI

Professor, University of Brescia

Prof. Dr. Jean-Pierre RASKIN

Professor, UC Louvain

Affidavit

I hereby confirm that the PhD thesis entitled "Metal-oxide nanostructures for low-power gas sensors" has been written independently and without any other sources than cited.

Esch-sur-Alzette, 20/04/2022 Rutuja BHUSARI

Acknowledgements

We often take for granted the very things that most deserve our gratitude. I was never alone and whatever I have learnt and achieved, was because the following people were with me.

Dr. Renaud Leturcq is the most understanding supervisor I could have asked for. He gave me so much independence to work and yet, very politely, got me back on track the many times I went astray. I have learned technical as well as soft skills from you, which I aspire to inculcate in myself. For Dr. Jean-Sébastien Thomann, I am an adopted PhD candidate. He gave me time, attention, care, and encouragement equal to his own students, no matter how busy he was.

Dr. Emanuele Barborini, for me, is a dedicated group leader and a very good scientist. Cheers to my colleagues Dr. Raoul for the drinks, Dr. Tai for the mandarins and a bite of his lunches, Dr. Joao, Marco, Dr. Sabrina, Dr. Serena, Dr. Rishabh, Shiv, Antoine, Daniel, Julien for being a dynamic group of office mates; Enzo and Vincent for making the chem lab so fun; Lauriane, a colleague who became a good friend; Youri, Naveen, Diana, Poorani, handsome Sir Petru, and all of MRT who made the 4 years fly by so fast and easy.

I would not be here unhurt if it was not for the extreme amount of help from MRT support; Julien, Jérémy. MRT secretariate, Alexis and Corrine were always there to help in administration and other aspects of office. I also had a chance to closely work with Dr. Emmanuel Defay and Prof. Susanne Siebentritt, whom I admire as leaders and who influence me in many ways.

I will always be indebted to Dr. Niranjan Ramgir, my mentor, who gave me a start in the world of nanotechnology and gas sensing.

Thank you, I will forever be grateful.

Family means the world to me, and I am so glad I had a bunch of them.

My little brother, Hrishik; I could come so far away and yet stay so close, because he took the responsibility. My friend and my husband, Dr. Mohit Sood, who accepts me for who I am and at the same time inspires me to be a better person, a better researcher.

Nikhar, who was holding my hand in all the ups and downs; Sangita, who loved me no matter what; Ahilan, who made me look beyond; Maithili, my personal cheerleader and Somita and Kuatuk, who didn't care for what I do as long as I am happy.

To my Luxembourg family for making my life here eventful and happy. Deb, Arpan and Shreyasi, Rohan and Sweta, Sachin and Yamini, Shuklaji and Monikaji, Dipti, Anjali and Deepak, Darshit and Richa, Dinesh, Chanakya, Neha, Apurva, Sourabh, Carolina and the whole of ISAL.

A thank you is not enough to express what you mean to me.

Dedicated to

Dr. Dilip BHUSARI and Dr. Vandana BHUSARI,

Baba and Aai, who believed I would pursue research, even when I didn't

Index

List of Figures

List of Tables

Abstract

For gas sensing applications, metal oxide (MOx) nanostructures have demonstrated attractive properties due their large surface-over-volume ratio, combined with the possibility to use multiple materials and multi-functional properties. For MOx chemiresistive gas sensors, the temperature activated interaction of atmospheric oxygen with MOx surface plays a major role in the sensor kinetics as it leads to oxygen adsorption-desorption reactions, that eventually affects the gas sensing performance. Thus, MOx sensors are operated at high temperatures to achieve the desired sensitivity. This high temperature operation of MOx sensors limits their application in explosive gas detection, reduces the sensor lifetime and causes power consumption. To overcome these drawbacks of MOx sensors, researchers have proposed the use of heterostructures and light activation as alternatives. In this thesis, we aim to develop low power consuming MOx sensors using these solutions.

We show the template-free bottom-up synthesis and shape control of copper hydroxide based nanostructures grown in liquid phase which act as templates for formation of CuO nanostructures. Precise control over the pH of the solution and the reaction temperature lead to intended tuning of the morphology and chemical composition of the nanostructures. We contemplate upon the rationale behind this change in shape and material as CuO nanostructures are further used in a heterostructure.

We discuss synthesis and characterisation of CuO bundles and Cu_2O truncated cubes, former of which lead to very interesting gas sensing properties and application. Devices made from CuO bundles network are investigated for their electrical and oxygen adsorption- desorption properties as a gas sensor. It was observed that the sensor has faster response and recovery in as deposited condition in comparison to annealed sensor. A detailed inspection of response and recovery curves enabled us to derive parameters like time constants, reaction constants and diffusion coefficients for CuO bundles, an analysis that is scarcely performed on p-type materials. Investigation of the derived parameters, role of network junctions and a hydroxylated CuO surface leads us to discuss the hypotheses for the contributing processes. CuO bundles show conduction transients upon exposure to reducing gas H_2 and temperature-based inversion of response upon exposure to reducing gas CO. This has not been reported in literature for CuO exposed to H_2 and/or CO.

We choose ZnO, n-type transducer material, and CuO, p-type materials with lower band gap and higher absorption in the visible range to synthesise a heterostructure. However, sol-gel synthesis of ZnO and CuO nanostructures have different reactions parameters, like temperature, pH, etc., and do not show natural affinity to grow on the other material. These challenges are overcome by implementing a stepped synthesis procedure to fabricate a heterostructure with Cu-based nanoplatelets on ZnO nanorods, also represented

as CuO@ZnO heterostructure in this thesis.

We finally demonstrate electrical and functional characterisation of CuO@ZnO heterostructure. The heterostructure responds differently to tested gasses as compared to its constituent nanostructure ZnO nanorods and a reference CuO nanostructure, CuO bundles. This is an unexpected result as heterostructures usually show response type similar to their base material but with an enhanced sensor response. We present a possible application of e-nose that can differentiate qualitatively between CO, NO_2 and ethanol, using the heterostructure, ZnO nanorods and CuO bundles together.

Introduction

The aim of this introduction is to briefly give an overview of the context of this thesis or what this thesis is about. This is brought about by describing the challenges involved in this work, what questions are posed to researchers in this field, followed by the motivations or why I chose to work on these challenges. This thought process leads to defining clear objectives of this thesis, personifying what I planned to achieve through the course of this work. The last part of the introduction will provide the reader with a structure of the thesis describing how the work is presented here.

0.1 Context (*What is this thesis about?*)

Rapid industrialisation has led to emission of many gasses into the environment. In most cases, these gasses are harmful to human health in the short or long term. The gases produced could either be a by product of an industrial reaction or an end result of a processing step in a product assembly line. Nevertheless, it calls for monitoring of air quality and gases in both, indoor and outdoor environment [1].

In commercial applications, gas chromatographs are still used to map indoor air quality. Gas chromatograph is accurate does not allow real time measurement and are bulky instruments. These act as drawbacks of this technique. Researchers and material scientists have come up with a variety of gas sensors based on optics, mechanics, electromagnetics, electronics and electrochemistry in the past half century. Each technique has its advantages, disadvantages and particular applications. We choose to study electronic sensors, specifically chemiresistive sensors, in this thesis.

Chemiresistive sensors are generally cheaper to fabricate and easy to integrate into integrated circuits compared to other types of gas sensors [2]. Various materials like metal oxides (MOx), polymers, carbon nanotubes etc., have been studied as chemiresistive gas sensor materials in literature [3]. However, in this work, we concentrate on MOx for their use as chemiresistive gas sensors. MOx are attractive for use in sensors as they are easily integrated into microelectronic systems and have displayed high stability. In

terms of performance, MOx based sensors are also characterised with large and quick response along with robustness. They are, however, limited to high temperature operation. Other than this disadvantage, MOx based sensors also suffer from drifts and inefficiency on long exposures to humidity [4].

MOx based sensors can be based on thin film or nanostructure. Researchers have found that nanostructure based MOx sensors of the same material performed better than a thin film based sensor as it has larger surface area to volume ratio, which allows for a greater amount of oxygen adsorption [1]. Taking this lead from previous research, we strictly concentrate only on nanostructure based MOx sensors in this work. Sensors can be prepared using various physical and chemicals techniques. However, due to it's reproducibility, low cost and ease of up-scaling, we choose to fabricate MOx nanostructure sensors using sol-gel synthesis [2].

The working principle of chemiresistive gas sensor, as the name suggest, is the change of resistance due to chemical redox reactions, and is based on Ohm's law, $V = I * R$. The oxygen in the atmosphere reacts with the MOx surface causing electrical changes in the material. Since the atmospheric oxygen is largely stable, external energy needs to be provided for it to dissociate and interact with the MOx surface. Traditionally, this energy is provided in terms of heat in chemiresistive sensors. Heat provides activation energy for oxygen adsorption reaction to occur as well as facilitate reaction rates of test gases that are temperature-dependent [5, 2]. Chemiresistive sensors are known to operate at high temperatures like 150 °C to 400 °C for optimal performance.

With this context, we can move to the motivation of this work.

0.2 Motivation (*Why did I invest 4 years of my life in this?*)

The high temperature operation of chemiresistive MOx sensors leads to various disadvantages like reduced lifetime, limitation in application for detection of explosive gasses and majorly, consumption of power for continuous heating [5]. Due to the miniaturisation of electronics and the upcoming energy crisis, there is a drive in research to achieve low power gas sensing. Low power consumption of gas sensors is quite necessary for a sustainable technology and a pre-requisite for the development of autonomous devices like wireless sensors or Internet of Things devices [6] To overcome this disadvantage of chemiresistive MOx sensors, researchers have worked on many aspects like using porous nanostructures, doping of MOx, using heterostructures, light activation, etc [2]. Of these various pathways, we choose to examine in detail, effect of using a heterostructures along with light activation to achieve low power MOx gas sensors.

Heterostructures are known to make use of junction effects to lower the operating temperature of chemiresistive gas sensors or to improve sensitivity based on catalytic effects [2]. Light is known to replace

heat as a source of excess charge carries in a semiconductor gas sensor. However, if a sensor operates with UV light, extra power will be required to generate the UV light for efficient sensing. This does not solve the power consumption issue. It, thus, becomes crucial to work on visible light activated gas sensors.

0.3 Challenges (*What questions do I want to answer?*)

It is also important to understand how the material reacts with various conditions such as the temperature of sensor, presence or absence of oxygen, certain target gas and its concentration, surrounding irradiation, etc. It is imperative to know how it affects the current passing through material and how these factors affect its gas sensing properties. This is not the same for all the materials and thus, a broad topic of study and discussion, making it a necessity to determine whether a material can be used as a gas sensor or not. Researchers have worked on presenting hypotheses to explain various mechanisms. However, the challenge is to correctly identify the mechanism taking place in a sensor using literature and relevant experiments.

Correct identification of mechanisms will enable a researcher to fine-tune properties of the material and to identify suitable conditions to improve the 3S of gas sensing: Sensitivity, Selectivity and Stability.

Though it might seem simple, achieving heterostructures at nanoscale is not that straightforward. Synthesis procedures of different material nanostructures have extremely different reaction conditions that can vary in temperature, pH, stirring conditions or even equipment. There are two ways that a heterostructure can be synthesised by combining two different procedures, one step approach or a two step approach. For a one step synthesis approach, there must be a way to combine the synthesis procedure of two different material nanostructures in one equipment at similar working conditions. For a two step approach to the formation of the heterostructure, it would be important for one of the materials to have a natural affinity to grow on another or there needs to be an intermediate step that creates affinity for natural growth of second nanostructure material on the first nanostructure material. This is a major synthesis challenge to overcome.

Another major challenge is to incorporate light activation. Since different materials have different band gap, they absorb light at different wavelengths. Large band gap materials will absorb light at UV wavelengths or higher. Thus, to focus on visible light activated sensing, we work with lower band gap materials.

With the context, motivation and challenges in mind, let us get to know the objectives of this thesis.

0.4 Objectives (*What had I planned to achieve?*)

A summary of the objective of this thesis are as follows:

- A deeper understanding of what constitutes response and recovery in MOx chemiresistive gas sensors,
- Synthesise heterostructure in nanoscale and its characterisation and
- To achieve low power gas sensing with the help of heterostructure and light activation.

In this work, we analyse in detail the oxygen adsorption and desorption characteristics in p-type MOx, copper oxide (CuO), to achieve the first objective. We attempt to relate physical processes or hypotheses involved in gas sensing to experimentally derived parameters. With the help of sol gel synthesis and many references from literature, we achieve the second objective by synthesising a novel heterostructure combining zinc oxide (ZnO) and CuO nanostructures. In the process, of obtaining these heterostructures, we go through steps of obtaining various Zn based and Cu based individual nanostructures, which are also analysed in this thesis.

It is important to characterise the nanostructure materials and to ensure that there is a physical junction between two materials, through which charge flow can occur for a heterostructure. After material characterisation, we test the nanostructures for electrical conductivity and gas sensing properties.

To achieve the last objective, the achievement of first two objectives is imperative. We perform various gas sensing tests and do a comparative study on the role of heterostructure and light activation in sensing performance.

0.5 Structure of the thesis (*And how did I do it?*)

The thesis is structured as follows:

Chapter 1 includes fundamentals of gas sensing, heterostructures and light activation. Basics of gas sensing are explained here with schematics to create a background of understanding. The sections on heterostructure and light activation explain these phenomena and have a dedicated subsection for state-of-the-art examples of work done in this field previously. This is an important chapter to start with to fully understand the terminologies used in this thesis as well the achievements of this work.

Chapter 2 encompasses all the materials and equipment used in the various procedures mentioned in the thesis. This is not a glossary of equipment and their basic working principles. But rather a description of exactly how or with what specifications each of these materials and equipment were used in this work. This

chapter also describes in detail the gas sensing test bench set up at LIST. This set up was assembled during the course of this work and is essential towards functional characterisation of the materials synthesised.

Chapter 3 consists of the synthesis procedures of the various nanostructures obtained during the course of this work in detailed steps. Along with this, morphological, optical, structural and elemental characterisation performed on the nanostructures are also elaborated in this chapter. The chapter is roughly divided into two sub parts, one detailing simple nanostructures, while the other detailing heterostructures. The synthesis procedures used are sometimes as described in literature, modified versions of literature recipes or completely new procedures. A small part of the chapter is also dedicated to understanding the evolution Cu based nanostructures from a common starting point.

Chapter 4 constitutes of electrical and functional characterisation of CuO bundles nanostructure. Current-Voltage characteristics and gas sensing properties of CuO bundles nanostructure network are discussed in detail in this chapter. A dedicated discussion is presented on the response and recovery curves and their relation to physical processes that occur at the gas sensor surface. Performance of CuO bundles network is tested in presence of reducing gasses H_2 and CO.

Similar to chapter 4, chapter 5 incorporates current-voltage characteristics and gas sensing properties of CuO@ZnO heterostructure synthesised during this work. We present the electrical characterisation in comparison to ZnO NRs as they form the base of the heterostructure. The gas sensing characteristics are tested in presence of oxidising gasses like O_2 and NO_2 along with reducing gasses like H_2, CO and ethanol. To gauge the performance of the heterostructure, we compare the gas sensing properties with ZnO NRs and CuO bundles in similar working conditions.

Chapter 6 concludes this work with a few take away points and enlists the biggest achievements of this work. This chapter also gives an outlook into the future and mentions open avenues for exploring.

This brief introduction to the reader can act as a guide to browse through specific topics of interest and also serve the purpose of a reminder of what is to be expected in the following text. Throughout the text two fonts are used to differentiate between the texts. Latin Modern Roman is used for the overall text written originally for this thesis while Computer Modern Roman is used for the text adapted from various articles that are published or submitted a result of this work. The text and figures from the publications are either directly used or modified slightly based on compatibility requirements of the thesis.

Chapter 1

Fundamentals of Gas sensing, Heterostructures and Light activation

The aim of this chapter is to provide the reader with sufficient background and literature to have a better understanding of the work that will be presented in the rest of the thesis. This chapter will endeavour to very briefly represent the fundamentals of gas sensing and the state-of-the-art in the field of MOx based chemiresistive sensors. In the fundamentals, generally accepted working principles of n-type and p-type MOx sensors are described along with an example of typical gas sensing curve. For the state-of-the-art, we concentrate on ZnO and CuO based sensors. The choice of these materials is justified later on. In the second subsection, the concept of heterostructures is introduced emphasising how they overcome the shortcomings of single MOx senors. Here too, the state-of-the-art is presented for heterostructures, primarily based on ZnO and CuO. In the final subsection of this article, we motivate use of light activation by presenting a detailed working principle and explaining how light activation could overcome the disadvantages posed by high operating temperature based MOx sensors. We also present state-of-the-art for ZnO and CuO based light activated sensors. The information in this chapter should, thus, help the reader assess the novelty of the work presented and recognize the challenges overcome during the course of this work.

Various parts of this chapter are included in a published review article [7].

1.1 Gas sensing - Basic principles

Gas sensing principles are widely discussed and based on different individual material specific investigations where researchers have provided hypothesis for the same [8, 9, 10]. For details of physical mechanisms

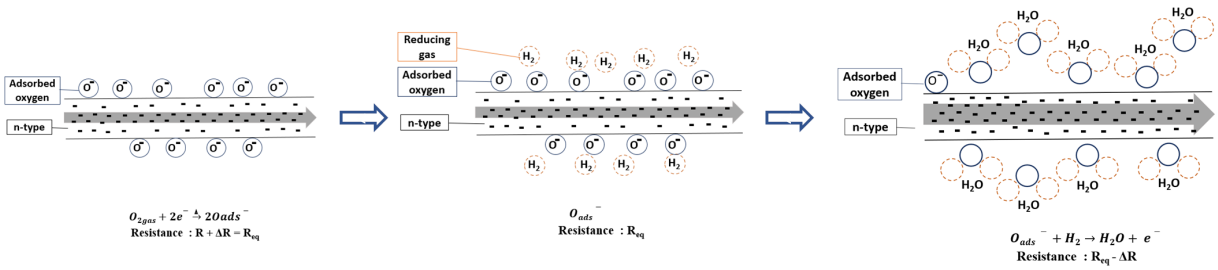

Figure 1.1: Schematic representation of simplified working of n-type of MOx chemiresistive sensor a) n-type MOx in air, b) n-type MOx in air, reducing gas introduced in environment, c) n-type MOx in presence of reducing gas. "-" represents electrons as the majority carriers, gray arrow represents the overall conductance through the material.

underpinning in nanostructure MOx gas sensors, readers can refer to [7]. In the following subsection, however, we concentrate on a simplified version of the basic sensing mechanism widely accepted by the scientific community, to strengthen our understanding of the working of MOx gas sensors.

1.1.1 Metal oxide chemisresistive gas sensors

The operation of chemiresistive gas sensors can be described in terms of two functions, namely receptor and transducer. The ability of the MOx surface to react with the target gas depends on the properties of the surface and the oxygen species adsorbed on the surface. This is also known as the receptor function. The transducer function is the ability of the material to convert this interaction of surface and gases into an electrically measurable signal. A material converts the chemical interaction into an equivalent electrical signal with the help of work function changes.

As a reminder, the working principle of chemiresistive gas sensor is the change in resistance due to chemical redox reactions and is based on the Ohm's law, $V = I * R$. When a target gas interacts with the oxygen adsorbed or with the elements on the surface of a chemiresistive sensor, there occurs a reaction. This leads to change in the resistance of the material. This change in resistance is recorded and indicated as detection of gas in the atmosphere. Since we will be studying specifically MOx based chemiresistive sensors in this thesis, its imperative to know their working in detail.

MOx are semiconductors in nature. Hence, they can be classified as n-type or p-type based on the majority charge carriers they have. The working of n-type and p-type MOx chemiresistive gas sensors is schematically represented in fig. 1.1 and fig. 1.2, respectively. When a n-type MOx is in an oxygen environment, oxygen adsorbs on the surface of the MOx by taking an electron from it. This leads to a reduction in the electron density in the MOx, and the resistance of the MOx increases. If a reducing gas

is introduced in this environment, like hydrogen (H_2), it reacts with the adsorbed oxygen to form H_2O, and the electron is returned to the MOx. This leads to a decrease in resistance and increase in current flowing through the MOx. This change in resistance or current, also known as response, is observed to detect the presence of gas in an environment. In most cases, the change in current flowing through the MOx is proportional to the change in the concentration of reducing gas present in the environment. When the reducing gas is no longer in the environment around the MOx, the atmospheric oxygen re-adsorbs on the surface, causing the resistance to increase and current to decrease. This is known as the recovery of the gas sensor.

There are different species of oxygen that adsorb on the surface of a MOx at various operating temperatures and participate in gas sensing reaction. Let's take an example of ZnO based sensor. The following equations adapted from [11], are generally accepted scenarios of ZnO based sensor, where equation 1.1 occurs at room temperature while equation 1.2 occurs at higher operating temperatures like 300 °C - 400 °C.

$$O_{2(g)} + 2e^- \longleftrightarrow 2O^-_{ads} \tag{1.1}$$

$$O_{2(g)} + 2e^- \longleftrightarrow O^{2-}_{ads} \tag{1.2}$$

Change in resistance of MOx due to the above equations also depends on the size of the MOx nanostructure. If the size of the nanostructure is comparable to the Debye length, then the change in resistance will occur in the bulk of the material. If the size of the nanostructure is much larger than Debye length, then a surface depletion region is formed where the oxygen species is adsorbed. These intricate details and case studies are explained in [2, 7].

When a reducing gas, like H_2, comes in contact with the MOx surface, the following reactions may occur based on what species of oxygen is adsorbed on the MOx surface.

$$H_{2(g)} + O^-_{ads} \rightarrow H_2O_{(g)} + e^- \tag{1.3}$$

$$2H_{2(g)} + O^{2-}_{ads} \rightarrow 2H_2O_{(g)} + 2e^- \tag{1.4}$$

The electron on the right side of these reactions is given back to MOx, changing its conductance.

An almost similar process occurs in p-type of MOx. Here, when oxygen adsorbs on the MOx surface, in the process of taking an electron, a hole is generated in the MOx. This leads to decrease in resistance

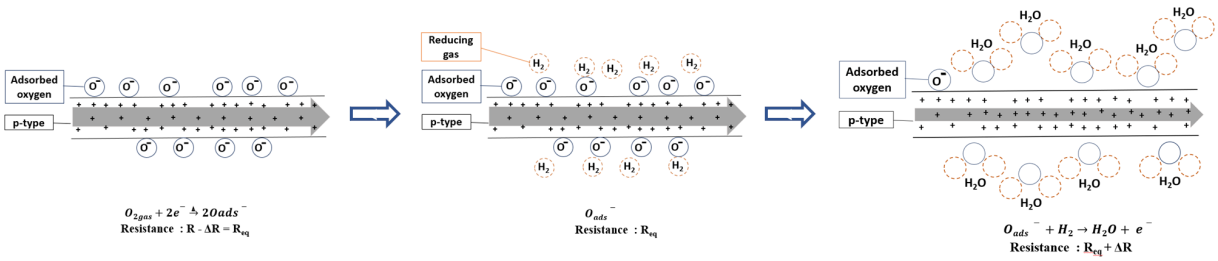

Figure 1.2: Schematic representation of simplified working of p-type of MOx chemiresistive sensor a) p-type MOx in air, b) p-type MOx in air, reducing gas introduced in environment, c) p-type MOx in presence of reducing gas. "+" represents holes as the majority carriers, gray arrow represents the overall conductance through the material.

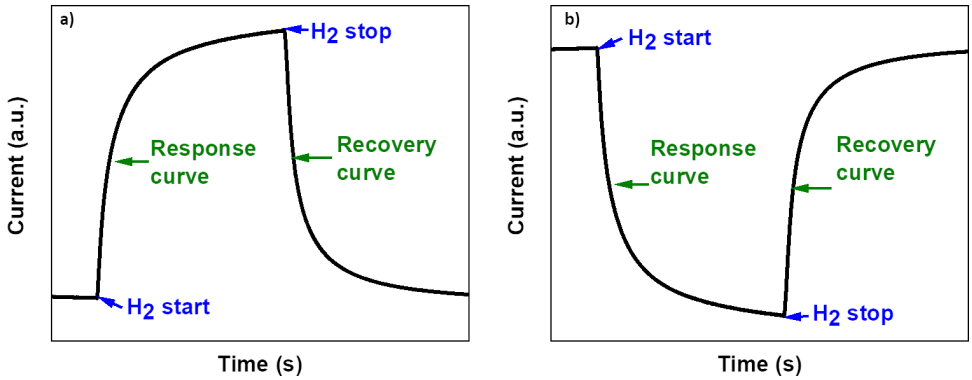

Figure 1.3: An example of typical response of a chemiresistive gas sensors a) n-type of MOx in presence of reducing gas (H_2), b) p-type of MOx in presence of reducing gas (H_2)

and increase in current through the MOx. In the presence of a reducing gas like H_2, when H_2 reacts with oxygen, a electron is given back to the MOx, increasing the resistance and reducing the current flowing through it. An example of the sensor response is shown in fig. 1.3, with fig. 1.3a corresponding to sensor response of n-type MOx to reducing gas and fig. 1.3b corresponding to sensor response of p-type MOx to reducing gas.

Some important terminologies, are worth describing here. Sensor response (SR) is a ratio of the change in current taking place in presence of a target gas. There are multiple ways of calculating the SR. In this thesis, we use the following definition throughout. For an n-type MOx in presence of a reducing target gas,

$$SR = \frac{I_g}{I_{air}} \tag{1.5}$$

while for a p-type of MOx,

$$SR = \frac{I_{air}}{I_g} \tag{1.6}$$

and vise-a-versa for oxidising target gas. Here, I_g is saturation current flowing through the gas sensor in the presence of target gas and I_{air} current flowing through the gas sensor in air or base gas. For an n-type MOx sensors, response time is the time taken by the current flowing through the gas sensor to reach 90% of it's steady state value in the presence of a target gas. Similarly, for an n-type MOx sensors, recovery time is defined as the time taken by the current in the gas sensor to reach 10% of it's steady state value in the presence of base gas or air during the recovery of the sensor.

1.1.2 Materials for metal oxide gas sensors

From a variety of n- and p-type MOx available, we decide to work on ZnO, n-type MOx, and CuO, p-type MOx, for our work in this thesis. ZnO is a known and well-studied material that has tunable nanostructure growth possibility and offers good electrical conductivity as well as sensitivity to most gases[1]. However, ZnO based sensors operate at high temperatures and the ones that operate at low temperatures generally require UV light activation [12]. Gas sensing applications of CuO are far less explored than ZnO and CuO absorbs light in the visible wavelength [13]. With an aim to develop low power consuming light activated sensors, we choose to work on combining ZnO and CuO into a heterostructure. With this motivation of the choice of materials, let us understand them in detail and the research already done on these materials, below. It is imperative to note that the literature presented below is restricted to nanostructures only.

State-of-the-art on ZnO based gas sensors

Various n-type MOx like SnO_2, ZnO, WO_3, TiO_2 etc. have been studied in the literature for their gas sensing applications. However, ZnO has been found to be an important multi-functional semiconductor due to its following properties, some of which are listed below.

ZnO has a reported wide band gap of 3.37 eV and a large exciton binding energy of 60 meV, which can be slightly different based on the morphology of the nanostructure. ZnO is also reported to have a high hall mobility of 200 $cm^2v^{-1}s^{-1}$ at room temperature. Due to it's excellent electrical properties, it is used in various applications like gas sensors, light emitting diodes, solar cells, piezo-electronic and magneto-strictive devices, conductive transparent optics, etc. ZnO also presents an opportunity to work with various nanostructure morphologies including nanoparticles, NWs, nanorods, arrays, mesoporous particles, nanoflakes, and many more [1].

In terms of gas sensing material, ZnO exhibits sensitivity to multiple gasses, good electrical conductivity,

long term stability and repeatability of gas sensing properties. However, ZnO is also riddled with some disadvantages like lack of selectivity, high temperature operation, which are common to all n-type MOx, along with quick degradation on exposure to humidity. Researchers are working on ZnO as a gas sensing material for more than half a century now and are implementing various techniques like doping, synthesis of various morphologies, heterostructures, use of UV light, and many more to overcome these disadvantages [1].

The following state-of-the-art is some of the most recent work done on ZnO nanostructures as gas sensors and an inspiration for the work done in this thesis. However, the reader can refer to some review articles on this subject [14, 15, 16, 17, 18].

Work done by N. Caicedo on ZnO nanorods networks acts as a starting reference for this thesis [19]. Caicedo worked on developing a recipe to synthesize ZnO nanorods in solution. She tested various deposition techniques and post deposition treatment on these ZnO nanorods. She further tested a network of ZnO nanorods and observed the effect of the performed post deposition treatments on the sensing properties [20].

When we talk about novel morphologies that are possible with ZnO, work done by Kumar *et al.* needs a mention. Through single step thermal decomposition reaction, they developed a ZnO nano lily bud garden. This sensor displayed a highly selective response and a maximum sensitivity of 178 at 180 °C to 80 ppm of H_2. This ZnO sensor had a fast response time of 1-2 s while the recovery was roughly 45-50 s. The authors hypothesise that a rough network and availability of large surface area could lead to increased gas phase interactions and lead to such a high and quick response to H_2 [21].

Wang *et al.* prepared NO_2 gas sensors based on ZnO nanorod arrays, which is able to detect 1 - 50 ppm of NO_2 when operated at 200 °C - 225 °C [22]. However, nanostructures are shown to offer greater sensitivity at much lower temperatures, which has inspired researchers to investigate them more in recent times. Using this idea, Zubair *et al.* have experimented with various ZnO morphologies to create ZnO based sensors that are able to detect 10 ppm NH_3 at room temperature [23]. Similarly, Cardoza-Contreras MN *et al.* also developed room temperature operating ZnO single NW sensors which can detect H_2 at low concentration of 121 ppm [24].

Researchers have also worked on developing ZnO based gas sensors for organic complex gasses. Huang *et al.* worked with macro-mesoporous ZnO nanostructures to make sensors selective to acetone showing sensor response to concentration as low as 10 ppm with optimum operating temperature of 300 °C [25]. Ge *et al.* also presented similar work with porous ZnO microspheres being sensitive to the lowest 5 ppm of acetone, methanol and ethanol at 330 °C [26]. Both claimed that the high surface area due to porous nanostructures is the reason for achieving this high sensitivity at low gas concentrations.

State-of-the-art on CuO based gas sensors

Among MOx chemiresistive gas sensors, p-type MOx are less investigated as they show lower sensor response compared to n-type MOx. Despite that, p-type MOx provides various other benefits over n-type MOx like better stability of sensor response in humidity [27]. It is also known that p-type MOx adsorbs more oxygen on their surface compared to n-type MOx, which is critical when it comes to sensitivity of a gas sensor [27]. P-type MOx also have an advantage of providing catalytic effect in gas sensing due to its multiple oxidation states [28]. P-type MOx are good catalysts in promoting selective oxidation of various volatile organic compounds making them easier to detect [29].

CuO is a well known p-type semiconductor with a narrow band gap of 1.2 - 2.16 eV [30]. It has been found in the literature that nanostructure morphology affects this band gap [29]. Other than gas sensing, CuO nanostructures are also used in biomedical applications because of their antimicrobial and biocidal properties [31]. Due to its characteristic electrical, optical and magnetic properties, CuO is also widely used in supercapacitors, filters, magnetic storage media, catalysts, cosmetics and microelectronics [32]. Moreover, CuO nanostructures are an effective catalyst for CO and H_2S oxidation as well as in the oxidation of volatile organic chemicals (VOCs) such as methanol [33, 34, 29].

Cuprous oxide (Cu_2O), a Cu based oxide, is a widely used p-type semiconductor material having contrasting optical properties, crystal structures, electrical and physical properties in comparison with CuO. Cu_2O is expected to have a direct forbidden band gap of 2.17 eV in bulk, while CuO has a direct band gap of 1.2 eV in bulk. However, CuO is considered to be more stable than Cu_2O because Cu(II) ions are more stable in ambiance, making CuO important in practical sensor applications [35, 36, 37].

Table 1.1: CuO nanostructures for gas sensing

Sr. No.	Morphology	Synthesis Technique	Target gas	Temperature	Working principle	Ref.
1.	NRs	hydrothermal	ethanol (1-2000 ppm)	RT	surface accumulation conduction	[38]
2.	NW arrays	heating the copper foil in air	H_2S (500 ppb)	160 °C	-	[39]
3.	porous NWs	deposition of Cu on porous SWNT	H_2	250 °C	interaction of H_2 with preadsorbed oxygen species	[40]
4.	nanotubes and nanocubes	Cu NW oxidation and Cu2O nanocubes oxidation	CO (50 - 1000 ppm)	NTs 175 °C + NCs 250 °C	interaction of gas with preadsorbed oxygen species at high temp	[41]
5.	NPs	hydrothermal reducing process and a thermal oxidation	H_2S (0.2 ppb)	19.85 °C	pores may act as channels for gas dispersion	[36]
6.	NWs	chemical solution (SCS approach)	H_2 (100 ppm)	300 °C	persolating phase transition from CuO to Cu	[42]
7.	NWs	thermal oxidation of Cu thin film	butanol (10-30 ppm)	300 °C	conductometric sensing mechanism	[37]
8.	NRs ($+Cu(OH)_2$)	hydothermal + oxidation	NO_2	-	piezoresistive readout using cantilever (not material specific)	[43]
9.	NWs	thermal oxidation of Cu film	CO (1 to 30 ppm)	325 °C	adsorption/desorption kinetics	[33]
10.	Npowders urchin-like	microwave-assisted hydrothermal method	H_2	200 - 400 °C	reaction with oxygen (adsorbed or lattice)	[44]

Due to the variety of applications of CuO nanostructures, it is difficult to find review articles dedicated its application in gas sensing. Most review articles like [35, 45, 46] talk about CuO nanostructure synthesis, its properties and a variety of its possible applications, including gas sensing. Some recent reviews though, like [47] talk about p-type gas sensor materials in general while [48, 49] specifically talk about CuO nanostructures in gas sensing applications. However, in this section, we talk about only some pioneering work done on CuO nanostructures in gas sensing applications which forms a base reference for our work. The readers can refer to the above mentioned review articles for more details.

Volanti *et al.* have performed an extensive analysis of CuO nanostructures as gas sensors responding to 5% H_2 at 400 °C using insitu XPS and gas sensing measurements. They study the effect of carrier gasses, N_2 and air, on the oxidation state of CuO nanostructures and response to a reducing gas H_2 [44]. Nyugen *et al.* have also developed a porous CuO NWs based gas sensor with the capability of detecting 6% H_2 at an operating temperature of 250 °C [40]. Similar work has been done by Lupan *et al.* , where they develop CuO NWs based sensor operating at 300 °C with the detection limit of 100 ppm H_2 [42].

CuO is known to have particular affinity for H_2S gas detection. When CuO, a MOx semiconductor, reacts with H_2S, CuS, a metal, is formed. The resistance of the sensor film is drastically affected when parts of semiconductor are changed to metal allowing a very sensitive detection of H_2S. This reaction is reversible and CuS converts back to CuO in air. Chen *et al.* developed a "chemical sensor based on vertically aligned CuO NW array constructed by insitu SEM micromanipulation". This sensor was investigated for its H_2S sensing properties and showed a detection limit as low as 500 ppb operating at 160 °C. The authors employed different sensing mechanisms to explain the detection at high and low gas concentrations. When the sensor was exposed to concentration higher than 5 ppm of H_2S, the surface reaction caused a layer of CuS, resulting in increased conductivity. In addition to this, the sensor was selective to H_2S when compared with H_2, CO, and NH_3 [39]. Li *et al.* also developed CuO nanoparticle based selective H_2S sensor with sub-ppb level detection operating at roughly room temperature and based on a similar working principle [36].

Steinhouer *et al.* studied CuO NWs as CO gas sensors with optimal operating temperature of 325 °C and detection range of roughly 1 - 30 ppm. They observed that sensor response drastically reduces upon exposure to humidity and concluded that it could be so due to surface hydroxylation [33]. Hou *et al.* also worked to develop a CuO nanotube sensor for CO detection with a little lower operating temperature of 175 °C and the lowest detection limit of 50 ppm CO. They observed that CuO nanotube sensor was highly selective to CO [41].

Work has also been done on using CuO based gas sensors for the detection of organic vapours. Wang *et al.* presented CuO nanorod based sensor device operating at 300 °C which was able to detect 2000

ppm of ethanol with 25% relative humidity. The authors explained the sensing mechanism to be surface accumulation conduction [38]. Mazhar *et al.* went a few steps further to develop a CuO NW based device also operating at 300 °C, but, which was able to detect lowest 10 ppm of butanol and 5 ppm of ethanol. Mazhar *et al.* also observed that there was no significant effect of relative humidity on the Kelvin Probe measurements [37].

1.2 Heterostructures

Parts of the following section are taken from my co-authored article [7] and are differentiated from the rest of the text by use of 'computer modern' font.

Miller et al. define heterojunction as a physical interface between two dissimilar materials and a heterostructure as one that incorporates all three, two dissimilar materials and a heterojunction between them [2]. Dissimilar materials, as specified by the name, will have different band gap and thus different Fermi levels. At a heterojunction, there is an exchange of charge carriers which leads to Fermi level adjustment between the two dissimilar materials. Heterostructures can be MOx-MOx or metal-MOx. We consider only MOx-MOx heterostructures in detail.

Use of heterostructures is known to offer many advantages in enhancing the sensitivity and selectivity of gas sensors, reducing operating temperature, being prone to light activation, etc. These advantages are due to synergic physical effects arising by the combination of dissimilar materials. For example, in a heterostructure, the receptor and transducer functions can be separately optimised by choosing a receptor MOx having an affinity for adsorption [50], reaction [34] or degradation of a target gas [29] while the materials used for optimising the transducer function should have tuneable charge transport characteristics [2]. The difference in bang gap and Fermi energy levels of dissimilar materials can enhance charge carrier separation, which in turn increases the charge carrier lifetime and allows them to participate in chemical reactions at MOx surface. This effect is predominantly utilised when heterostructures are used in combination with light activation [51], as described in the next section.

1.2.1 Understanding popular heterostructure based gas sensing mechanism

Researchers have proposed two conduction models for heterostructures, viz. the conduction channel model and the potential energy barrier model. Examples of both the models are schematically represented in fig. 1.4.

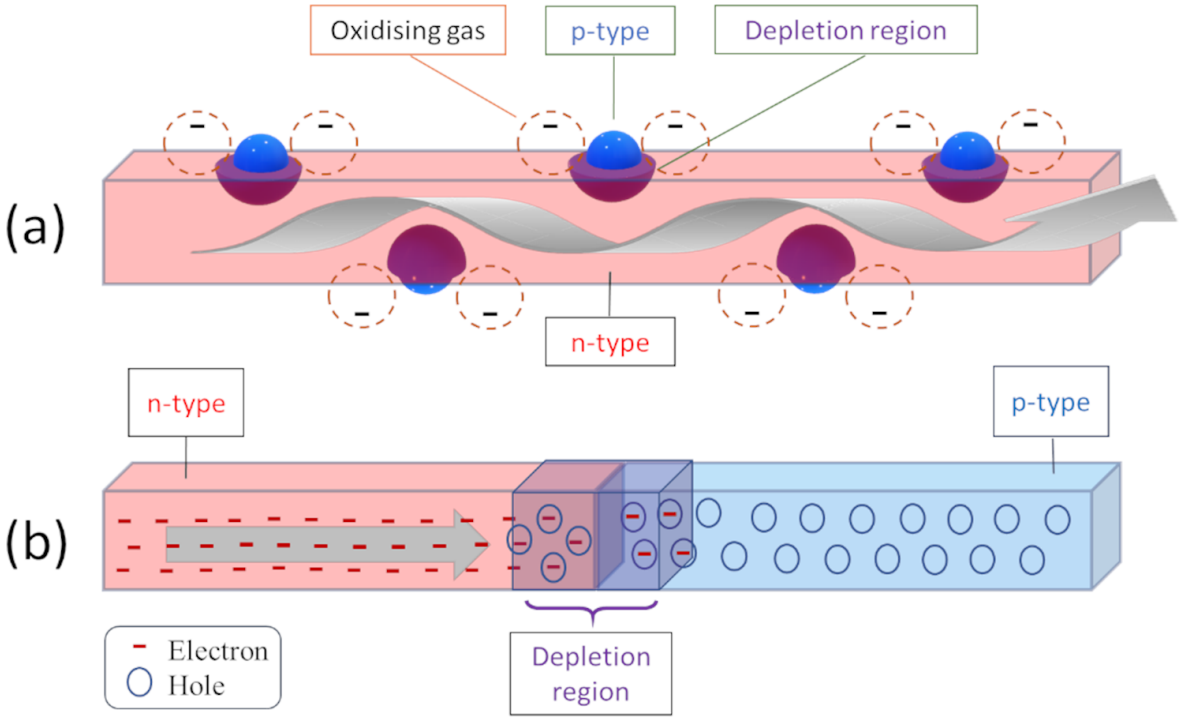

Figure 1.4: Schematic representation of (a) conduction channel mechanism (b) potential energy barrier mechanism of gas sensing in MOx-MOx heterostructures. Red area represents n-type MOx while blue area represents p-type MOx. The depletion region is represented by purple or a mixture of red and blue. Gray arrows represent the current flow through the device. Orange coloured dashed empty circles are representative of adsorbed oxygen in (a). "-" represents electrons and small circles represent holes as described in the legend

In the conduction channel mechanism, as shown in Figure 1.4 (a), the depletion or accumulation region formed at the heterojunction impinges on the conduction channel through the primary MOx with transducer function. Here, it is assumed that the movement of charge carriers is taking place in the bulk of the transducer-MOx and thus forms a conduction channel. When another MOx nanostructure is in contact with the transducer-MOx, depending on its majority carriers, a depletion or an accumulation region is formed at the interface or at the heterojunction. If the dimensions of this transducer-MOx nanostructure are comparable to twice the Debye length, any changes in the width of the depletion or accumulation region will have a direct effect on the amount of current flowing through the device. These changes occur due to oxygen adsorption and desorption along the surface of the heterostructure [52, 53].

The typical response type for such a heterostructure will be qualitatively the same as the response type of the primary MOx. However, due to the addition of the secondary MOx, the overall sensitivity of the

heterostructure towards the target gas is expected to increase, resulting in a larger response as compared to that of the primary MOx alone. This has been well demonstrated in the literature [54, 55, 56]

When two dissimilar materials form a heterojunction in such a way that the junction comes directly in between the pathway of current flow, a diode type junction is formed, as shown in Figure 1.4 (b). When this occurs at grain boundaries of similar type of MOx, e.g. n-n or p-p, a double Schottky barrier is formed at each boundary. Similar to the grain boundary model, the junction or a double Schottky barrier dominates the resistance of the heterostructure as charge carriers must overcome this barrier. Changes in the adsorbed oxygen on the surface of the heterostructures on either side of the heterojunction modulate the charge depletion region and thus modulate the current passing through the device [57, 58].

The response type of the heterostructure is difficult to predict in this case. There can be three possibilities; (i) electrons dominate as charge carriers through the heterostructure and the response is similar to n-type MOx; (ii) holes dominate as charge carriers through the heterostructure and the response is similar to p-type MOx; and (iii) the response is junction dominated or depletion layer dominated. In the first two possibilities, the MOx with less doping will be more sensitive towards changes in conduction due to adsorption and desorption of oxygen, while MOx with higher doping will determine the type of charge carriers. in the third possibility, the overall conduction through the heterostructure can be assumed to be dependent on the tunneling current through the depletion region. The barrier height faced by this tunneling current will be modulated due to oxygen adsoprtion and desorption, thus enabling highly sensitive gas sensor. However, even in the junction-based gas sensing mechanism, the type of response will be determined by the majority charge carriers in the overall heterostructure or the MOx with higher doping.

Heterostructure based gas sensors, however, are known to be a little difficult and not so straightforward in some respects. For example, the formation of a heterostructure does not always guarantee lower operating temperature [59, 60]. Korotchenkov and Cho enlisted heterostructure disadvantages as follows: large number of factors affecting sensor response, issues with reproducibility of results, incomparable to binary MOx and one factor improves at the cost of others [61].

Both these models explain how a heterostructure can lead to more sensitivity towards changes in the oxygen adsorption, and in turn could make operation at low temperature feasible. There are plenty of mechanisms discussed in the literature depending on the materials and morphology used [7]. Some of them are discussed below.

1.2.2 State-of-the-art on heterostructure based gas sensors

Mashock *et al.* developed a p-type CuO NW sensor that is functionalised with n-type SnO_2 nanocrystals and is thus able to operate at room temperature. The authors explained the conduction channel phenomenon that occurs in such kind of a sensor. They studied the effectiveness of the conduction channel model and commented that SnO_2 coverage affects the sensing performance [52]. Another example of the classic conduction channel model with n-type MOx decorated with p-type MOx is work done by Woo *et al.* They developed a highly sensitive and selective trimethylamine sensor using n-type ZnO NW network decorated with p-type Cr_2O_3 nanoparticles hetero-nanostructures [53].

CuO has a natural affinity for reacting with H_2S. CuO, a MOx, reacts with H_2S to from CuS which is metallic in nature. This forms an interesting case study in heterostructure gas sensors. Wang *et al.* synthesised CuO nanoparticle decorated ZnO nanorod sensor for low temperature H_2S detection. CuO -ZnO form p-n junctions at the interface of contact. It is known that conduction band edge of CuO is higher than that of ZnO. This leads to transfer of electrons from the conduction band of CuO to that of ZnO and the transfer of holes from the valence band of ZnO to that of CuO. At the equilibrium state, an electron depletion region is formed and the resistance of ZnO is increased compared to pure ZnO. When this nanostructure is exposed to H_2S gas, it reacts with CuO to form CuS destroying the heterojunctions and the depletion layer. This results in the remarkable decrease in resistance of ZnO and easy detection of H_2S [34].

The easiest way to achieve a heterostructure based on the potential energy barrier model is to have a core-shell nanoparticle morphology. Kim *et al.* designed a CuO - ZnO composite sensors using hollow spheres morphology. This sensor was found to be selective towards H_2S at 336 °C while selective towards ethanol at 475 °C [60]. Wang *et al.* also worked with p-n-type materials Co_3O_4 - SnO_2 to make core-shell nanospheres. These nanosphere gas sensors were used for ammonia sensing at 200 °C for concentrations as low as 10 ppm [59]. Both of these articles described the mechanism based on the potential energy barrier model of conduction where electrons are forced to cross the potential energy barrier formed in each grain to have any conduction through the device at all. It is important to note that use of heterostructure did not lower the operating temperature of these sensors noted here.

1.3 Light activation

Parts of the following section are taken from a co-authored article [7] and are differentiated from the rest of the text by use of computer modern font.

In literature, light activation is also a very popular sought-after solution for overcoming the

disadvantages posed by high temperature operation of most MOx gas sensors. Researchers have worked with various wavelengths of light, IR, UV or visible, based on the band gap of the material used in the sensors [10, 62, 63, 51]. In the following subsection, we try to understand the basic role of light activation.

1.3.1 Role of light activation in gas sensing

The generally accepted principle of light activation, also known as photo adsorption-desorption model, as represented in Figure 1.5, is described in literature as below. Photons with energy equal to or greater than the band gap of the MOx semiconductor excite an electron from the valence band to the conduction band, leaving a hole in the valence band. The photogenerated electron-hole pair has a natural tendency to recombine, releasing the excess energy thermally. The lifetime of photogenerated electron-hole pairs is typically in the order of picoseconds. However, if recombination time is sufficiently longer, the photogenerated electron and hole can participate in redox reactions with the compounds adsorbed on the surface of the MOx or in the surrounding atmosphere [64, 65, 12, 5, 21].

The photogenerated holes (h_h^+) react with adsorbed oxygen and release it into the atmosphere, while the photogenerated electrons (e_h^-) react with atmospheric oxygen helping it adsorb on the surface, as shown in the respective following equations:

$$h_h^+ + O_{2(ad)}^- \longrightarrow O_{2(g)} \tag{1.7}$$

$$O_{2(g)} + e_h^- \longrightarrow O_{2(ad)(h)}^- \tag{1.8}$$

The reactions in equations 1.7 and 1.8 are believed to occur simultaneously and attain an equilibrium state, where most of the oxygen adsorbed on the surface is due to photogenerated electrons ($O_{2(ad)(h)}^-$) . $O_{2(ad)(h)}^-$ is believed to be loosely bound to the semiconductor surface and thus more reactive than $O_{2(ad)}^-$ [12, 64]. Therefore, light irradiation is believed to increase adsorption and desorption rates, reducing response and recovery times of MOx gas sensors and, in turn, leading to higher sensitivity [65].

Following this, the operation of gas sensor remains same as mentioned before. The role of illumination is the same as heat, to create extra charge carriers in the MOx to enhance oxygen adsorption. More details about light activation can be found in a recent review [7].

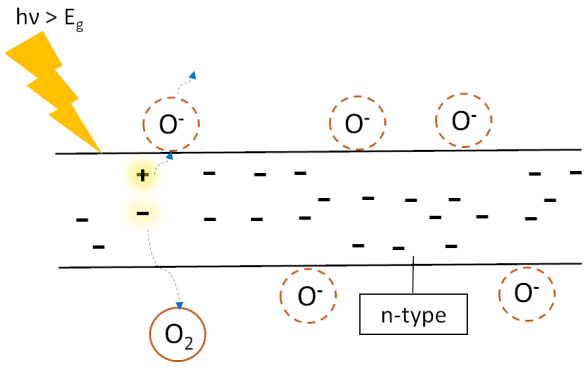

Figure 1.5: Schematic representing effect of light activation on MOx in presence of air

1.3.2 State-of-the-art on light activated gas sensors

Ultra-violet (UV) light is used to activate large band gap materials like ZnO. Fan *et al.* reported on effects of UV illumination on electronic and gas sensing properties of polycrystalline ZnO. They found that UV light helped photoinduced adsorption of oxygen ions which were responsible for room temperature gas sensing of ppm level H_2 by ZnO. They also concluded experimentally, smaller the grain size, larger number of photoinduced oxygen ions will be generated [12]. Many similar works have been done in the past enhancing sensing performance of different large band gap MOx with UV light [62, 66, 67]. However, this does not really overcome the disadvantage of high power requirement as UV light generation requires power.

Not much work is done on testing the gas sensing properties of CuO nanostructures in light. Hansen *et al.* probed opto-electronic properties of single CuO NWs in white light. They also tested it's gas sensing properties towards oxygen and NO_2 and found that photoinduced adsorption leads to enhanced device response [68].

Heterostructures are proved to improve the utilisation of photogenerated electrons and holes by suppressing their recombination. Take the example of work done by Wu *et al.* and Geng *et al.* [51, 63]. Wu *et al.* fabricated a three dimensional ZnO-CdSe heterostructure which displayed 20 fold higher sensitivity in dark and three fold higher sensitivity in visible light towards ethanol. The operating temperature of this sensor was lowered to 160 °C which is 100 °C lower than general MOx. The authors indicated that this visible light operation and improvement in sensitivity was due to two reasons; light activation of CdSe and effective charge carrier separation due to heterostructure band alignment [51]. Geng *et al.* worked with CdS-ZnO coatings and presented room temperature NO_2 sensor working with visible light [63]. Similar work was done by Park et al. with ethanol sensing of UV irradiated ZnO/Cr2O3 sensor, where they emphasised how the heterostructure can prevent recombination of

photogenerated electron-hole pairs and increase their lifetime [69]. In the past decade, researchers have also worked on integrating ZnO and CuO/Cu2O in various kinds of heterostructures to detect hazardous and organic gases at low temperatures [70, 54, 71, 72, 73, 74].

It is important to remind here that ZnO does not absorb in the visible spectrum. We take inspiration from the work mentioned above and attempt to integrate CuO, which shows absorption in the visible range, with ZnO, which is a known good sensor material. Thus, in this work, we concentrate on use of the visible light (from 400 nm to 700 nm wavelength) to activate MOx sensor in order to achieve low power sensing. We also want to benefit from heterostructure at nanoscale to lower the eventual operating temperature of the MOx sensor.

1.4 Conclusion

Based on the information provided above, we understand that oxygen adsorption and desorption control the kinetics of a chemiresistive MOx sensor. We also understand that high temperature operating MOx sensors pose limitations in terms of energy efficiency and applications.

The concept of heterostructures and light activation can overcome the disadvantages of high temperature operating MOx to enable low power gas sensors. Heterostructures combine individual properties of two different materials along with some synergistic effects due to heterojunction, which allows low temperature operation, better selectivity and many more benefits in terms of gas sensing applications. Light irradiation generates excess charge carriers that can participate in redox reactions in turn improving the sensitivity of gas sensing materials. Light can also help dissociate complex organic compounds into simpler gasses that can then be detected by gas sensing materials.

Keeping the above mentioned advantages in mind, we choose ZnO, an efficient transducer material and CuO, a visible light absorbing material, to fabricate a heterostructure, which can absorb visible light to be used for gas sensing application. This chapter provides a brief overview of work done with ZnO and CuO nanomaterials in gas sensing applications. This literature forms a foundation for the work done in this thesis.

As mentioned at the start of the chapter, the aim here was to provide a brief overview of the basics of gas sensing principles and the work done in this field. This chapter provides a concise background along with references for more details, in case the reader wishes to dive into it. Armed with this background knowledge, the reader will now be able to deeply understand the challenges of this work and how they were overcome.

Chapter 2

Methods

This chapter will introduce the reader to various equipment used during the course of this thesis. Basic settings and configurations used for the equipment are mentioned here. Since manuals and brochures of the equipment can be referred to for specifications and detailed working, unless relevant to the experiments performed, such technicalities are not mentioned in the sections below. However, the settings used for such tools are mentioned.

The tools used are broadly divided into three categories; tools used for synthesis and post processing of nanostructures, tools used for characterisation of these nanostructures, and finally the developed gas sensor test bench. The synthesis and post processing tools section describes the the basic glassware and chemicals used for experimentation along with equipment like the carousel used to obtain the end product of nanostructures. Post processing tools include description of settings used for centrifuge, furnace, etc. The end product of post processing is nanostructures dissolved in ethanol ready for deposition on a substrate or a device. This section also elaborates on device fabrication techniques, equipment used to develop electrodes, etc. leading to a fully functional device ready for electrical and gas sense testing.

Characterisation tools used are categorised based on the information they provide; morphological characterisation tools like SEM, AFM, TEM; structural characterisation tool - XRD, optical characterisation tool - spectrophotometer, elemental characterisation tools like EDX and XPS; and electrical characterisation tools like probe stations and multimeters. With an exception of XPS and TEM, all the characterisations and subsequent interpretations were executed by the author after required training and with the help of the supervisor.

A gas sensor test bench was designed, developed and assembled at LIST as a part of this thesis, and can be considered as one of the major accomplishments. A description of the components of this gas

sensor test bench is provided in this section. The gas sensor test bench is now a versatile and efficient system allowing functional characterisation of materials and is used in multiple projects at LIST.

2.1 Synthesis and post processing tools

2.1.1 Synthesis tools

Chemicals zinc chloride ($ZnCl_2$), hexamethylenetetramine (HMTA), copper chloride ($CuCl_2$), sodium dodecyl sulfate (SDS), and hydroxylamine hydrochloride ($NH_2OH \cdot HCl$) are sourced from Sigma Aldrich in powder form. Sodium hydroxide is sourced from Sigma Aldrich in form of pellets while 25% ammonia solution (NH_4OH) was sourced from Carl ROTH. All the above chemicals were sealed with parafilm and stored at room temperature inside appropriate chemical cabinets. They were used in the as received form without any further purification or processing. 2 M hydrochloric acid (HCl) stock solution was prepared and used as and when required. 18.2 MQ de-ionised water was used for all purposes.

Standard glassware like beakers, conical flasks, pipettes, measuring cylinders, etc were used wherever necessary. The glassware used for all experimentation was standard laboratory glassware from Duran, Blau Brand, or VWR. The glassware was cleaned and dried thoroughly before each use and washed with tap water and technical grade ethanol immediately after use.

All of the nanostructure synthesis procedures require stirring, while some also require heating and pH monitoring. There are three ways to achieve this, with the use of (i) a magnetic stirrer with a hot plate, (ii) Radley's Carousel 6 plus reaction station or (iii) Radley's MYA4 reaction station. The choice of equipment was largely depended on the number of batches of synthesis, availability of the equipment and the equipment specific glassware. All three equipment are quite capable of successfully delivering the required stirring speeds and temperatures of the synthesis procedures performed in this thesis. It is thus important to note that the use of different equipment did not affect the final product of the reaction as long as the procedure was correctly followed.

All the synthesis procedures having reaction temperature other than room temperature (RT), mention the reaction temperature as the temperature of the solution and not the temperature of the heating plate. All the heating equipment mentioned above have a default display of heating plate temperature unless an external temperature probe, dipped in the solution, is connected. Thus, an external temperature probe to monitor the solution temperature in real time was used with all of the equipment. The above mentioned equipment have integrated software to display the temperature of the external temperature probe, which makes this easier.

Whenever pH monitoring of the solution was required, pH monitor Portamess from Knick was used. It is an external pH monitor whose probe needs to be inserted into the solution. A separate device with a digital pH read out is used to get the pH of the solution in real time. The pH probe has an integrated temperature probe too. However, in all of the experimentation, it was observed that the temperature reading on the pH meter was lower than that of the individual temperature probe used. For temperature, the reading of the individual temperature probe was always trusted.

2.1.2 Post processing tools

The nanostructures are synthesised in solution. However, they cannot be stored in their mother solution for the fear of structural and elemental modifications. The mother solutions are usually not of neutral pH, and may cause changes in the nanostructures. Also, water is not a neutral solvent for long term storage. All the nanostructures are centrifuged to remove them from mother solutions. They are then washed with DI water and laboratory grade ethanol using centrifuge again. Finally, all the nanostructures are stored in absolute ethanol.

In some steps, there was need to dry the nanostructures and prepare them in powder form. For this purpose, Alpha 3-4 LSC basic freeze dryer from Christ and a universal mechanical oven from Memmert was used. This test was primarily done on Cu_2O truncated cubes. It was found that there was no difference in the end result of freeze drying or oven drying the cubes. Hence, freeze drying and oven drying was interchangeably used in this work. For calcination of Cu_2O truncated cubes and for annealing of devices, Nabertherm series 400-1 M03.0012 furnace was used at various temperatures as required by the procedure and in air atmosphere. Annealing was always done in air atmosphere.

2.1.3 Device fabrication

The electrodes were designed in KLayout software under the guidance of Stéphanie Girod, LIST. The electrodes are fabricated on SiO2-coated Si substrate by optical lithography using Mask Less Aligner (MLA-150) from Heidelberg Instruments. This is followed by e-beam evaporation of 5 nm Ti and 100 nm Au, and lift-off. The device fabrication, MLA and e-beam evaporation was performed by Stéphanie Girod, LIST. An example of interdigitated electrodes and single electrodes is shown in figure 2.1 a) and b), respectively. The single electrodes had a spacing of 2 μm, 5 μm, 10 μm and 20 μm with electrodes lengths 10 μm, 50 μm, 100 μm, 200 μm and 300 μm each. For the interdigitated electrodes designed, the different configurations used are mentioned in table 2.1.

The nanostructure network devices are fabricated by dispersing droplets of the solution containing the

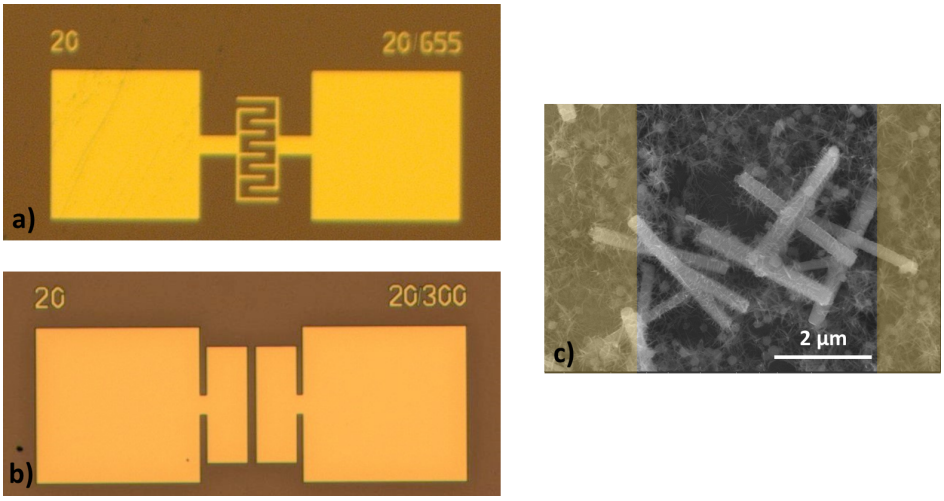

Figure 2.1: Light microscope images of electrodes used in devices in this work a) example of interdigitated electrodes, b) example of single electrodes, c) SEM image of network of nanostructures between two gold electrodes formed by drop casting nanostructure solution on the device. The gold electrodes in c) are light yellow in colour to enable identification.

nanostructures on predefined electrodes and letting the solution dry in air and at room temperature for approximately 5 minutes. This is also known as drop casting. The nanostructures, thus form a network between the electrodes as shown in Figure 2.1 c), enabling pathways for current transport from one electrode to another.

2.2 Characterisation tools

2.2.1 Morphological characterisation tools

The basic morphological characterisation tool used is the scanning electron microscope (SEM) from Helios Nanolab 650 from FEI. The preferred mode of scanning was immersion mode with through-the-lens (TLD) detector. Top view images were obtained at various acceleration voltage and current combinations ranging from 2.5 kV, 25 nA to 10 kV, 100 nA and a working distance of 4 mm. For colouring the SEM images to highlight certain nanostructures, a free version of MountainsLab software was used.

Some Cu based nanostructures were also analysed under the atomic force microscope (AFM) model INNOVA from Bruker. AFM was primarily used to determine the thickness of the individual nanostructures. AFM measurements and analysis presented through the thesis is done by Patrick Grysan, LIST

Transmission electron microscopy (TEM) investigations were carried out using a JEM - ARM 200F

number of electrodes	electrode spacing (μm)	length of electrodes (μm)
3 electrodes	2	240
	5	265
	10	280
	20	330
5 electrodes	2	488
	5	515
	10	560
	20	655
7 electrodes	2	816
	5	855
	10	920
	20	1050

Table 2.1: Details of electrode spacing and total electrode length designed for interdigitated electrodes

Cold FEG TEM/STEM operating at 200 kV and equipped with a spherical aberration (Cs) probe and image correctors (point resolution 0.12 nm in TEM mode and 0.078 nm in STEM mode) at Institut Jean Lamour, Université de Lorraine. This collaboration was through Natallie Valle, LIST. Samples for TEM analysis were prepared by Asmaa El Moul, LIST.

2.2.2 Structural characterisation tool - *XRD*

For determination of the crystal structure of formed products, X-ray diffraction (XRD) was performed with a X-Ray diffractometer from Bruker equipped with a copper x-ray source with an emission wavelength of 0.1542 nm. The diffractograms are recorded in θ -2θ mode, analysing from 10° to 60°. For the samples where information was not obtained in θ -2θ, also known as locked couple mode, diffractograms were recorded in grazing incidence mode. Grazing incidence mode allows probing the surface without going deep within the sample. For the all the scans, the step size was set to 1 while time per step was set to 2 s. The diffractograms were analysed using software Diffrac Suite EVA from Bruker and compared to the database of PDFs for confirmation of crystal structure.

2.2.3 Optical characterisation tool - *Spectrophotometer*

The absorption spectra of the nanostructures deposited on glass were measured with a Perkin-Elmer Spectrophotometer Lambda 1050 equipped with a 150 mm integrating sphere. The absorbance (A) spectra have been obtained from the transmittance (T) and reflectance (R) measurement using A = 1 - R - T. The

range for measurements was 250 nm to 1500 nm, as below 250 nm, the glass substrate will not transmit.

2.2.4 Elemental characterisation tools

Primary elemental characterisation was carried out with energy dispersive X-ray spectroscopy (EDX) integrated with SEM at LIST. The software INCA was used to control the movement of the detector and record the EDX spectra. A voltage of 10 kV or 20 kV with high current of 50 - 100 nA suited EDX measurements. Area scan was done on selected area with a scan time of roughly 100 s. EDX allowed identifying elements present in the nanostructure on a primary basis. The quantitative measurements presented by EDX were not trusted very much due to the lack of resolution and calibration of the instrument. Nevertheless, it gave an idea of what to expect in detailed elemental characterisation.

Elemental characterisation and chemical state identification were carried out by X-ray photoelectron spectroscopy (XPS) (Axis Ultra DLD, Kratos Analytical Ltd.) using a monochromated X-ray source (Al Ka , E=1486.6 eV) working at 150 W. Narrow spectra were acquired on a 700 x 300 μm^2 area and with a 20 eV pass energy (corresponding to a full width half maximum of 0.6 eV for the Ag $3d_{\frac{5}{2}}$ peak on a sputter cleaned silver sample). A charge neutralizer system was used for all samples as needed. All the XPS spectra were calibrated on the adventitious carbon C 1s peak at 284.6 eV. Quantification and peak fit procedures were carried out with the software CasaXPS (version 2.3.22). The XPS characterisation and analysis was done by Jérôme Guillot, LIST.

2.2.5 Electrical characterisation tools

For electrical characterisations, two tools are used interchangeably, PM8 probe station from Cascade Microtech and THMS600 / HFS600 temperature control stage probe station from LINKAM. Both probe stations work along with Keithley multimeter (SMU 2614B or 2634B) and Labber software from Keysight to record current voltage (IV) characteristics of a device. PM8 has an open stage with micromanipulators and a light microscope to control the placement of the probes. Linkam probe station has an enclosed chamber of 50 cc and thus a possibility to record IV characteristics in controlled environment. More about the Linkam probe station is mentioned in the next sub section related to the gas sensor test bench. In all the IV characteristics measured, two probe measurements were performed. Whenever electrical measurements at higher temperatures or in presence of particular gasses are mentioned, they are measured with the Linkam probe station.

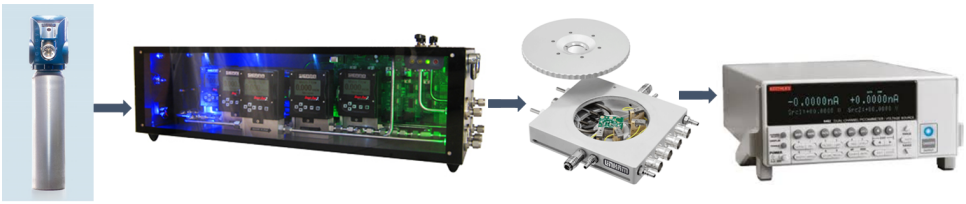

Figure 2.2: Schematic representing set up components and flow of gas through the gas sensor test bench

2.3 Gas sensor test bench

Gas sensing measurements are one of the most important characterisations that the nanostructures have to go through for the purpose of this thesis. A gas sensor test bench was assembled and set up at LIST during the course of this work, as mentioned before. A schematic representing the components of the gas sensor test bench are shown in Figure 2.2.

2.3.1 BIOAGE gas mixing system

The Bioage gas mixing system, GMIX-5CH, consists of 5 mass flow controllers (MFCs). It has inlet for one carrier gas that can flow through 3 MFCs and two target gasses inlets that are controlled by the remaining two MFCs. The mixing system is controlled through a programmable software, which was incorporated into Labber for ease of use. The MFCs can be thus switched on, switched off and set to a particular flow with the help of this software.

We use ECOCYL gas bottles mixtures from LINDE for synthetic gasses like 1000 ppm NO_2 in air, 2% H_2 in N_2 and 100 ppm CO in air. For synthetic air and N_2 large bottles from AirLiquide are used.

The gasses are mixed in required quantities in the pipeline of the Bioage gas mixing system after which the gas mixture flows through the outlet of the machine to the inlet of the LINKAM probe station as shown in Figure 2.3

2.3.2 LINKAM probe station

The Linkam THMS600 / HFS600 is an enclosed probe station with a volume of 50 cc, a temperature controlled stage with the possibility for attaching four probes. The probes need to be manually placed on the contacts of the device. The enclosure ensures that the atmosphere around the gas sensor device is controlled. The probe station thus has an arrangement for gas inlet and outlet. From the outlet of the

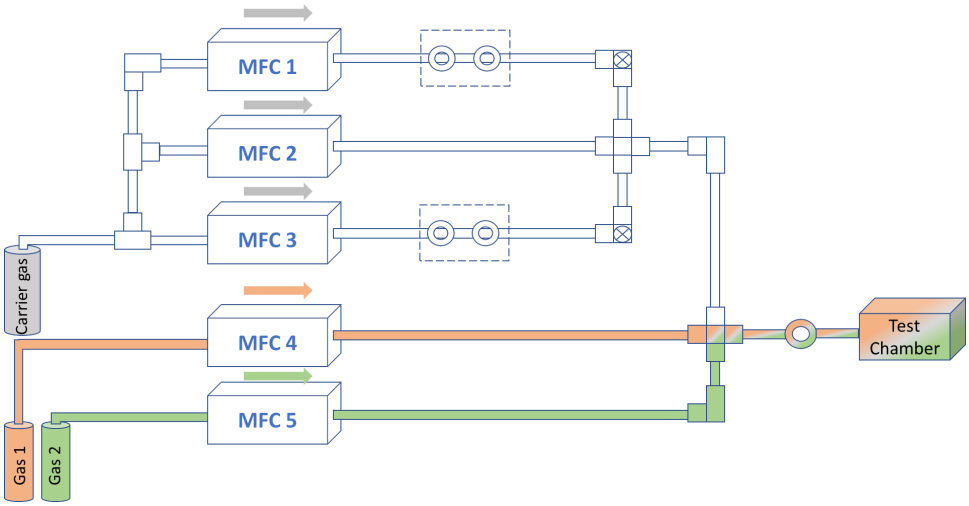

Figure 2.3: Schematic representing the internal and external connections of gas mixing system with flow of gas indicated through the gas sensor test bench. This schematic is adapted and modified based on the manual of GMIX-5CH provided by BIOAGE.

Linkam probe station, gasses are sent to exhaust. If flow rate of 100 sccm is used, the gasses in the test chamber will be renewed every 30 seconds.

The Linkam probe station along with Keithley multimeter and Labber software, record electrical response of sensor device to the gasses present inside the chamber of the probe station. The stage available in the Linkam probe station can be heated and cooled as needed. To do this another accessory, a temperature controller is required. Also with the help of a dedicated software, LINK, the temperature of the stage is maintained. Thus gas sensing measurements at high temperatures are easy to follow through.

Chapter 3

Synthesis and Characterisation of nanostructures

This chapter will describe the synthesis procedures used for fabrication of various nanostructures. The synthesis of each nanostructure will be followed by the morphological, structural, optical and elemental characterisation. These characterisations will allow us to know how the nanostructures are shaped, what are they made of, what wavelength of light do they absorb and what bonds constitute the surface of these nanostructures. Each of this information will act in support of the choices we make for the applications of these nanostructures and will help us justify observations we have in process of application.

The chapter is largely divided in two subsections, single nanostructures, representing single MOx nanostructures and heterostructure, representing nanostructure made of more than one MOx. We discuss seven single MOx in the first section, namely, ZnO nanorods, ZnO nanoflowers, $Cu(OH)_2$ nanowires, $Cu_2(OH)_3Cl$ nanoplatelets, $Cu_2(OH)_3Cl$ crystals, CuO bundles and Cu_2O truncated cubes. In heterostructures, we discuss only two, ZnO NRs + $Cu_2(OH)_3Cl$ nanoplatelets and ZnO Nanoflowers + CuO truncated cubes. The nanostructures are schematically represented in Figure 3.1 with its intended purpose, as an intermediate step for another nanostructure and / or as an individual sensing material.

ZnO NRs and ZnO NFs are synthesised as precursors and comparison nanostructures for heterostructures. They are characterised in detail as the synthesis procedure is unique. Functional properties of ZnO NRs will be studied in comparison with the ZnO NRs + $Cu_2(OH)_3Cl$ nanoplatelets heterostructure in chapter 5 of this thesis.

In the next subsection, we show the template-free bottom-up synthesis and shape control of copper hydroxide based nanostructures grown in liquid phase, from 1D nanowires to 2D layered nanoplatelets

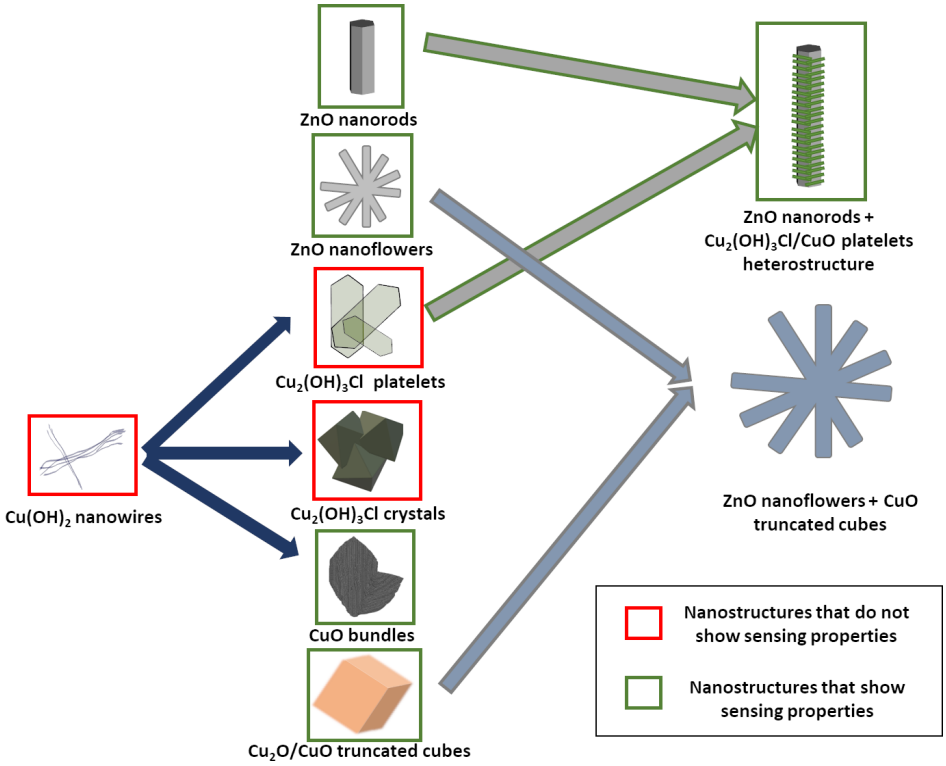

Figure 3.1: A scheme depicting all the nanostructures discussed in this chapter along with their co-relations and whether or not they were used in this thesis as sensing materials.

and 3D crystals. Precise control over the pH of the solution and the reaction temperature lead to intended tuning of the morphology and chemical composition of the nanostructures. Among the copper hydroxy salts, the botallackite polymorph is known as an intermediate compound which is difficult to stabilise in mother solution. We show here a way to achieve the stable botallackite in form of nanoplatelets. Characterisation of the obtained copper hydroxide based nanostructures is also provided. We contemplate upon the rationale behind this change in shape and material.

In addition to the copper hydroxide based nanostructures, we also discuss the synthesis and characterisation of CuO bundles and Cu_2O truncated cubes. CuO bundles are individually interesting gas sensing material and its functional characterisation is discussed in detail in chapter 4 of the thesis. On the other hand, Cu_2O truncated cubes, are intermediate structures and analysed to eventually achieve CuO truncated cubes. CuO truncated cubes are of interest for incorporation in the ZnO Nanoflowers + CuO truncated cubes heterostructure.

Finally, the novel multistep synthesis approach for two possible heterostructures, ZnO NRs + $Cu_2(OH)_3Cl$ nanoplatelets and ZnO Nanoflowers + CuO truncated cubes is presented. In characterising

these new structures, we attempt to determine if they really are heterostructures or not.

3.1 Single nanostructures

3.1.1 ZnO nanorods (NRs) and ZnO nanoflowers (NFs)

ZnO nanorods (NRs) and ZnO nanoflowers (NFs) are synthesised and studied with the primary aim to incorporate them in heterostructures. We approach the synthesis of ZnO-CuO heterostructure in two ways: ZnO nanostructure, like NRs, decorated with CuO nanostructure or CuO nanostructure at the core with ZnO NRs grown on it. Thus we study synthesis of two kinds of ZnO nanostructures, one NRs which can be easily decorated with CuO nanostructures and second a ZnO NFs which is ZnO NRs grown on a seed, as will be explained more in detail in this section.

ZnO NRs were synthesized based on the work done by Caicedo *et al.* [75]. 100 mL DI water was heated to 70 °C. 1 mL 1 M $ZnCl_2$ and 1 mL 1 M HMTA was added under 500 rpm stirring. After this addition, the temperature of the solution was increased to 85 °C and maintained so for 100 minutes. After 100 minutes the stirring and heating were stopped and the solution was brought down to room temperature. The precipitated nanostructures were centrifuged, washed and stored in absolute ethanol. The synthesis procedure is described in Figure 3.2 a).

ZnO NFs are synthesised by modifying the above procedure. There is an additional step where ZnO nanoparticles were introduced before addition of $ZnCl_2$ and HMTA. The synthesis procedure is described in Figure 3.2 b). ZnO nanoparticles were also prepared in the laboratory using the following procedure from [76]. 50 mL, 30 mM NaOH solution (in methanol) is added drop wise to 25 mL, 10 mM solution of zinc acetate dihydrate (in methanol) under continuous stirring at 60 °C for 2 h. The solution in methanol was stored as prepared, without any filtration or washing, and used as and when required.

Xu *et al.* have provided an extensive review on growth mechanisms of ZnO 1 dimensional nanostructures. They bellieve chemical reactions in aqueous systems to be in a reversible equilibrium, and that the minimization of the free energy is the driving force of growth. ZnO is a wurtzite structure that grows along the c axis as it has high energy polar surfaces $\pm$ (0001). These polar surfaces are either Zn^{2+} or O^2 terminated. When a ZnO nucleus is forming, the Zn^{2+} or O^2 precursor molecules in the aqueous solution tend to preferentially adsorb on the polar surfaces to minimize the surface energy. So a O^2-terminated surface changes into an Zn^{2+}-terminated surface, or vice versa. This is repeated over time, leading to growth along the $\pm$ [0001] directions [77].

This growth mechanism is applicable to both, ZnO NRs and ZnO NFs. But we still have two

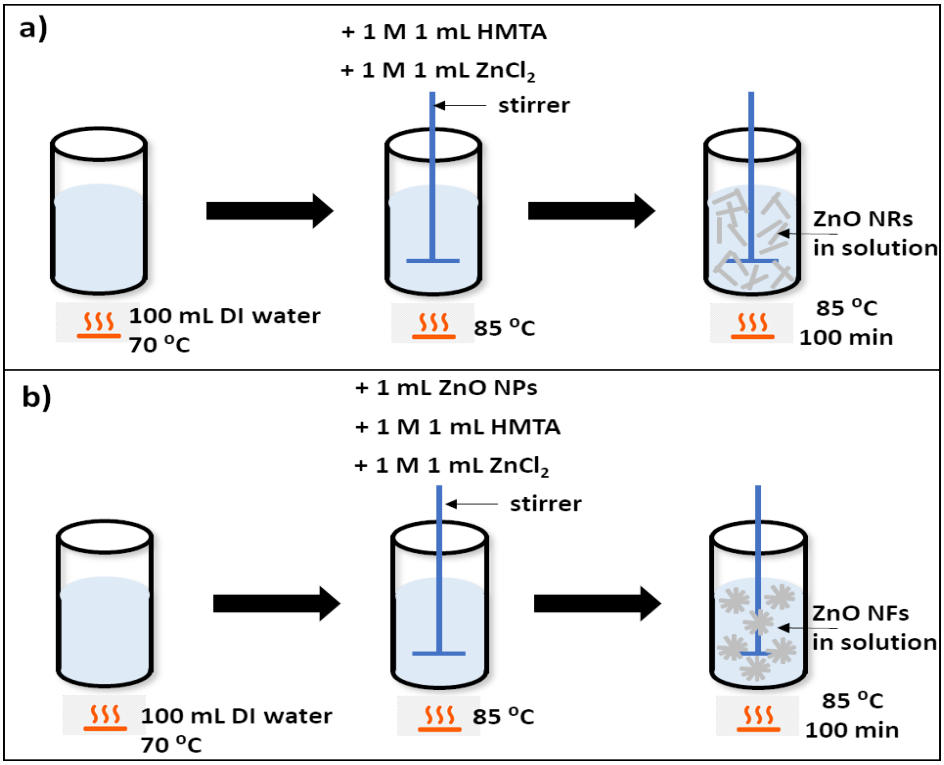

Figure 3.2: Schematic depicting synthesis procedure for a) ZnO NRs, b) ZnO NFs

morphologically different nanostructures. Here's why. In the synthesis procedure of ZnO NRs, nucleation took place spontaneously when the reaction precursors, $ZnCl_2$ and HMTA, were inserted in the heated water. Post the spontaneous nucleation, the growth continues in the fashion explained above, along the c axis only, and as a result we have NRs morphology. For ZnO NFs, ZnO nanoparticles were inserted in the heated water before adding the precursors and thus spontaneous nucleation did not occur. Instead, upon addition of the precursors, the growth started taking place on the nanoparticle in the water in all directions possible and continued so to form NFs. This growth phenomenon is also widely explored in the literature [77, 78]

ZnO NRs and ZnO NFs were primarily fabricated to be a comparison base line for heterostructures, later synthesised in this thesis. However, it is still important to characterise them well. Thus, SEM images of ZnO NRs and ZnO NFs are shown in Figure 3.3 a) and b), respectively. The ZnO NRs have an approximate length of 1 μm - 3 μm with the diameter of 100 nm - 500 nm. The ZnO NFs, on the other hand, have rods much smaller than ZnO NRs, with approximate length of 1 μm and diameter of 100 nm. In some cases, independent and larger ZnO NRs were also seen mixed with ZnO NFs, as shown in Figure 3.3 b).

Optical properties of ZnO NRs and ZnO NFs, in terms of their absorbance spectra, are shown in

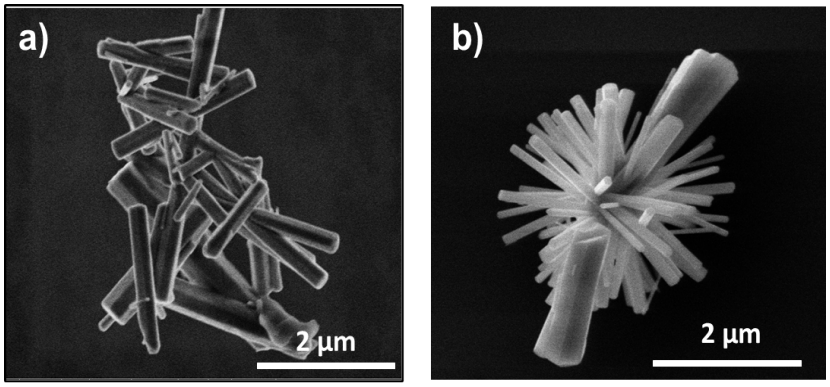

Figure 3.3: SEM images of as prepared a) ZnO NRs, b) ZnO NFs

Figure 3.4 a). We can observe that ZnO NRs and ZnO NFs do not absorb in the visible wavelength from 400 nm to 700 nm, similar to what is observed in bulk ZnO crystals in literature [79]. The high absorbance before 400 nm, roughly around 380 nm, can be attributed to band gap of ZnO while absorbance for wavelengths lower than 380 nm is attributed to the glass substrate used for these measurements. The Tauc plots corresponding to ZnO NRs and ZnO NFs are calculated and presented in Figure 3.4 b) and c), respectively, indicating the band gap of 3.1 eV for both.

XPS analysis were carried out on ZnO NRs and ZnO NFs for chemical identification. Figure 3.5 shows Zn 2p and O 1s spectra corresponding to as deposited ZnO NRs, as deposited and post 200 °C 2 h annealed ZnO NFs. No post deposition treatments were performed on the ZnO NRs. Zn 2p peaks observed at 1021.8 eV and 1044.9 eV for both ZnO NRs as well as ZnO NFs in Figure 3.5 a), correspond to zinc oxide as observed in literature [80, 81, 82]. The O 1 s peak in Figure 3.5 b) was de-convoluted into O-Zn at 530.55 eV and OH at 531.65 eV, showing that hydroxide groups are present in or at the surface of as deposited ZnO NRs. Figure 3.5 b) also shows the O 1s peaks of as deposited and post 200 °C, 2 h annealed ZnO NFs. It is noticeable that no major change occurs in oxidation state of Zn and bonding of oxygen in ZnO NFs on annealing.

3.1.2 $Cu(OH)_2$ NWs, Botallackite $Cu_2(OH)_3Cl$ nanoplatelets, $Cu_2(OH)_3Cl$ nanocrystals, CuO bundles

Most of the text in this subsection is adapted, either directly or with slight modification, from two articles [83] and [84] from Bhusari *et al.* also obtained as a result of work done under the framework of this thesis. Figures in the subsection are similar to the publications, but modified to be relevant in the context of the thesis.

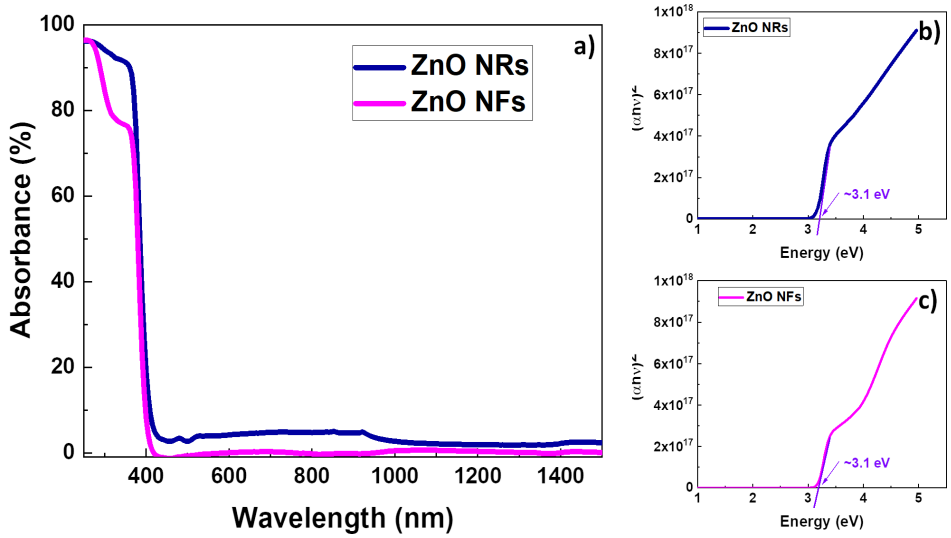

Figure 3.4: a) Absorbance spectra of ZnO NRs in royal blue and ZnO NFs in magenta indicating that ZnO nanostructures do not absorb light in visible wavelength range. Tauc plot of b) ZnO NRs and c) ZnO NFs showing their respective calculated band gap.

The principle of the simple one-pot process for the synthesis of various Cu based nanostructures is described in Figure 3.6. Here, the main varying parameters are the temperature and the pH of the solution. The starting point for obtaining the nanostructures is $Cu(OH)_2$ NWs which is elaborated below.

The synthesis procedure followed for $Cu(OH)_2$ NWs is in line with the procedure described by Xu et. al. [85]. 85.2 mg of $CuCl_2$ was dissolved in 100 mL DI water at room temperature. 30 mL of 0.15 M NH_4OH solution was added to this under 500 rpm stirring. Next, 10 drops of 10 M NaOH solution was added to make the final pH of the solution equal to 12.5. Blue precipitate was immediately formed in the solution, following which stirring was stopped. The precipitate was centrifuged and washed with DI water and ethanol. It was stored in absolute ethanol for further characterisation.

To obtain botallackite ($Cu_2(OH)_3Cl$) nanoplatelets, the $Cu(OH)_2$ NWs are heated to 70 °C in their basic solution. The pH of this solution is reduced to 6 by adding around 2.5 mL of 2 M HCl. The precipitate changes its colour from blue to forest green. The solution is then cooled down to room temperature before washing and the product is stored in absolute ethanol. Clinoatacamite ($Cu_2(OH)_3Cl$) nanocrystals are obtained by heating as-formed $Cu(OH)_2$ NWs to 80 °C and reducing the pH of the solution to 5. The colour of the precipitate changes from blue to brown. The washing and storage procedure is similar to that of earlier products. For synthesis of CuO bundles $Cu(OH)_2$ NWs solution is heated at 85 °C for 5 hours to form CuO bundles without any additional pH modification

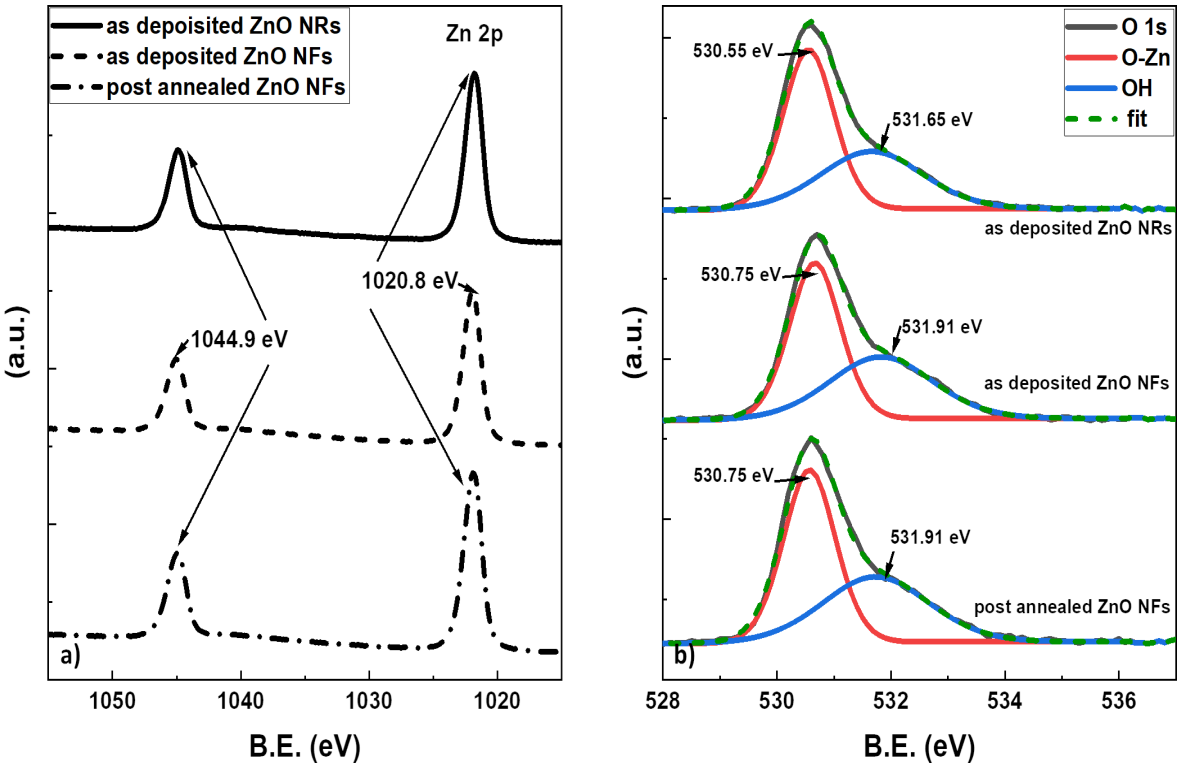

Figure 3.5: XPS spectra of a) Zn 2p, b) O 1s for as deposited ZnO NRs, as deposited and post 200 °C 2 h annealed ZnO NFs, respectively. The observed spectrum is in black while the fit, shown as dashed green line, is calculated based on combination of all the components mentioned in the legend.

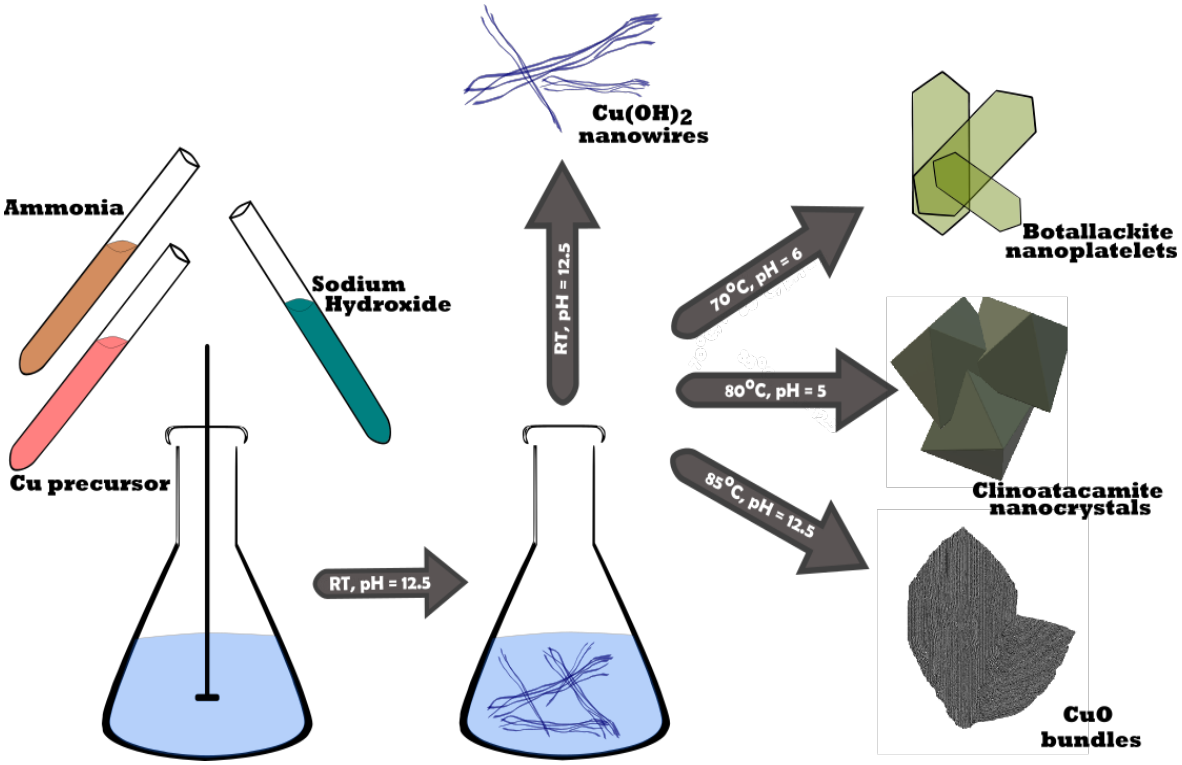

Figure 3.6: Schematic representing synthesis procedure for $Cu(OH)_2$ NWs, Bottalackite $Cu_2(OH)_3Cl$ nanoplatelets, Clinoatacamite $Cu_2(OH)_3Cl$ nanocrystals and CuO bundles

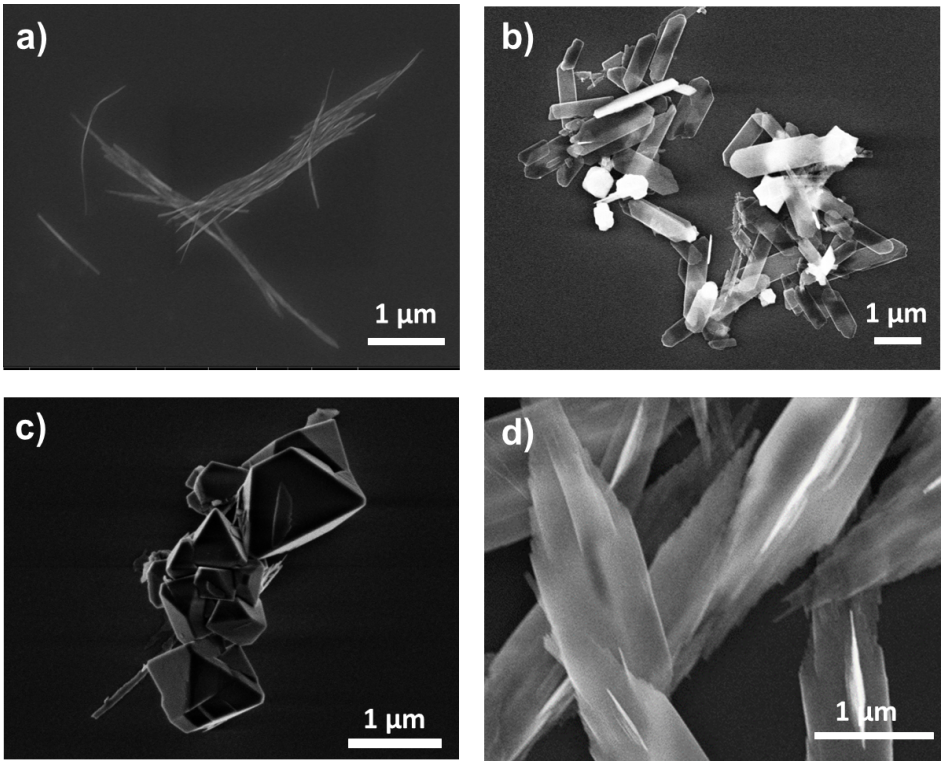

Figure 3.7: SEM images of a)$Cu(OH)_2$ NWs, b) Bottalackite $Cu_2(OH)_3Cl$ nanoplatelets c) Clinoatacamite $Cu_2(OH)_3Cl$ nanocrystals and d) CuO bundles

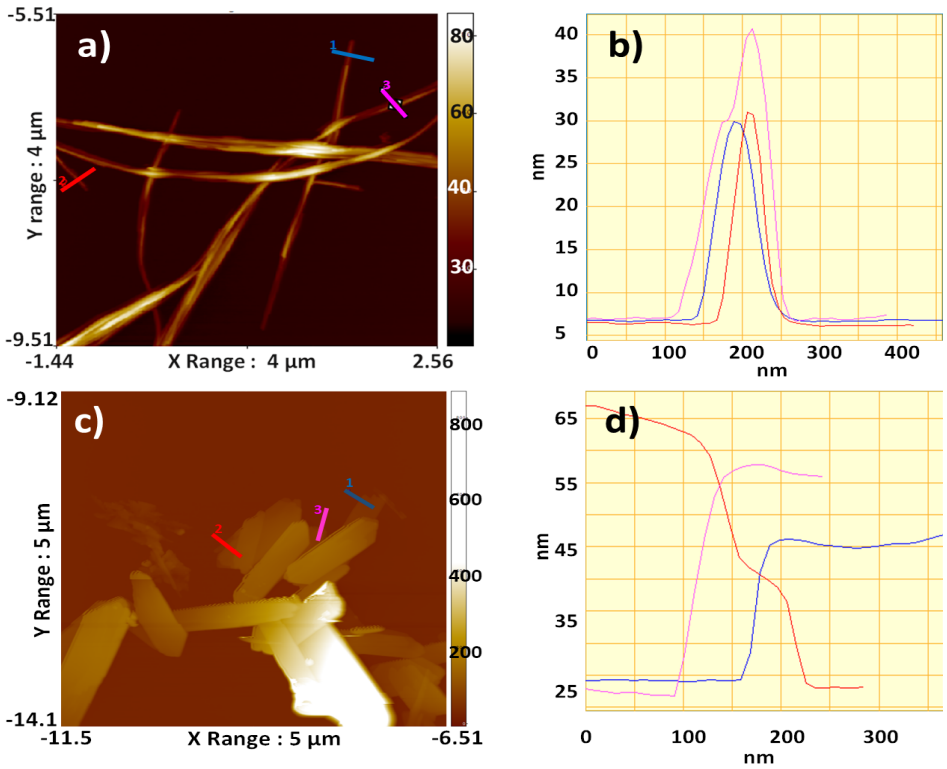

Figure 3.8: AFM images along with corresponding depth profiles of a) and b) $Cu(OH)_2$ NWs, c) and d) Bottalackite $Cu_2(OH)_3Cl$ nanoplatelets

step. However, the pH of the solution is observed to lower from 12.5 to 11 at the end of the 5 hours. The CuO bundles precipitate, black in colour, was washed with water and stored in absolute ethanol.

The nanostructures obtained using this process are presented in Figure 3.7, showing SEM of various kind of Cu based nanostructure morphologies. $Cu(OH)_2$ NWs (Figure 3.7 a) are found to have an approximate length of 3 - 6 μm and maximum diameter of 30 nm, as measured by atomic force microscope (AFM) (see Figure 3.8 a) and b)). Botallackite $Cu_2(OH)_3Cl$ nanoplatelets have width between 400 - 700 nm while the length is between 1 - 3 μm as shown in Figure 3.7 b). The thickness of the nanoplatelets is merely 15 - 25 nm, as determined by AFM (see Figure 3.8 c) and d)). Botallackite nanoplatelets are known to be layered materials. The thickness of the nanoplatelets, thus, indicates that there are 25-40 layers of $Cu_2(OH)_3Cl$ in one nanoplatelet. Clinoatacamite $Cu_2(OH)_3Cl$ nanocrystals, with an approximate size of 700 nm, are shown in Figure 3.7 c). SEM image of CuO bundles is shown in Figure 3.7 d). CuO bundles are about 3 μ m in length and about 1 μ m in width.

The stability region of each type of nanostructure is well defined when varying the pH and the temperature, which allows us to draw a phase diagram depicting the transition from $Cu(OH)_2$ NWs

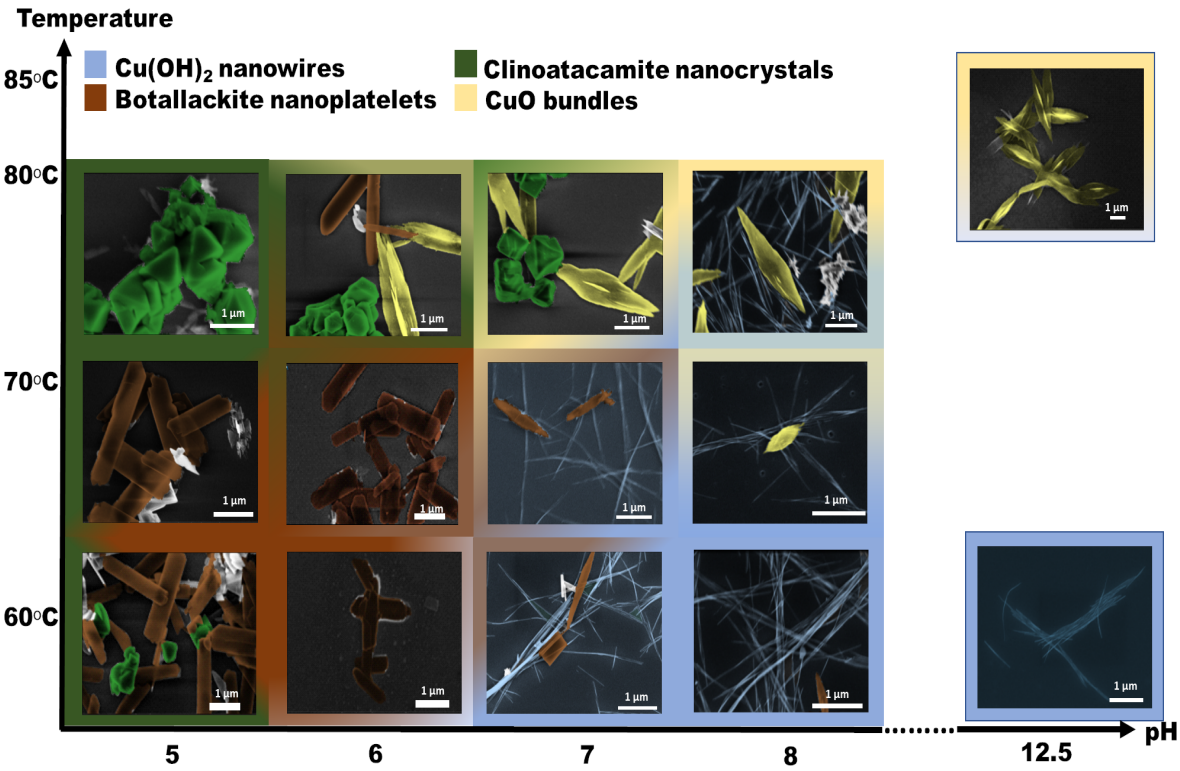

Figure 3.9: Phase diagram for the synthesis of Cu based nanostructures as a function of the solution pH, obtained by adding HCl to the original solution, and of the solution temperature. The SEM pictures of the obtained nanostructures are colorized with the following color code: blue for $Cu(OH)_2$ NWs, brown for $Cu_2(OH)_3Cl$ nanoplatelets, green for clinoatacamite crystals and yellow for CuO bundles.

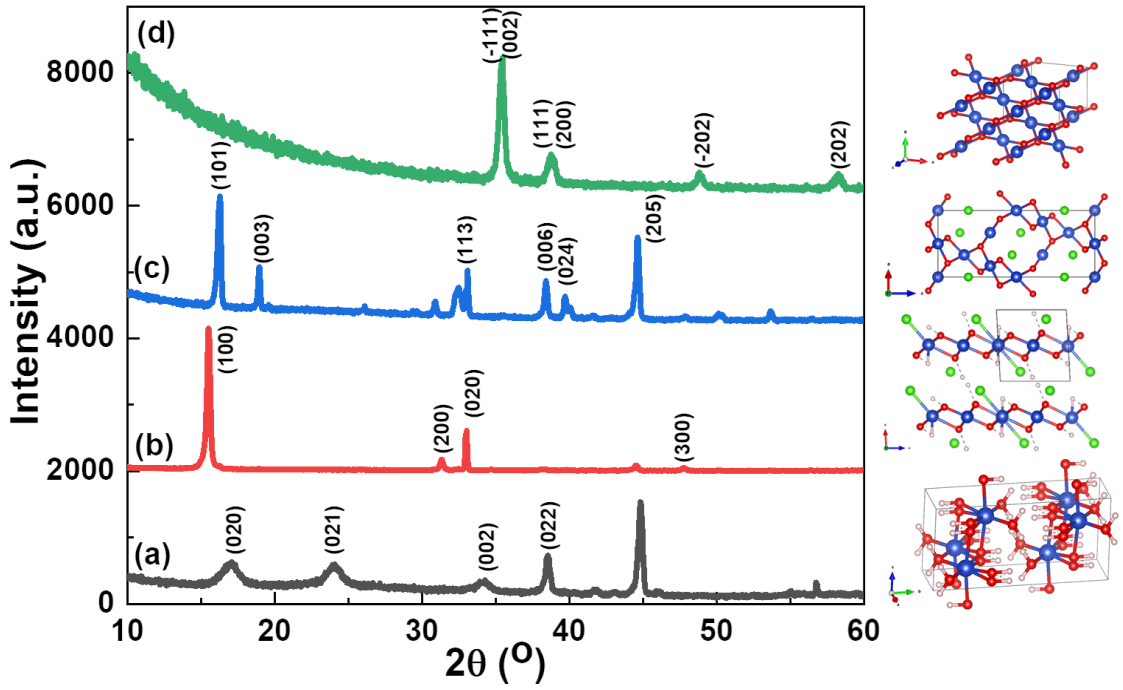

Figure 3.10: XRD spectra for (a) $Cu(OH)_2$ NWs, (b) Bottalackite $Cu_2(OH)_3Cl$ nanoplatelets (c) Clinoatacamite $Cu_2(OH)_3Cl$ nanocrystals and (d) CuO bundles along with their corresponding lattice structures on the right

to $Cu_2(OH)_3Cl$ nanoplatelets and nanocrystals. The phase diagram is shown in Figure 3.9. $Cu(OH)_2$ NWs are formed at room temperature and at a pH of 12.5. They are maintained when the temperature is increased to 60 °C. At 60 °C, as pH of the solution is decreased from 12.5 to 7 by adding HCl, the $Cu(OH)_2$ NWs start changing their shape. At 60 °C, with the pH reduced below 6, we observed formation of $Cu_2(OH)_3Cl$ nanoplatelets along with the presence of nanocrystals. On increasing the temperature of the solution to 70 °C, we observe a similar change from $Cu(OH)_2$ NWs to $Cu_2(OH)_3Cl$ nanocrystals and nanoplatelets on reducing the pH from 8 to 5. However, at 70 °C and pH of 6, pure phase of botallackite nanoplatelets is observed. $Cu(OH)_2$ NWs agglomerate to form CuO bundles at high temperature and high pH, as already demonstrated by Engelbrekt et al. [86]. While, when $Cu(OH)_2$ NWs are heated to 80 °C and the pH of the solution is reduced to 5, clinoatacamite nanocrystals are obtained.

Figure 3.10 shows the measured XRD patterns of the as prepared $Cu(OH)_2$ NWs, $Cu_2(OH)_3Cl$ nanoplatelets, $Cu_2(OH)_3Cl$ nanocrystals and CuO bundles. All the peaks in Figure 3.10 (a) can be

Table 3.1: Elemental composition of each Cu based nanostructure based on XPS analysis.

Nanostructure	C%	Cl%	Cu%	Na%	O%	Si%	Cu/O	Cu/Cl
$Cu(OH)_2$ NWs	20.0	1.9	29.6	0.0	48.5	0.0	0.61	14.16
$Cu_2(OH)_3Cl$ nanoplatelets	15.5	12.6	27.8	0.0	44.1	0.0	0.63	2.2
$Cu_2(OH)_3Cl$ nanocrystals	27.6	9.9	22.3	0.0	41.1	0.0	0.54	2.25
CuO bundles	2.0	0.0	34.1	2.6	46.5	2.0	0.73	-

indexed to orthorhombic phase of $Cu(OH)_2$ with the space group Cmcm with the calculated lattice parameters $b = 10.44$ Å and $c = 5.25$ Å, close to the expected values ($b = 10.59$ Å and $c = 5.256$ Å, PDF: 00-013-0420). Figure 3.10 (b) is found to be monoclinic phase botallackite of $Cu_2(OH)_3Cl$ with space group $P2_1/m$. The lattice parameters of unit cell for this phase of $Cu_2(OH)_3Cl$ is found to be $b = 5.42$ Å, slightly lower than the expected value ($b = 6.1255$ Å, PDF: 00-058-0520), which could be due the deficiency of Cu atoms (ratio Cu/O = $0.63 < 2/3$, see table 3.1). Other lattice parameters were not possible to calculate with the observed spectrum. Figure 3.10 (c) corresponds to the rhombohedral phase clinoatacamite of $Cu_2(OH)_3Cl$ with space group $R\bar{3}m$. The lattice parameters of this phase of $Cu_2(OH)_3Cl$ are calculated using formula for hexagonal crystal lattice system and are found to be $a = 6.69$ Å and $c = 16.25$ Å. These values are significantly different than the expected ones ($a = 6.827$ Å and $c = 14.041$ Å, PDF: 04-012-5828), probably related to the strong difference with expected stoichiometry (Cu/O = $0.54 < 2/3$, Cu/Cl = $2.25 > 2$, see table 3.1). For Figure 3.10 (d), the XRD peaks can be indexed to monoclinic phase of CuO with the space group C2/c with the calculated lattice parameters $a = 4.71$ Å, $b = 3.415$ Å, $c = 5.13$ Å and $\beta = 99.89°$, close the expected values ($a = 4.6883$ Å, $b = 3.4229$ Å and $c = 5.1319$ Å and $\beta = 99.506°$, PDF: 00-048-1548).

The elemental compositions determined by XPS are summarized in table 3.1. One can note that the amount of carbon is ranging from 12 at.% to 25 at.% in the different structures. This carbon may be due to surface contamination (the probing depth of XPS being less than 10 nm) or traces of organic solvent left on the substrate. Chlorine is observed in every sample but only in the range of 1 at.% for $Cu(OH)_2$ NWs whereas it is around 10 at.% and 12 at.% for both the $Cu_2(OH)_3Cl$ nanostructures. The Cu/O and Cu/Cl ratios help confirm the chemical composition of the material. The Cu/O ratio of $Cu(OH)_2$ NWs is expected to be around 0.5 and is found to be 0.63. The excess of copper can be associated with some of the copper bound to oxygen in the form of Cu_2O. For both $Cu_2(OH)_3Cl$ nanostructures, expected Cu/O ratio is 0.67 while calculated ratio is 0.63 and 0.54 for nanoplatelets and nanocrystals, respectively. On these two structures, the Cu/Cl ratio is slightly larger than 2,

Table 3.2: Positions of Cu 2p, Cu LMM and Auger parameter for Cu based nanostructures as observed in XPS spectra along with main copper states indicated in literature

Nanostructure/ Cu state	Cu 2p (eV)	Cu LMM (eV)	Auger Parameter (eV)
$Cu(OH)_2$ NWs	933.1	915.8	1848.9
$Cu_2(OH)_3Cl$ nanoplatelets	935.1	916.2	1851.3
$Cu_2(OH)_3Cl$ nanocrystals	935	916.7	1851.7
CuO bundles	933.9	917.3	1851.2
Cu_2O truncated cubes	934.6	916.3	1850.9
$Cu(OH)_2$ [82, 87]	934.5	916.3	1850.8
Cu_2O [82, 87]	932.6	916.3	1848.9
Cu^{2+} [82, 87]	934	917.3	1851.3

expected from the crystal stoichiometry. The Cu/O ratio being lesser than expected value (0.67) while the corresponding Cu/Cl ratio being larger than expected value (2) may be due to incomplete incorporation of Cl in the $Cu(OH)_2$ matrix to form $Cu_2(OH)_3Cl$. Cu/O ratio of CuO is expected to be 1 but is calculated to be 0.73. This is because CuO bundles contain both CuO and $Cu(OH)_2$, presumably due to a hydroxylated surface.

The nature of the Cu based nanostructures was identified by XPS by investigating not only the Cu 2p peak position but also the shape of the satellites characteristic of the copper chemical state as well as the Auger parameter value (Cu 2p – Cu $L_3M_{4,5}M_{4,5}$ peaks). The XPS spectra of Cu 2p peak and its satellites for copper hydroxide based nanostructures are shown in Figure 3.11 a). A clear evolution of the Cu 2p line and satellites shape is observed with the successive materials. Indeed, the spectrum for $Cu(OH)_2$ NWs presents a double peak maximum at 934.5 eV and 932.6 eV due to coexistence of two different phases. The Auger parameters associated to these two maxima are 1850.8 eV and 1848.9 eV corresponding to $Cu(OH)_2$ and Cu_2O phases, respectively [88, 89, 90]. The other samples exhibit a single peak (934.6 eV for the $Cu_2(OH)_3Cl$ nanoplatelets and nanocrystals). The Auger parameter of these other structures are ranging from 1851.2 eV to 1851.7 eV and correspond to Cu^{2+} atoms. Both, $Cu_2(OH)_3Cl$ nanoplatelets and nanocrystals, present the same Cu 2p spectra, similar to $Cu(OH)_2$ spectra found in literature [82, 87], especially when considering the shape of the satellites (940 – 945 eV) characteristic of the copper in a +2 state. Both the Auger parameter (1851.3 eV) and the Cu^{2+} satellites shape of the sample CuO bundles are comparable to a CuO reference [82, 87, 13]. However, we note a slight broadening of the peak towards higher binding energy, due to the existence of another phase in low amount, most probably $Cu(OH)_2$.

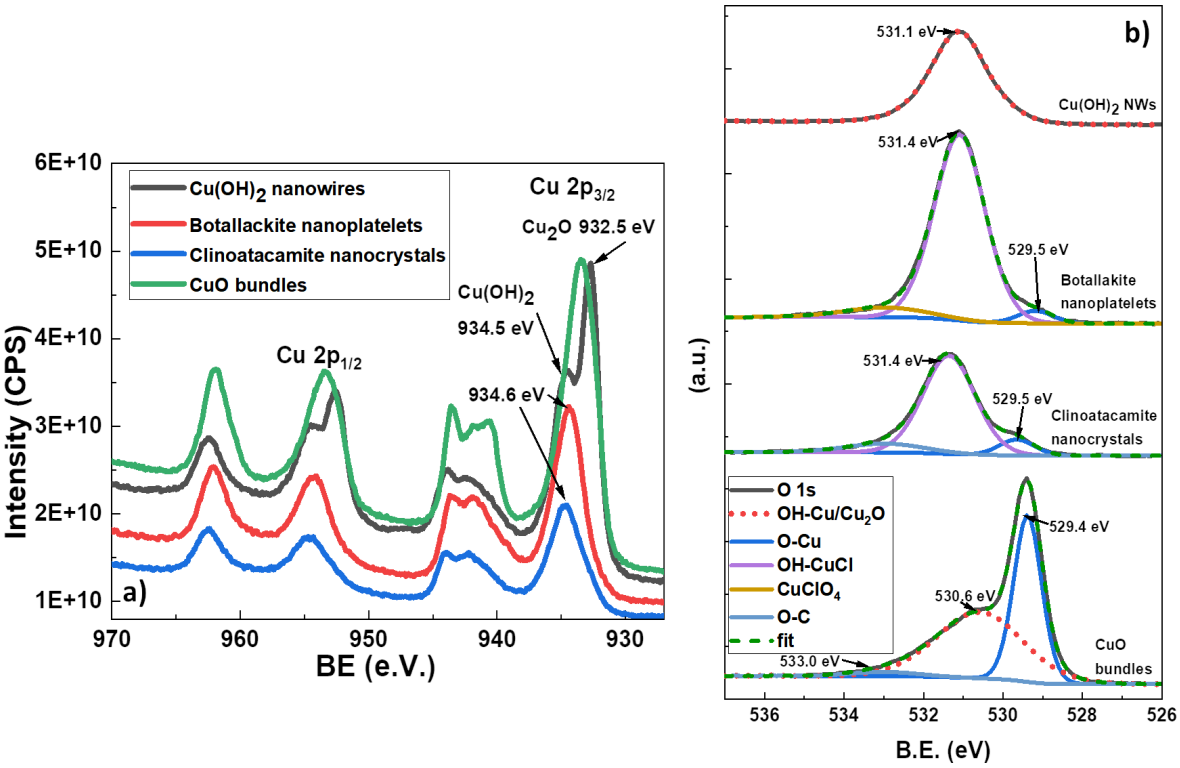

Figure 3.11: XPS spectra of as deposited Cu based nanostructures a) Cu 2p peaks, b) O1s peaks. The observed spectrum is in black while the fit, shown as dashed green line, is calculated based on combination of all the components mentioned in the legend for figure b).

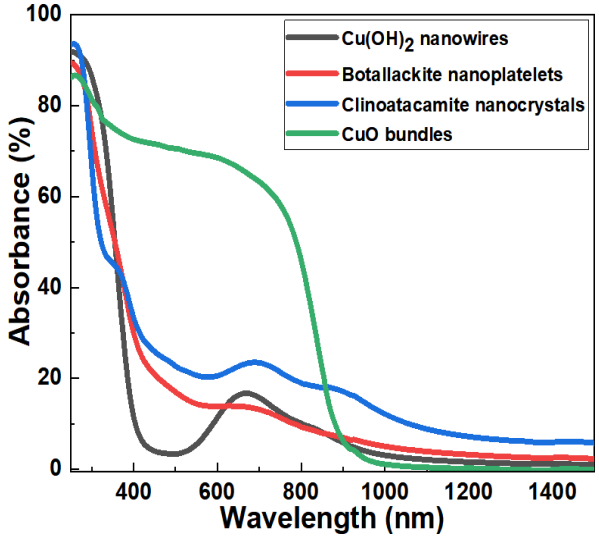

Figure 3.12: Absorption spectra of Cu based nanostructures as deposited on glass substrate

Although the Auger parameter is a powerful method to determine the chemical state of an element, and thus to identify the phases incorporating this element, it is limited to the phases or chemical environment easily observable in the phototelectron and Auger peaks, minor phases may be missed. Thus, the investigation was completed with the O 1s peak shown in Figure 3.11 b). The O 1s spectrum of the $Cu(OH)_2$ NWs presents a single contribution at 531.1 eV (FWHM = 1.65 eV) corresponding to both OH-Cu bonds and oxygen atoms in Cu_2O, as previously identified from the Cu 2p spectra. Two main components are observed in the O 1s spectra for the other structures, corresponding to O-Cu (at 529.5 eV) and to HO-CuCl (531.4 eV) for both $Cu_2(OH)_3Cl$ nanoplatelets and nanocrystals. Two components observed in the O 1s spectra for CuO bundles correspond to O-Cu (529.4 eV) and HO-Cu (530.6 eV). These values are in agreement with the data reported in the literature [13]. An additional contribution at higher binding energy (533.0 eV) is due to the presence of O-C bonds.

The change in colour of the solution observed for various products is a primary indicator of the change of optical properties. To confirm it, the absorption spectra of the nanostructures deposited on glass, measured from 250 nm to 1500 nm, are shown in Figure 3.12. The spectrum for $Cu(OH)_2$ NWs shows a broad asymmetric absorption peak with a maximum at 680 nm and a shoulder at 850 nm. The feature at 680 nm is also present in the absorption spectra of both $Cu_2(OH)_3Cl$ nanostructures, with a shift to 700 nm for the peak maximum and to 900 nm for the shoulder. Moreover, the $Cu_2(OH)_3Cl$ nanostructures show higher background absorption in the visible region as compared to $Cu(OH)_2$ NWs, and an onset of the UV absorption at 400 nm.

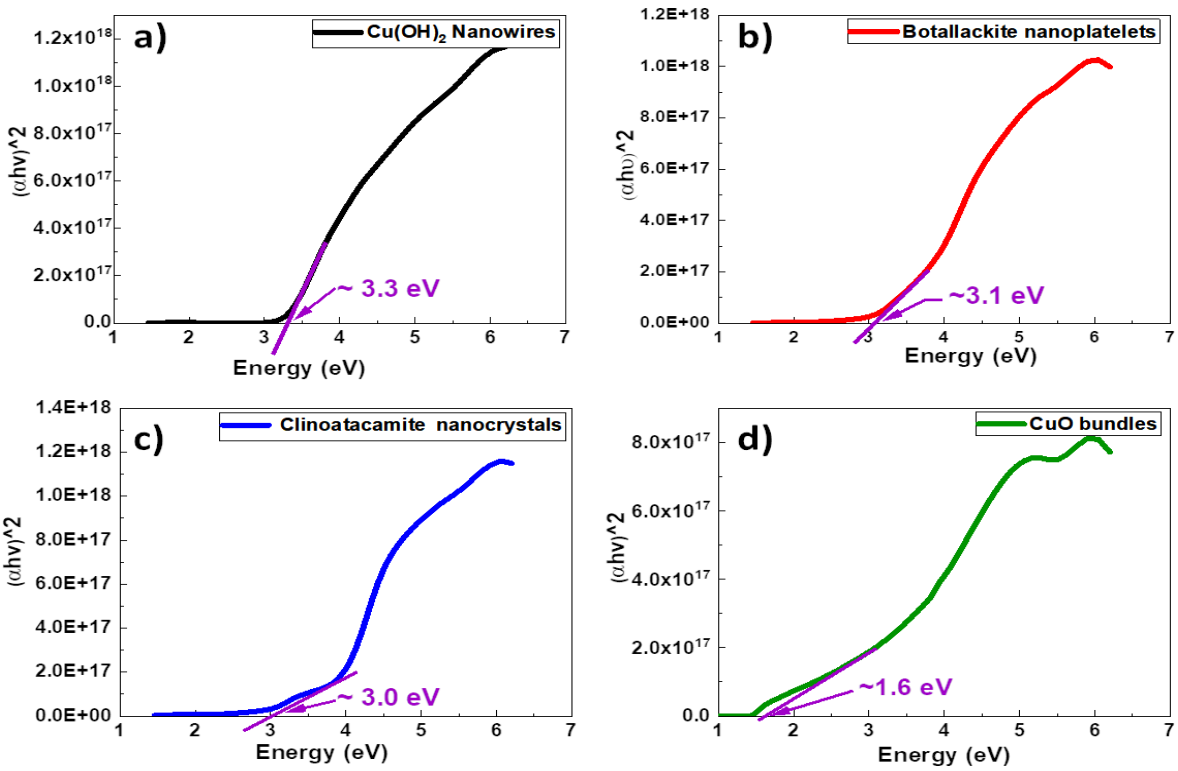

Figure 3.13: Direct band gap Tauc plots calculated and plotted for (a) $Cu(OH)_2$ NWs, (b) Botallackite $Cu_2(OH)_3Cl$ nanoplatelets (c) Clinoatacamite $Cu_2(OH)_3Cl$ nanocrystals and (d) CuO bundles

The broad peak at 650 nm - 700 nm can be attributed to d-d transitions observed in copper II oxidation state [91, 92]. This peak can be observed in the absorption spectra of $Cu(OH)_2$ NWs, botallackite nanoplatelets and clinoatacamite nanocrystals, alike. For clinoatacamite nanocrystals, the absorption around 400 nm could be related to the band gap transitions. CuO bundles show the characteristic absorption in the visible range from 400 nm to 800 nm due to transitions across the band gap as also observed by Zhang and coworkers [93]. The band gap of the materials can be calculated by using a Tauc plot based on the measured absorption spectrum (Figure 3.13). From Tauc plot calculations, the band gap of $Cu(OH)_2$ NWs is found to be 3.3 eV in our case which is close to 3.08 eV mentioned in the literature [94]. The direct band gap of botallackite nanoplatelets is calculated to be 3.1 eV while that of clinoatacamite nanocrystals is 3.0 eV. The band gap of CuO bundles is found to be 1.6 eV, which is close to 1.2 eV mentioned in the literature [95].

A discussion on morphology change in Cu based nanostructures

This sub section in entirely taken as it is, from discussion part of the article published based on word done during this thesis [83].

We discuss the hypothesis and build rationales for the control of the nanostructure morphology and composition demonstrated in our work. We explain the formation of $Cu(OH)_2$ NWs and debate on the effect of precursors with the help of the literature. Then, utilizing the concepts of formation energy and energy above hull, we explain why $Cu(OH)_2$ is bound to convert to other morphologies and compositions on change of a few reaction parameters. Furthermore, we develop hypotheses for conversion of $Cu(OH)_2$ NWs to $Cu_2(OH)_3Cl$ nanoplatelets and nanocrystals.

The formation of $Cu(OH)_2$, in presence of ammonia as a catalyser and sodium hydroxide, in an aqueous solution can be expressed by following chemical reaction.

$$CuCl_2 + 2\,NaOH \xrightarrow{NH_4OH\,(cat\cdot)} Cu(OH)_2 + 2\,Na^+ + 2\,Cl^-$$

The development of NWs is a two step process, viz. formation of nuclei and coalescence into nanowire. The NWs formed are of different lengths between 3 μm and 6 μm. This suggests that there is nucleation occurring at various times in the solution indicating simultaneous occurrence of the two steps.

Luo et al. have studied the effect of the reactant salt on the morphology of the $Cu(OH)_2$ nanostructures[96]. They compared $CuCl_2$, copper sulphate ($CuSO_4$) and copper nitrate ($Cu(NO)_3$) as precursors with aminoethanol, and found that only the use of $Cu(NO)_3$ led to $Cu(OH)_2$ NWs.

Table 3.3: Crystal structure and related formation energy and energy above hull for the different copper hydroxide based nanostructures [97]. Taken from [83].

Nanostructure	Crystal lattice	Space group	Formation energy (eV)	Energy above hull (eV)
$Cu(OH)_2$ NWs	Orthorhomic	Cmcm	-1.11	0.107
Botallackite	Monoclinic	$P2_1/m$	-1.119	0.043
Clinoatacamite	Rhombohedral	$R\bar{3}m$	-1.116	0.046

$CuCl_2$ is used as a source of Cu^{2+} in our work, which is similar to the work of Xu and co-workers [85]. The difference in the results observed by Luo et al. and the $Cu(OH)_2$ NWs results presented here could be linked to concentration of the reactants or the base used in the reaction. Luo et al. have used aminoethanol as a base, while here we have used ammonia and sodium hydroxide. According to Luo et al. , the role of ammonia is to stabilize the positively charged copper hydroxide building units and to restrict the growth of the crystal in [100] direction. They also found that NaOH, itself, was not sufficient for precipitation of $Cu(OH)_2$ NWs. In contrast to this, we were able to synthesize $Cu(OH)_2$ NWs by just mixing $CuCl_2$ and NaOH. However, some part of the Cu^{2+} source was still left unreacted in this particular experiment without ammonia. Thus, we can assume that ammonia may act as a catalyser in utilising the Cu^{2+} ions in the solution. The concentration of NaOH used also plays a role in the formation of $Cu(OH)_2$ NWs. Luo et al. used only 0.8 mM of NaOH while 6.92 mM was used in our case. Higher concentration of NaOH, even in absence of ammonia as a catalyser, leads to a more basic environment and eventually to a precipitation of $Cu(OH)_2$ NWs.

In order to explain the observed transformations and the phase diagram presented in Figure 3.9, the crystal structure of the nanostructures and energies related to them are summarized in table 3.3. The data in table 3.3 are sourced from the XRD spectra and article by Jain et al. [97] The formation energy of a material is directly related to it's stability. The more negative the formation energy the more stable the compound is as compared to it's constituent elements. The negative formation energy of all the compounds indicates that energy was released when the compound was formed. On the other hand, the energy above hull is a positive quantity, and characterises the thermodynamic stability of the compound as compared to other phases [98]. Based on this $Cu(OH)_2$ is the least stable and expected to convert to other stable materials depending on the environment around it. Krivovichev et al. examine the validity of Goldmsmith's simplexity rule in case of $Cu_2(OH)_3Cl$ polymorphs. They state that since the $Cu_2(OH)_3Cl$ polymorphs have different crystal structures, one can interpret that

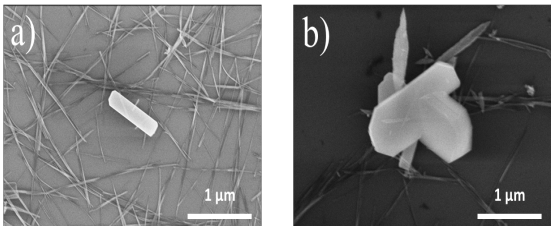

Figure 3.14: a) as prepared botallackite nanoplatelets, b) botallackite nanoplatelets sampled after 48 hours in mother solution at pH 6. Taken from [83].

the transformations between these phases have reconstructive character, meaning it involves breaking of chemical bonds and formation of new ones [99].

On reducing the pH of $Cu(OH)_2$ NWs at higher temperature, $Cu_2(OH)_3Cl$ compounds are formed. According to the Hard Soft Acid Base (HSAB) theory, Cu^{2+} is a borderline Lewis acid. OH^- and Cl^- are both hard Lewis bases. This makes it difficult to predict which anion will form a compound with Cu^{2+} based on HSAB theory only. In the condition for the formation of $Cu(OH)_2$, the concentration of Cl^- ions in the solution is close to 4.87 mM while that of OH^- ions is 31.62 mM. When the solution is heated to 70 °C, the pH of the solution changes from 12.5 to 11.5. On addition of 2.5 mL of 2 M HCl, the pH of the solution further reduces to 6. The Cl^- ion concentration at this stage is about 47.92 mM while that of OH^- ions drastically reduces to 0.08 μM. The increase of the Cl^- concentration may lead to trapping of this ion in the crystalline basic salt of $Cu(OH)_2$ by replacing one OH^- ion resulting in formation of botallackite.

As Krivovichev reminds, the Ostwald step rule states that in a crystallizing system, first a sequence of metastable phases is formed before forming the stable phase [99]. Goldsmith, in his paper, explains that nucleation and growth of phases with higher simplexity are favored in many cases of polymophs over more stable compounds with lower simplexity [100]. To apply this rule in the case of formation of $Cu_2(OH)_3Cl$ or clinoatacamite, it would mean that an intermediate compound like botallackite may form, which is less stable but has a higher simplexity than clinoatacamite.

Pollard et al. claim that this is an intermediate phase and will change to clinoatacamite when kept in mother solution for long duration [101]. We show here that the botallackite phase can be stabilized by the controlled pH and temperature. When kept in the mother solution at pH 6 for 48 hours, botallackite nanoplatelets are found to retain their shape as shown in Figure 3.14 . Thus, we have successfully stabilised the intermediate step of botallackite in form of nanoplatelets.

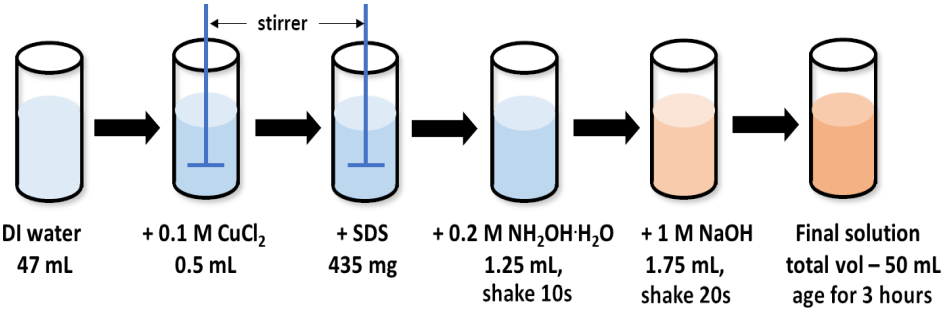

Figure 3.15: Schematic representing synthesis procedure for Cu_2O truncated cubes. Change of solution colour shown as reactants are added is to represent more realistic view of the experimental procedure. The solution changing colour to orange indicates formation of Cu_2O.

A similar observation with incorporation of NO_3^- ions is stated in the work done by Luo et al. [96]. Such observations lead us to believe that the phase diagram in Figure 3.9 is not specific to the use of HCl to reduce the pH of $Cu(OH)_2$NWs. Such a phase diagram could be reproduced using other acids too.

It is observed that, when the pH of botallackite nanoplatelets is reduced further to 5, clinoatacamite nanocrystals start to form. A complete conversion from botallackite nanoplatelets to clinoatacamite nanocrystals takes place at 80 °C at pH of 5. The reason for this observation lies in the space group and stability. Botallackite nanoplatelets are monoclinic with $P2_1/n$ space group while clinoatacamite nanocrystals are rhombohedral with $R\bar{3}m$ space group. When h+k+l = odd in $P2_1/n$ setting, this transforms to half integer indices in hexagonal setting corresponding to Brillouin Zone of $R\bar{3}m$. Malcherek and Schlüter claim that this transition can be due to Jahn-Teller distortion of the regular $Cu(OH)_6$ octahedron [102].

3.1.3 Cu_2O truncated cubes

Another copper based metal oxide, viz. Copper(I) oxide (Cu_2O) is popular among the studied p-type metal oxides and has already been widely investigated for the sensing of ethanol, NO_2, etc. [103, 104]. The main motivation behind working on Cu_2O was to obtain a cube-like morphology and calcinate it to obtain CuO cubes. The CuO cubes were then intended to be used in formation of a ZnO-CuO heterostructure.

For synthesis of Cu_2O truncated cubes, an up-scaled and modified version of the synthesis procedure mentioned by Kuo and Huang is used [105]. In 47 mL DI water, 0.5 mL of 0.1 M of $CuCl_2$ solution and 435 mg of SDS is mixed until dissolved. 1.25 mL of 0.2 M of $NH_2OH \cdot HCl$ is added and the solution is shaken for 10 s. Then, 1.75 mL of 1 M NaOH solution is added and the solution is again shaken for 20

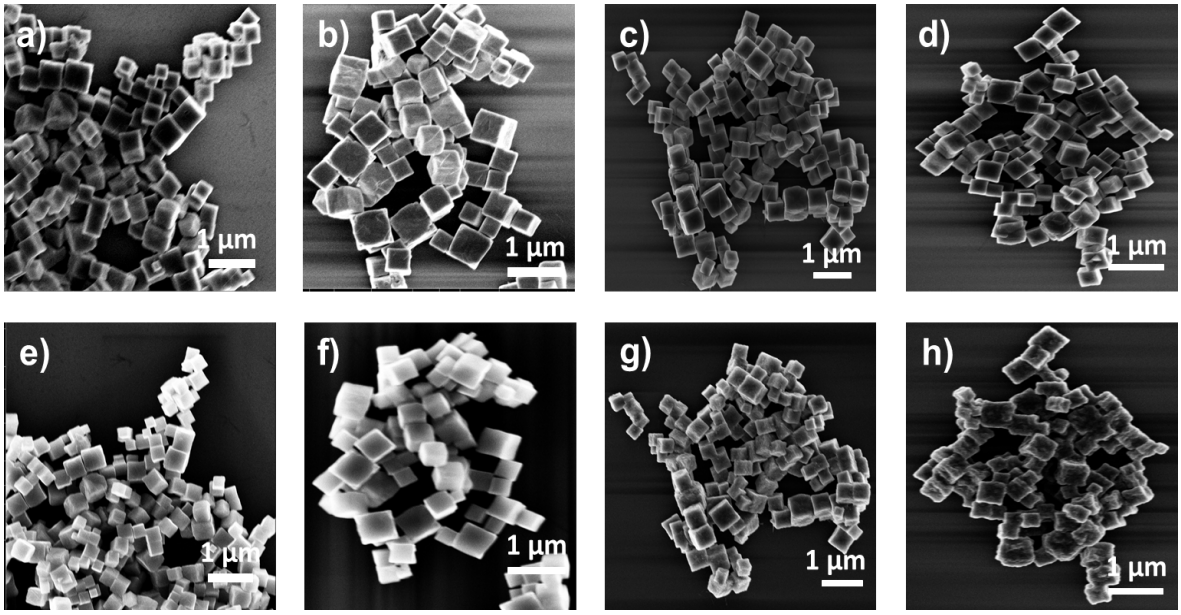

Figure 3.16: SEM image of as prepared and post annealed Cu_2O truncated cubes where a), b), c) and d) are 4 samples of as prepared material while the lower row show the same samples after annealing e) post 100 °C annealed for 2 hours, f) post 200 °C annealed for 2 hours, g) post 300 °C annealed for 2 hours, h) post 400 °C annealed for 2 hours

s. On addition of NaOH, the solution chages colour to green while shaking it changes its colour to yellow. The solution is then kept to age for 3 hours at room temperature and atmospheric pressure where it turns brick red in colour. The brick red coloured precipitate is then centrifuged, washed and stored in absolute ethanol for further analysis. A schematic representation of this procedure is shown in Figure 3.15.

Kuo and Huang explain the growth process of Cu_2O truncated cubes as follows. $Cu(OH)_4^{2-}$ ions are readily formed upon the addition of NaOH and are reduced to Cu_2O by NH_2OH through the following reaction

$$2Cu(OH)_4^{2-} + 2NH_2OH \longrightarrow Cu_2O + N_2 + 5H_2O + 4OH^- \tag{3.1}$$

They observed that the crystal growth is rapid and proposed that Cu_2O seed particles are formed immediately upon addition of the reactants. This is evident by the very quick change in colour of the solution. Smaller crystals of 50 - 100 nm diameter aggregate to form intermediate nanocubes. Simultaneously tiny Cu_2O nanoparticles of 10 - 20 nm diameter, adsorb on the surface of these intermediate nanocubes to finally grow into larger nanocubes. The nanocubes produced have truncated edges and corners, hence the name 'truncated cubes'. [105]

Since the aim was to convert the Cu_2O truncated cubes to CuO while preserving the morphology of the

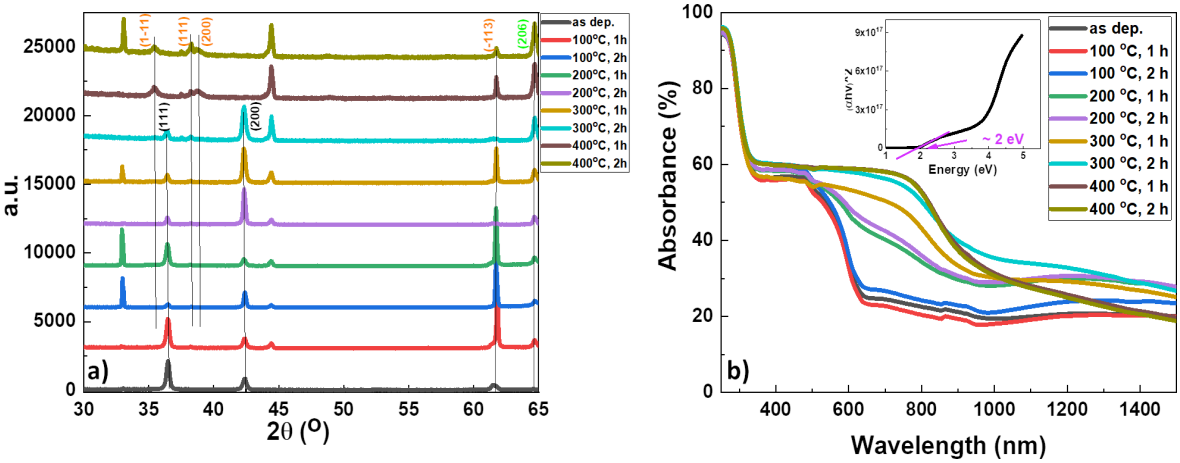

Figure 3.17: Characterisation of Cu_2O truncated cubes showing evolution with annealing a) XRD spectra, b) absorbance spectra with inset of Tauc plot of as deposited Cu_2O truncated cubes

nanostructure, a detailed SEM and XRD annealing study was performed. Figure 3.16 shows SEM pictures of as deposited and post annealed Cu_2O truncated cubes at various temperatures. To observe if there are any specific morphological changes, the SEM image was taken at the same position on the substrate, before and after annealing. Figure 3.16 a) must be directly compared to Figure 3.16 e), Figure 3.16 b) with f) and so on. Comparing the morphology of the Cu_2O truncated cubes before and after annealing, we can safely infer that the annealing does not change the morphology of the truncated cubes.

Figure 3.17 a) shows XRD spectra of Cu_2O truncated cubes with Cu_2O peaks indexed to PDF: 04-007-9767 and Figure 3.17 b) shows absorbance spectra with an inset of a Tauc plot. The strong increase of the absorbance below 600 nm for Cu_2O is due to the inter band transition across the band-gap. Cu_2O truncated cubes show absorption between 300 nm to 600 nm which is a part of the visible spectrum. From a Tauc plot of the data, we estimate the band gap of the respective nanostructures to be 2 eV for Cu_2O truncated cubes, close to 2.1 eV expected for bulk Cu_2O [106].

It is very interesting to see how annealing affects the structural composition and optical characteristics of the Cu_2O truncated cubes. XRD spectra obtained are compared with Cu_2O PDF: 04-007-9767 and CuO PDF:00-048-1548. Figure 3.17 a) reveals that Cu_2O truncated cubes are stable up to 300 °C, but change crystal structure to form CuO when annealed at temperatures equal to or higher than 400 °C for 1 hour. This conversion, which is not expected from the thermodynamic stability of copper oxides, has already been reported for the oxidation of copper thin films [107, 108]. Thus, the maximum temperature at which Cu_2O truncated cubes can be annealed to improve it's properties without changing the composition is 300 °C for 2 hours. Figure 3.17 b) shows the evolution of the optical properties of Cu_2O truncated cubes

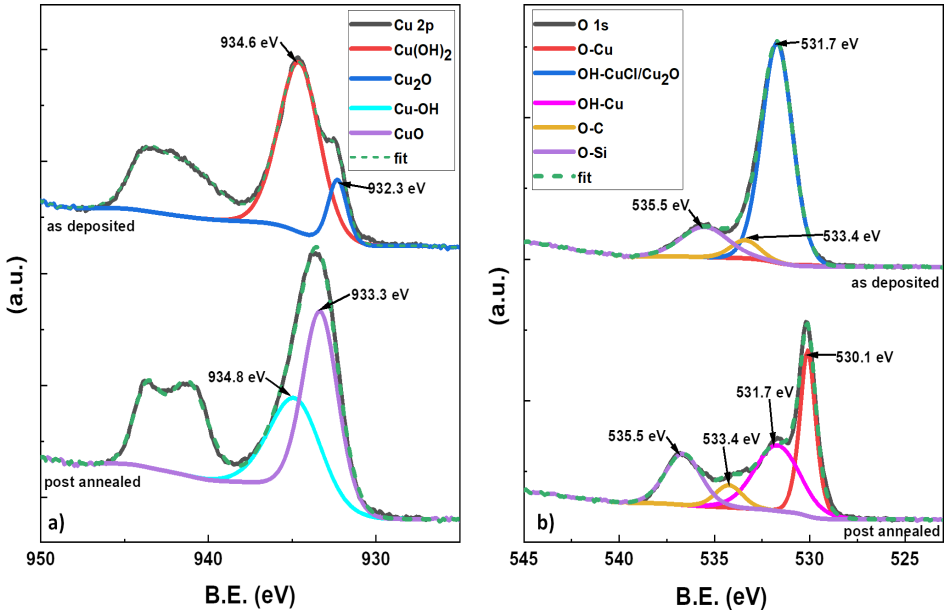

Figure 3.18: XPS spectra a) Cu 2p peak b) O 1s peak of as deposited and post 200 °C annealed Cu_2O truncated cubes. The observed spectrum is in black while the fit, shown as dashed green line, is calculated based on combination of all the components mentioned in the legend.

with annealing. Even though the structural properties do not show any oxidation to CuO till 300 °C 2 h annealing, the absorbance in the visible region already starts to change with 200 °C 1 h annealing. The absorbance in visible range from 400 nm to 800 nm is seen to be at its maximum after 400 °C annealing, indicating complete conversion of Cu_2O truncated cubes to CuO.

Thus, further XPS investigations of as deposited and post 200 °C annealed Cu_2O truncated cubes were carried out to complete the characterisation and study the early stage of the oxidation process. As deposited Cu 2p peak has two contributions, one from $Cu(OH)_2$ at 934.6 eV while the other from Cu_2O at 932.3 eV as shown in Figure 3.18 a). Post annealed Cu 2p peak also has two contribution, however from Cu-OH at 934.8 eV and the other from CuO at 933.3 eV as shown in Figure 3.18 b). Thus, in Cu 2p peak, we can see that Cu_2O changed to CuO even after annealing at only 200 °C while some amount of Cu-OH bonds are retained at the surface. This is rather unexpected from the XRD observations. In the O 1s spectrum of the as deposited Cu_2O truncated cubes, the contributions of O-Cu (530.1 eV), OH-CuCl/Cu_2O (531.7 eV), O-C (533.4 eV) and O-Si (535.5 eV) are observed. (O-Si is observed because Cu_2O was non-uniformly deposited on the sample with large areas of Si wafer exposed.) For post annealed sample however, peak position at 531.7 eV is attributed to OH-Cu. Observing Figure 3.18 c) and d), Cu_2O no longer appears in post annealed sample. It is possible that after 200 °C annealing, the conversion of

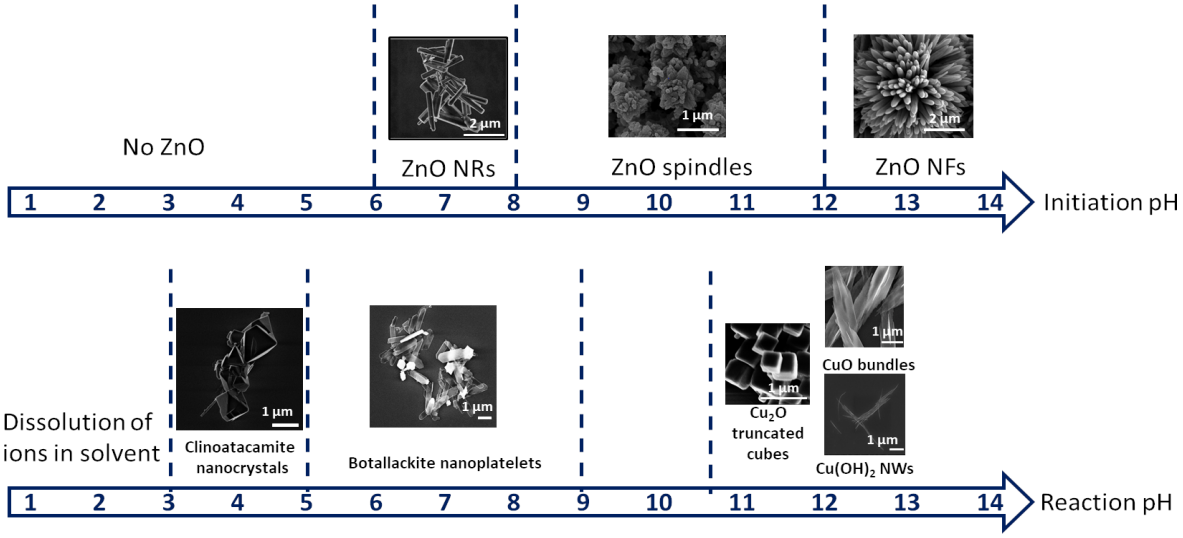

Figure 3.19: Difference in pH range for liquid phase synthesis of ZnO and CuO nanostructures. (images adapted from work done in this thesis and [109].)

Cu_2O to CuO occurs only at the surface and is hence visible in XPS but not in XRD pattern and also affects the absorbance of the material.

3.2 Heterostructures

Liquid phase synthesis of heterostructure is not a straight forward process of combining synthesis procedures of individual nanostructures. In liquid phase synthesis, reaction parameters like initiation pH and temperature, reaction pH and temperature, reaction duration and molarity of constituent ingredients play an important role in determining the morphology and the crystal structure is the nanostructure. Figure 3.19 shows different pH ranges at which different ZnO and CuO nanostructures are known to be synthesised. Although other reaction parameters are not shown in the figure, just observing pH scale, we can infer that simple mixing of the synthesis procedures will not lead to heterostructure formation.

The pH limitation can be overcome in two ways. One, synthesise ZnO NRs that are stable in the pH and temperature range of the target CuO nanostructure. Then, add ZnO NRs in the solution before CuO nanostructure precursor and follow the synthesis procedure so that CuO nanostructures grow on the preexisting ZnO NRs. This approach was used in synthesis of ZnO NRs + $Cu_2(OH)_3Cl$ nanoplatelets heterostructure. In the second approach, we start with a CuO based nanostructure which is stable in pH and temperature range of ZnO nanostructure and follow the stepped synthesis. This approach is adapted in the synthesis of ZnO NFs + CuO truncated cubes.

It is a challenge to work around the specific reaction conditions and find a way to be able to obtain both the nanostructures in solution together and have a naturally grown heterojunction between them. This challenge is overcome in this thesis, particularly for ZnO and CuO nanostructures. Quite often this leads to a multi step synthesis procedure as can be seen in the following subsections.

3.2.1 ZnO NRs + $Cu_2(OH)_3Cl$ nanoplatelets

Synthesis of the heterostructure is a multi step process as described in Figure 3.20 a) and b). The first step is the synthesis of ZnO NRs already described in subsection 3.1.1. The fabricated ZnO NRs are washed before further use. 1 ml, 1 M solution of $CuCl_2$ is added to 5 mL of ZnO NRs solution and the mixture is centrifuged. Next, the procedure used for synthesis of $Cu(OH)_2$ NWs is followed with a new step of addition of ZnO NRs + $CuCl_2$ solution along with ammonia and NaOH. Once the $Cu(OH)_2$ NWs precipitate, the solution is heated to 70 °C. Under 500 rpm stirring, 2 M HCl is added to the solution to bring down the pH to 7. The mixture is then cooled down to room temperature. The precipitate is centrifuged, washed and stored in absolute ethanol.

Figure 3.20 c) shows an SEM image of the precipitate. We observe that a heterostructure is formed with $Cu_2(OH)_3Cl$ nanoplatelets attached around the sides of hexagonal ZnO NRs. $Cu_2(OH)_3Cl$ nanoplatelets are seen to cover all the 6 exposed surfaces of the ZnO NRs in an uneven fashion and seem to be connected from shorter side of the nanoplatelet to the ZnO NR. This forms the typical morphology observed for heterostructure which may have conduction channel model described in Figure 1.4 a).

This is a novel heterostructure. Thus, it is extremely important to make a detailed characterisation. In the following text, as deposited heterostructure is referred to as ZnO NRs + $Cu_2(OH)_3Cl$ nanoplatelets heterostructure while annealed heterostructure is referred to as CuO@ZnO heterostructure.

Figure 3.21 a) shows the XRD spectrum of the as deposited ZnO NRs + $Cu_2(OH)_3Cl$ nanoplatelets heterostructure. The peaks observed in the heterostructure are attributed to various possible component element materials of the heterostructure i.e. with ZnO NRs (PDF: 01-089-1397) and $Cu_2(OH)_3Cl$ nanoplatelets (PDF: 00-058-0520). Some of the peaks also corresponded to CuO (PDF: 00-048-1548). The heterostructure is likely composed with a mix of these phases or structures.

Figure 3.21 b) shows absorbance spectra of as deposited ZnO NRs + $Cu_2(OH)_3Cl$ nanoplatelets heterostructure in orange. For comparison, absorbance spectra of ZnO NRs and $Cu_2(OH)_3Cl$ nanoplatelets is also shown. We can see that the absorbance spectrum of the heterostructure is not just a simple addition of the spectra of the constituent materials. Instead, it has increased absorbance in the visible wavelength range from 400 nm to 900 nm. This is an indication that the heterostructure is not

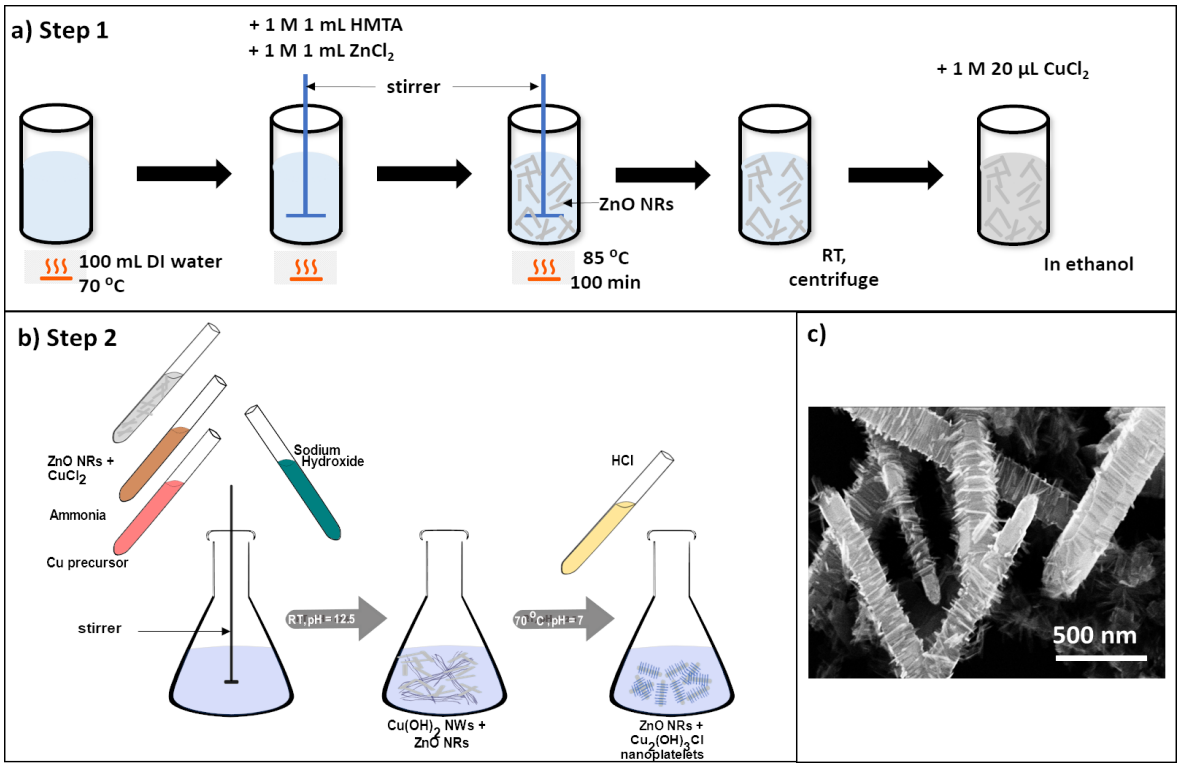

Figure 3.20: Schematic representing synthesis procedure of ZnO NRs + $Cu_2(OH)_3Cl$ nanoplatelets heterostructure. a) Step 1: Synthesis of ZnO NRs, b) Step 2: Synthesis of ZnO NRs + $Cu_2(OH)_3Cl$ nanoplatelets heterostructure. c) SEM image of as deposited ZnO NRs + $Cu_2(OH)_3Cl$ nanoplatelets heterostructure

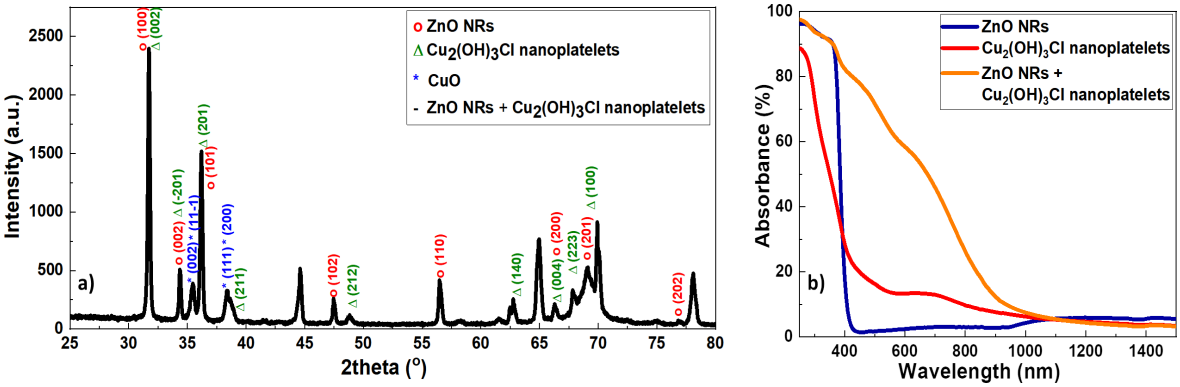

Figure 3.21: a) XRD spectrum of as deposited ZnO NRs + $Cu_2(OH)_3Cl$ nanoplatelets heterostructure with peaks identified from components PDF (ZnO: PDF card-, $Cu_2(OH)_3Cl$ nanoplatelets: PDF card-, CuO: PDF card-) b) Absorbance spectra of as deposited ZnO NRs + $Cu_2(OH)_3Cl$ nanoplatelets heterostructure, ZnO NRs and $Cu_2(OH)_3Cl$ nanoplatelets shown together for comparison

merely a mixture of two materials but that formation of the heterostructure has changed the optical properties of the constituent nanostructures.

Figure 3.22 shows SEM pictures of as deposited ZnO NRs + $Cu_2(OH)_3Cl$ nanoplatelets and post annealed CuO@ZnO heterostructure at various temperatures. Just like Cu_2O truncated cubes, the SEM image was taken at the same position on the substrate, before and after annealing, to observe if there are any specific morphological changes. Figure 3.22 a) must be directly compared to Figure 3.22 e), Figure 3.22 b) with f) and so on. Comparing the morphology of the heterostructure before and after annealing, we can safely infer that the annealing does not case any morphological changes.

We further studied the effect of annealing on the structural and optical properties of the heterostructure shown in Figure 3.23. Let us consider evolution of structural characteristics in terms of XRD spectra as shown in Figure 3.23 a). Peaks at 16.71° corresponding to paratacamite (PDF: 04-012-5828) and 23.8° corresponding to $Cu(OH)_2$ (PDF: 00-018-0420) disappear post 200 °C annealing while peaks at 15.5° corresponding to botallakite (PDF: 00-058-0520) and at 16.2° corresponding to $Cu(OH)_2$ disappear post 300 °C annealing. Peaks at 31.7°, 34.3°, 36.2°, 47.4° and 56.5° corresponding to ZnO (PDF: 01-089-1397) and at 64.7° corresponding to $Cu(OH)_2$ appear in XRD spectra of the heterostructure after all the stages of annealing. Peak at 33° in post 100 °C annealed sample is an artefact and not observed again on repetition of measurement. Peaks at 35.5°, 38.9°, and 61.7° corresponding to CuO (PDF: 00-048-1548) appears after 200 °C annealing, strengthens after 300 °C annealing and disappears with annealing, respectively. Peak at 38.1° corresponding to atacamite (PDF: 01-077-016) strengthens after 300 °C annealing while

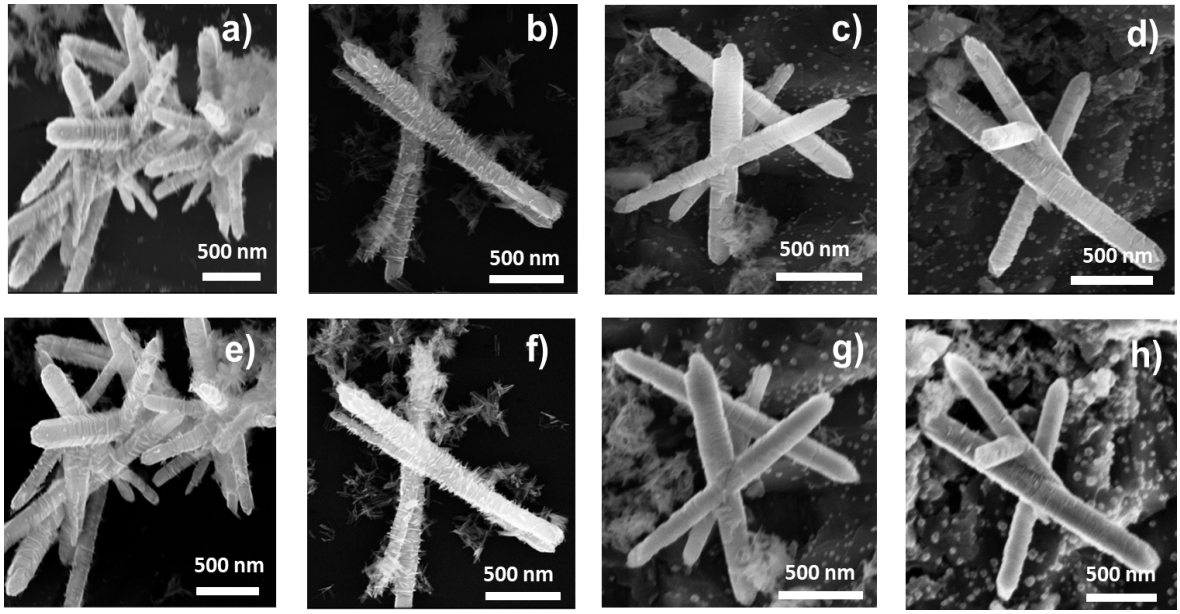

Figure 3.22: SEM images of as prepared ZnO NRs + $Cu_2(OH)_3Cl$ nanoplatelets and post annealed CuO@ZnO heterostructure where a), b), c) and d) are of as prepared while e) post 100 °C annealed for 2 hours, f) post 200 °C annealed for 2 hours, g) post 300 °C annealed for 2 hours, h) post 400 °C annealed for 2 hours

one at 62.1° corresponding to paratacamite appears after 400 °C annealing of the heterostructure. Thus, on evolution through annealing, ZnO NRs + $Cu_2(OH)_3Cl$ nanoplatelets heterostructure reduces its copper hydroxide bonds and strengthens its copper oxide bonds, all the while, not affecting ZnO crystal structure in any way.

Figure 3.23 b) shows the evolution of absorbance spectra with annealing temperatures for heterostructure. We observe that as deposited heterostructure shows absorbance in visible region reducing steadily from 400 nm to 900 nm. As the annealing temperature is increased we observe that absorption percentage in the visible region strongly rises with a maximum absorption in visible region from 400 nm to 800 nm for 300 °C and 400 °C annealed heterostructure sample. Also, a sharp drop in absorbance is seen for wavelengths just outside visible spectrum for these high temperature annealed heterostructure samples. This increase of absorption in visible region could also be an indication of increased amount of CuO in the heterostructure after annealing.

Further elemental characterisation of ZnO NRs + $Cu_2(OH)_3Cl$ nanoplatelets heterostructure was carried out via XPS for as deposited and post 400 °C annealed CuO@ZnO heterostructure samples. XPS analysis corresponding to Cu 2p and Zn 2p are shown in Figure 3.24 while that corresponding to O 1s and Cl 2p

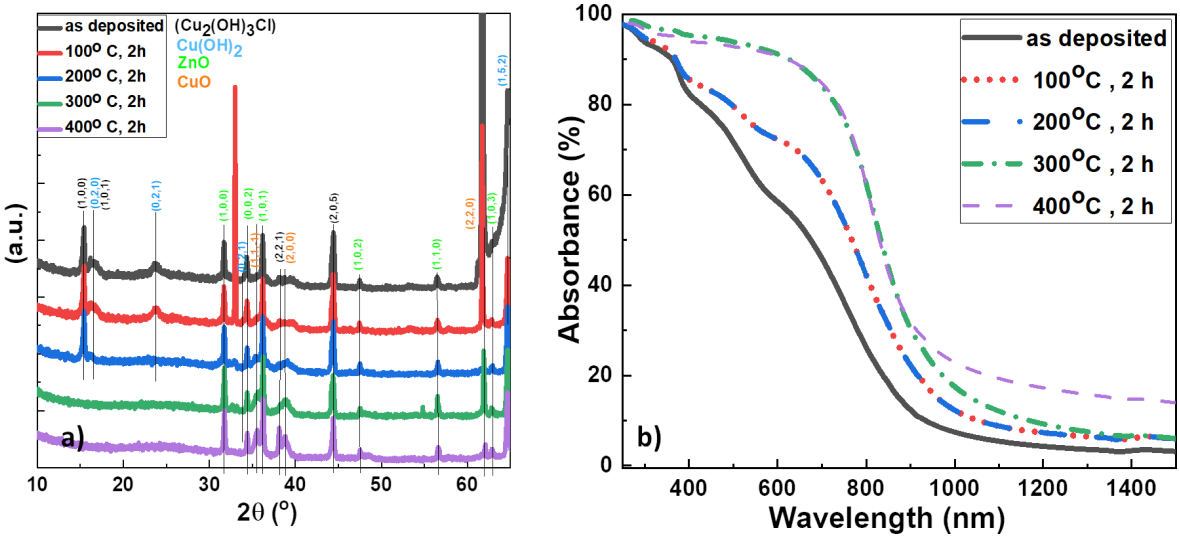

Figure 3.23: Effect of annealing on structural and optical characteristics of ZnO NRs + $Cu_2(OH)_3Cl$ nanoplatelets heterostructure. a) XRD spectra and b) Absorbance spectra of ZnO NRs + $Cu_2(OH)_3Cl$/CuO nanoplatelets heterostructure annealed at different temperatures.

is shown in Figure 3.25. Cu 2p peak fit was achieved by integrating experimentally observed spectra for CuO bundles and $Cu_2(OH)_3Cl$ nanoplatelets. Comparing Cu 2p peak for as deposited and post annealed heterostructure (Figure 3.24 a) and b), respectively), we observe that contribution of CuO (at 933.4 eV as deposited and 932.9 eV post annealed) to the peak fit increases after annealing. Also, contribution to the fit of $Cu_2(OH)_3Cl$ (at 934.8 eV as deposited and at 934.1 eV post annealed) reduces after annealing. This is an additional proof to the earlier observed fact in XRD and absorbance spectra of the heterostructure confirming that there is indeed more CuO in the heterostructure after annealing. Comparing Figure 3.24 c) and d), we confirm that Zn (at 1021.7 eV) does not undergo any change in it's oxidation state after annealing in the heterostructure.

Oxygen is connected in bonds to multiple elements in the heterostructure. Observing the as deposited and post annealed heterostructure sample O 1s spectra in Figure 3.25 a) and b), we see that the contribution from O-CuCl (531.3 eV) and OH (531.3 eV) bond decreases drastically while the contribution from O-Cu (529.4 eV) bond increases significantly after annealing. This adds on as supporting argument to the increase of CuO in post annealed heterostructure. Figure 3.25 c) and d) show as deposited and post annealed heterostructure Cl 2p spectra where the Cl $2p_{3/2}$ and Cl $2p_{1/2}$ peaks at 198.7 eV and 200.4 eV, respectively, corresponding to metal-chloride bonds. One can note the FWHM of these contributions is lower after annealing, meaning the number of phases including chloride atoms is lower or there is less variation of the x value in the $Cu_2(OH)_3{-}xCl_x$ stoichiometry.

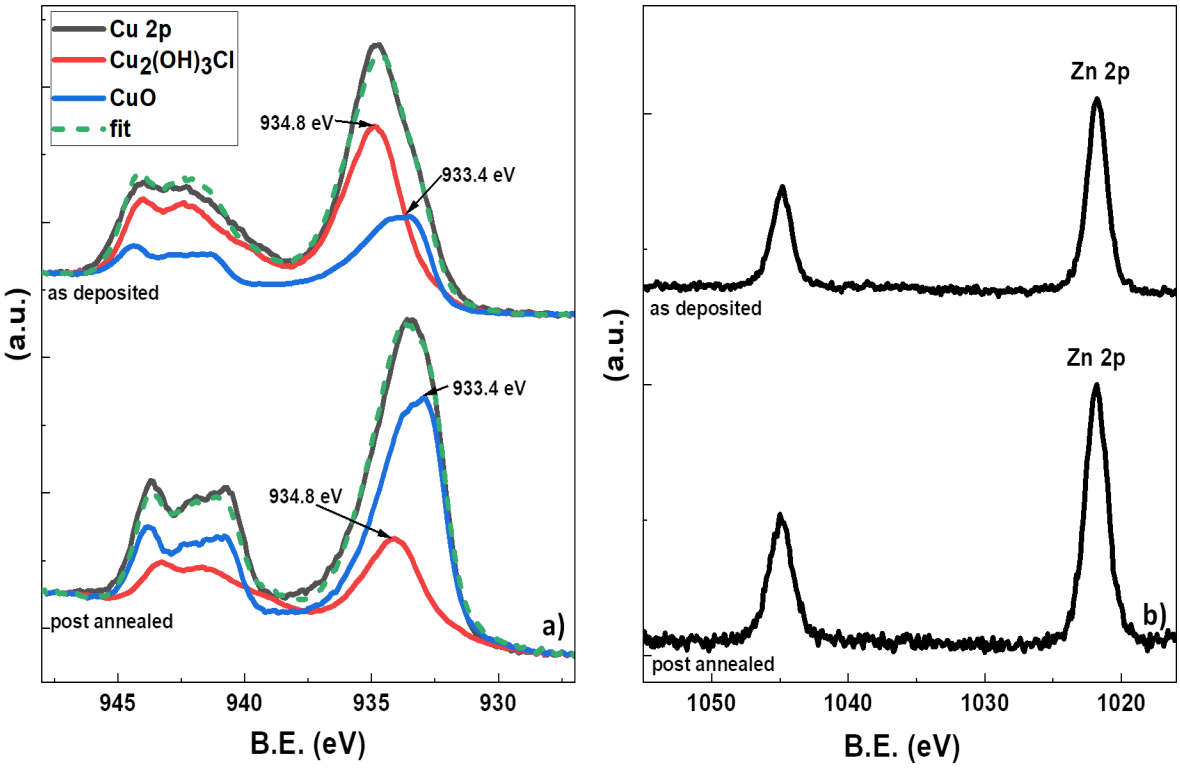

Figure 3.24: XPS spectra a) Cu 2p peak c) Zn 2p peak of as deposited ZnO NRs + $Cu_2(OH)_3Cl$ nanoplatelets and post 400 °C annealed CuO@ZnO heterostructure. for a) the observed spectrum is in black while the fit, shown as dashed green line, is calculated based on combination of all the components mentioned in the legend.

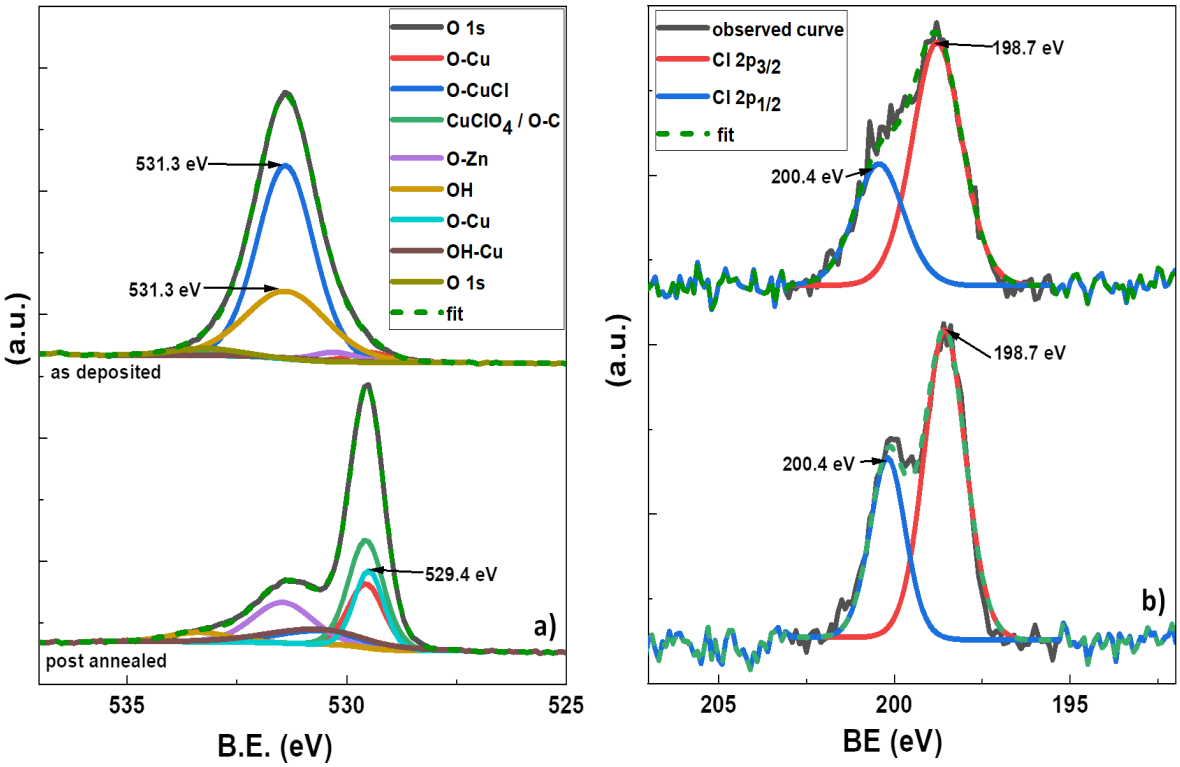

Figure 3.25: XPS spectra a) O 1s peak c) Cl 2p peak of as deposited ZnO NRs + $Cu_2(OH)_3Cl$ nanoplatelets and post 400 °C annealed CuO@ZnO heterostructure. The observed spectrum is in black while the fit, shown as dashed green line, is calculated based on combination of all the components mentioned in the legend.

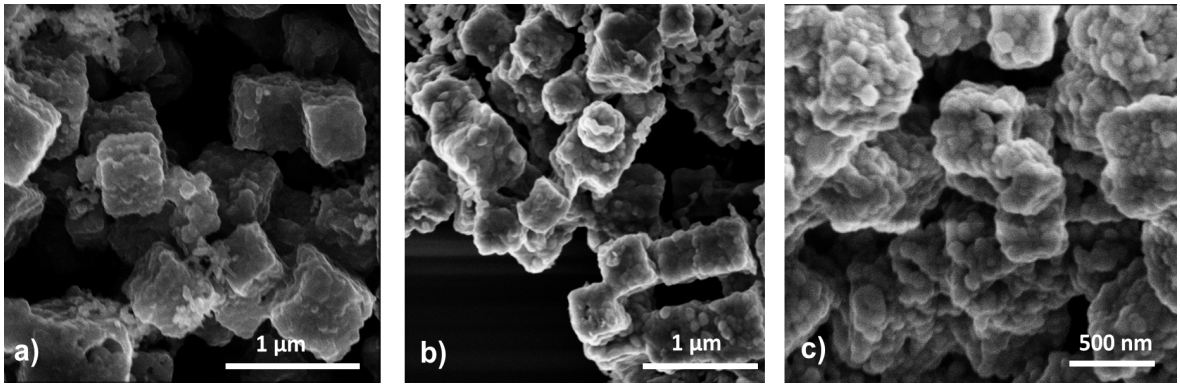

Figure 3.26: SEM image of a) Oven dried and b) Freeze dried Cu_2O truncated cubes, c) Calcinated CuO truncated cubes

3.2.2 ZnO NFs + CuO truncated cubes

The second approach to fabricating a heterostructure needs a CuO based 'seed' nanostructure on which ZnO nanostructure can grow. Thus, we start here with annealed Cu_2O truncated cubes, hereafter referred as CuO truncated cubes, as they provide cubic surfaces for ZnO NRs to grow. It must be noted that this is an attempt at a heterostructure and characterisation will help us determine whether we were successful at fabricating one or not.

Like the previously mentioned heterostructure, synthesis of ZnO NFs + CuO truncated cubes is also a multi step and slightly longer process described in Figure 3.27 a) - c). It starts with synthesis of Cu_2O truncated cubes already described in subsection 3.1.3. Once the Cu_2O truncated cubes are washed and stored in ethanol, they are dried in oven at 60 °C over 24 hours. Another way to dry is to use the freeze drier. However, no difference was found in the quality of drying and the drying process did not affect the morphology of the Cu_2O truncated cubes (see Figure 3.26 a) and b)). The dried Cu_2O truncated cubes were then calcinated at 550 °C for 4 hours in a furnace in air atmosphere, based on the work done by Li et. al. [28]. The calcination process changes the Cu_2O to CuO while maintaining the morphology of the truncated cubes as shown in figure 3.26 c). In the next and the last step of the synthesis, 1 mL of already prepared ZnO nanoparticles solution is added to 5 mL of CuO truncated cubes in water. The mixture is centrifuged and added to 100 mL DI water at 70 °C. The procedure for synthesis of ZnO NRs, described in subsection 3.1.1, is followed next. After 100 minutes, the solution is allowed to cool down to room temperature and centrifuged. The precipitates are the washed and stored in absolute ethanol.

Figure 3.27 d) shows the SEM image of the ZnO NFs + CuO truncated cubes. In SEM images we largely see only ZnO NFs, while CuO truncated cubes are not seen. This could be because quantitatively

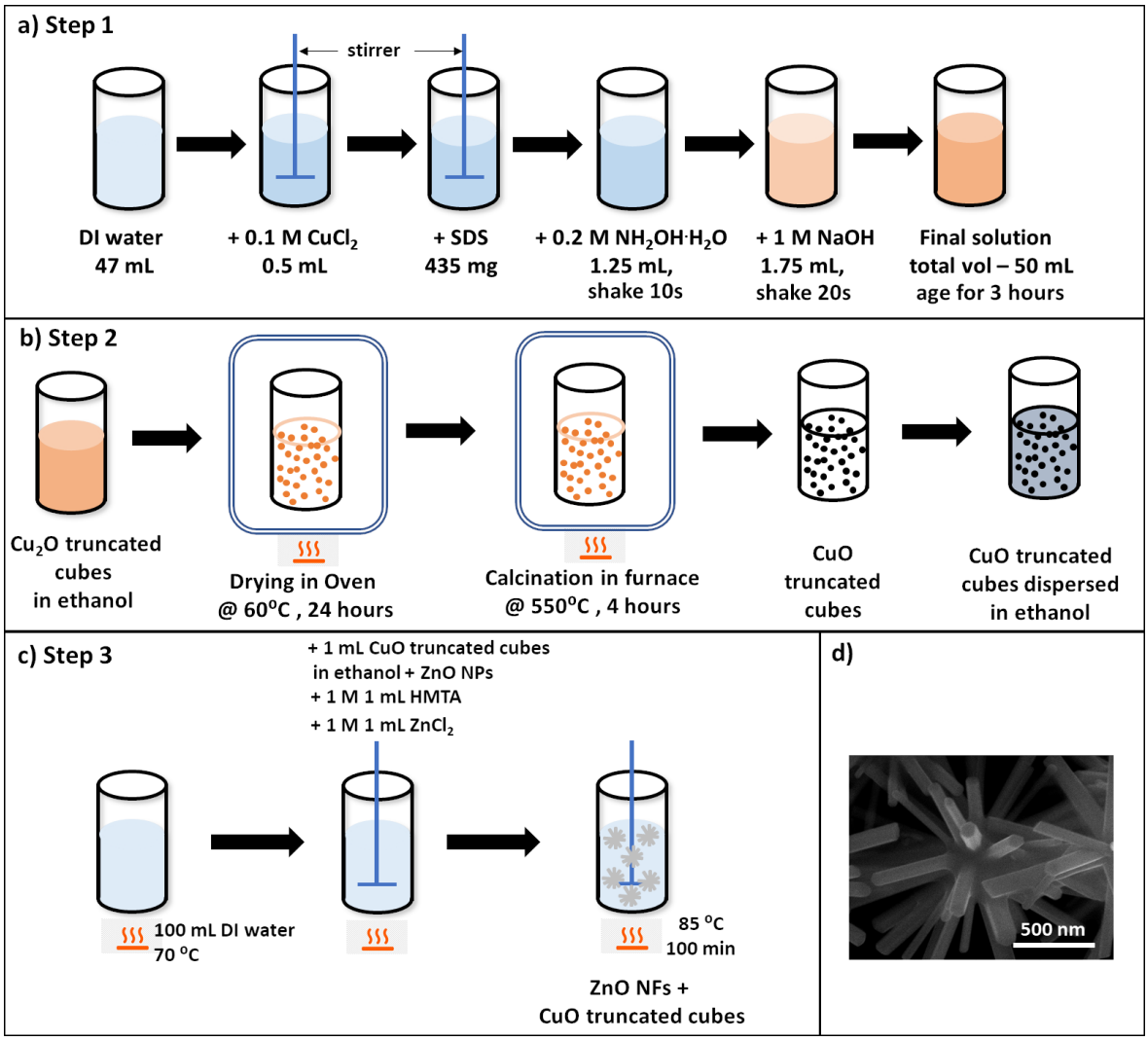

Figure 3.27: Schematic representing synthesis procedure of ZnO NFs + CuO truncated cubes a) Step one: Synthesis of Cu_2O truncated cubes, b) Step two: Drying and calcination of Cu_2O truncated cubes to convert it to CuO, c) Synthesis of ZnO NFs incorporating CuO truncated cubes. d) SEM image of ZnO NFs + CuO truncated cubes.

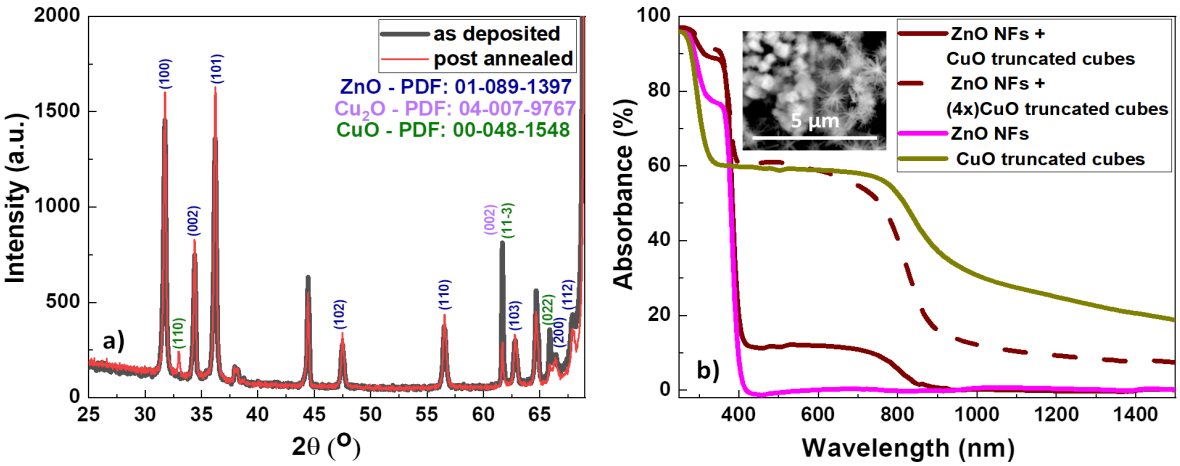

Figure 3.28: a)XRD spectra of as deposited and post annealed ZnO NFs + CuO truncated cubes material. b) Absorbance spectrum of as deposited ZnO NFs + CuO truncated cubes displayed in comparison with absorbance spectra of ZnO NFs and CuO truncated cubes. The dashed line corresponds to absorbance spectrum of ZnO NFs + CuO truncated cubes material with 4 times the amount of CuO truncated cubes indicated by (4x) in the legend. Inset in b) shows SEM image of same sample as used for absorbance spectra measurement showing presence of mixture of CuO truncated cubes and ZnO NFs.

there are more ZnO NFs present in the mixture than CuO truncated cubes.

XRD spectra of as deposited and post 200 °C, 2 h annealed ZnO NFs + CuO truncated cubes is observed and displayed in Figure 3.28 a). Peaks were analysed and attributed to constituent elements ZnO, CuO and Cu_2O. As one can see, there is not much change in the spectra before and after annealing. Most of the peaks observed can be attributed to ZnO (PDF: 01-089-1397). Peak at 32.99° after annealing, at 61.67° and 65.87°, both before and after annealing, can be attributed to CuO (PDF: 00-048-1548). Peak at 32.99° appearing only after annealing could be an indication that annealing process causes exposure of additional CuO in the material. Peak at 61.67° can also be attributed to Cu_2O (PDF: 04-007-9767). These peaks are indicative of presence of CuO.

Figure 3.28 b) shows the absorbance spectrum of as deposited ZnO NFs + CuO truncated cubes in comparison with absorbance spectra of ZnO NFs and Cu_2O truncated cubes. It can be clearly seen that ZnO NFs + CuO truncated cubes shows absorbance in visible spectrum between 400 nm to 800 nm, which is not the case for ZnO NFs. This clearly indicates the presence of CuO alongside ZnO NFs. When molar ratio of Zn:Cu is changed in the synthesis procedure by adding 4 times more CuO truncated cubes during the synthesis, the corresponding absorbance spectrum shows an increase in visible region absorbance, which is known to be a characteristic of CuO. This inspired us to take an SEM picture of the same sample as

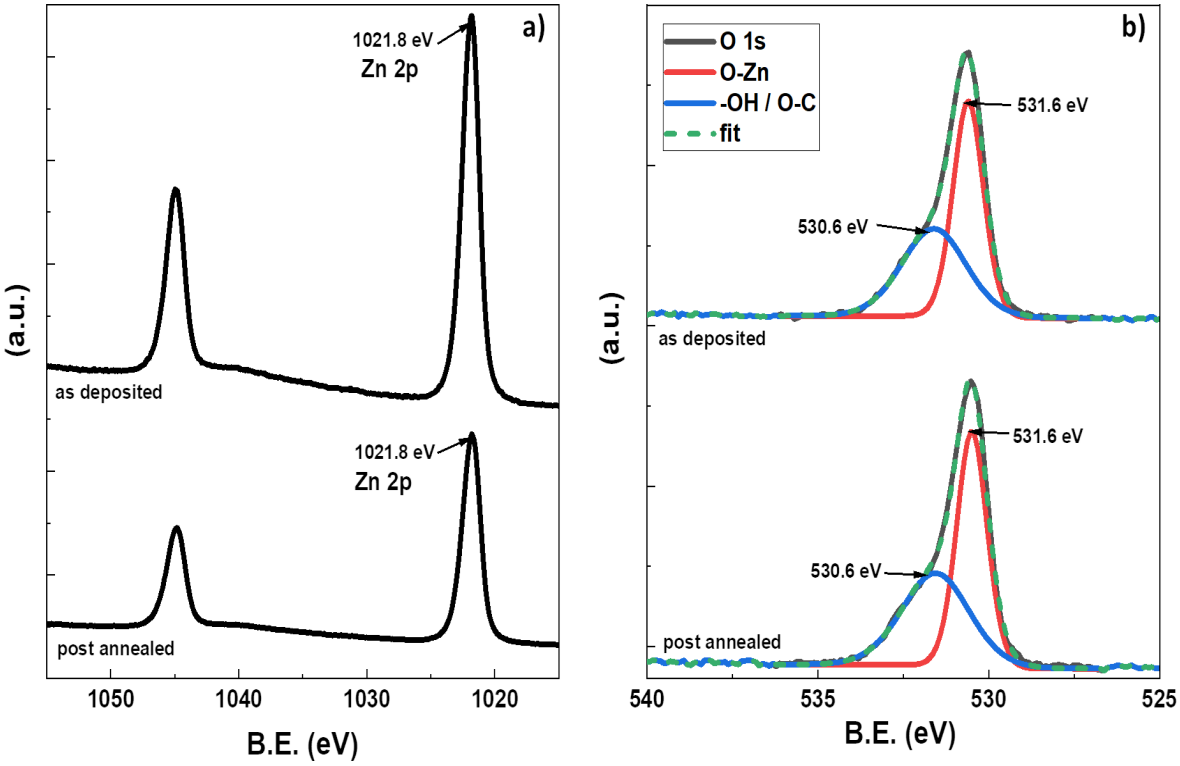

Figure 3.29: XPS spectra of a) Zn 2p peak c) O 1s peak as deposited and post annealed ZnO NFs + CuO truncated cubes heterostructure.

used for absorbance spectra. This SEM image is shown as inset in Figure 3.28 b), clearly showing that no heterostructure was formed, rather a mixture of ZnO NFs and CuO truncated cubes are present in the solution.

We also performed XPS analysis for detailed elemental characterisation of ZnO NFs + CuO truncated cubes material. Zn 2p and O 1s peaks corresponding to as deposited and post 200 °C annealed ZnO NFs + CuO truncated cubes are shown in Figure 3.29. No change is observed in Zn 2p (1021.8 eV) and O 1s peaks (O-Zn at 530.6 eV and -OH/O-C at 531.6 eV) before and after annealing in the ZnO NFs + CuO truncated cubes material indicating that annealing does not make chemical changes in the heterostructure. It was interesting to observe that ZnO NFs + CuO truncated cubes material showed no signature of Cu in XPS analysis, neither in as deposited nor in post annealed sample. However, since signature of presence of CuO was observed in absorbance spectra and XRD, we can only assume that XPS, being a surface technique, did not scan the bulk and that CuO was hidden in the bulk of the nanostructure thin film.

It is important to note here that the ZnO NFs + CuO truncated cubes material is not a heterostructure, but a mixture of two nanostructures, through characterisation techniques, it is not

referred to as a heterostructure through the text, but rather as a ZnO NFs + CuO truncated cubes material.

3.3 Conclusion

The nanostructures synthesised and characterised in this chapter were either fabricated to be an intermediate to another nanostructure or fabricated with the intended application of gas sensors. The single Zn-based and Cu-based nanostructures were synthesised and characterised to eventually integrate into heterostructures.

We discussed the effects of precursors on the formation of $Cu(OH)_2$ NWs. It is found that the concentration of the base, NaOH, plays a major role in formation of $Cu(OH)_2$ NWs. With the help of formation energy and energy above hull, we inferred that $Cu(OH)_2$ is a metastable material, which will change its morphology and composition on varying the reaction parameters. We also studied that botallackite nanoplatelets could be formed due to excess of Cl ions in the solution. The change of $Cu_2(OH)_3Cl$ nanoplatelets to crystals could be explained by space group transformations, Goldsmith's simplexity rule and Ostwald's step rule. Finally, we have been successful in stabilising and extracting the intermediate phase of botallackite in solution for at least 48 hours.

In the process of obtaining CuO nanostructures, intermediate nanostructures were obtained like $Cu(OH)_2$ NWs, $Cu_2(OH)_3Cl$ nanoplatelets, $Cu_2(OH)_3Cl$ crystals and Cu_2O truncated cubes. Each of these nanostructures, though individually unique, could not be translated into CuO nanostructures by temperature treatment and thus are not further discussed in the thesis. $Cu_2(OH)_3Cl$ nanoplatelets along with ZnO NRs formed the first heterostructure while annealed Cu_2O/CuO truncated cubes along with ZnO NFs lead us to the ZnO NFs + CuO truncated cubes material.

In this chapter, we also discussed the limitations in fabricating a heterostructure of ZnO and CuO via a sol-gel technique. two approaches were implemented to synthesise a heterostructure, one turned to be successful while the other not so clearly.

For the ZnO NRs + $Cu_2(OH)_3Cl$ nanoplatelets heterostructure, $Cu_2(OH)_3Cl$ nanoplatelets seem to align naturally onto ZnO NRs surface. However, our attempts to understand this natural alignment via crystal lattice parameters matching using the VESTA software did not give us the answers. However, characterisation techniques confirm the formation of the heterostructure. The ZnO NFs + CuO truncated cubes material was found to be a mixture of two nanostructure materials rather than a heterostructure.

The synthesis procedures used to fabricate the nanostructures were either modified versions of the one available in literature or original work. The novelties of the synthesis processes defined in this chapter thus

are summarised as follows:

Nanostructure (NS)	Synthesis Process	Characterisation Techniques				application in gas sensing
		Morphological (SEM, AFM)	Structural (XRD)	Optical (ABS)	Elemental (EDX, XPS)	
Single NS						
ZnO NRs	modified version of [19]	presented here, known in literature	presented here, known in literature	not presented here, known in literature	presented here, known in literature	yes, as a comparison to heterostructure
ZnO NFs	original synthesis procedure	presented here, known in literature	presented here, known in literature	not presented here, known in literature	presented here, known in literature	yes, as a comparison to heterostructure
$Cu(OH)_2$ NWs	adapted from [85]	presented here, known in literature	presented here, less known in literature	presented here, less known in literature	presented here, known in literature	no
$Cu_2(OH)_3Cl$ nanoplatelets	original synthesis procedure	original work	original work	original work	original work	no
$Cu_2(OH)_3Cl$ crystals	original synthesis procedure	original work	original work	original work	original work	no
CuO bundles	modified version of [85]	original work presented here, other versions known in literature	presented here, known in literature	presented here, known in literature	original work	yes
Cu_2O truncated cubes	modified version of [105]	presented here, known in literature	presented here, known in literature	presented here, known in literature	original work	yes/no tbd
Possible Heterostructures						
ZnO NRs + $Cu_2(OH)_3Cl$ nanoplatelets	original synthesis procedure	original work	original work	original work	original work	yes
ZnO NFs + CuO truncated cubes	original synthesis procedure	original work	original work	original work	original work	material not fully understood yet

Chapter 4

CuO bundles

CuO based nanostructures have been popularly used for gas sensing applications, either individually or in form of heterostructures [42, 41, 73, 52]. CuO is most used for H_2S gas detection, but it is a special mechanism as discussed in chapter 1, unlike for any other gas detection [39, 36]. In the following chapter however, we analyse the possibility of using CuO bundles in general gas sensing application.

First we analyse the IV characteristics of CuO bundles, as deposited and post deposition annealing treatment, in presence and absence of light, at different operating temperatures. This is to study the effect of post processing technique of annealing on the conduction through the CuO bundles network. We saw, in chapter 3, that CuO bundles showed absorption in visible wavelength. We study the IV characteristics of CuO bundles network in presence and absence of light to see if this visible light absorption translates to photoconductivity.

For metal oxide (MOx) chemiresistive gas sensors, oxygen adsorption and desorption reactions on a material's surface play a major role in the sensor kinetics. Studies on response and recovery curves of n-type MOx chemiresistive gas sensors have found that detailed analysis allow to extract parameters like time constants, reaction constants and diffusion coefficients. These derived parameters give more information on the processes occurring during gas sensing. However, such analysis is scarcely preformed for understanding p-type MOx sensors. Here, devices made from p -type CuO bundles network are investigated for oxygen adsorption - desorption properties as a gas sensor.

It was observed that the sensor has faster response and recovery in as deposited condition in comparison to annealed sensor. A detailed inspection of response and recovery curves enabled us to derive the above mentioned parameters for CuO bundles. Investigation of the derived parameters, role of network junctions and a hydroxylated CuO surface lead us to discuss the hypotheses for the

contributing processes.

We then study the performance of CuO bundles in presence of other reducing gasses like H_2 and CO. We observe that the response to 2% H_2 shows a non-monotonous behaviour with conductance transients while response to 20 ppm CO shows a response type inversion based on operating temperature. These phenomena were reported before only for n-type In_2O_3 [110, 111] and for WO_3 [112] when exposed to reducing gasses.

4.1 Preliminary remarks

The measurement and analysis presented below is performed on different samples with different device geometries. Unless specifically mentioned, the amplitude of current through the devices should not be compared directly. There are two reasons for this. First, since the devices are prepared by drop casting, there is a non-uniform distribution of nanostructures through the sample. Thus there could be more nanostructures interconnected in one device than the other, and it is impossible to determine which device has how many nanostructures forming a network between a pair of electrodes or how many junctions are formed in the network. Second, the graphs presented in one section may or may not be from one device. Since the nanostructure network distribution cannot be predicted comparing current in devices with different geometries will not be wise. However, if graphs are plotted together in one figure (mainly for the purpose of comparison), they may originate from one single device and thus can be directly compared in terms of current amplitude and characteristics.

In this chapter, all devices were annealed at a temperature of 200 °C for 2 hours in a furnace in air atmosphere, unless otherwise mentioned. CWL indicates 8 W cool white tube sourced from Hitachi which irradiates 1.25 mW power at 455 nm wavelength and 1.1 mW at 550 nm. LED indicates white LED powered by 1200 mA current is used and irradiates 118.3 mW at 440 nm and 95.8 mW at 550 nm.

4.2 Electrical transport

A potential sensor material is expected to have receptor as well as transducer abilities, i.e the ability for reversible adsorption-desorption of gas molecules and the ability to measure or convert this adsorption-desorption into electrical signal, respectively. The transducer functionality is usually tested with electrical transport properties of the potential sensor material. In the following section, we will test the electrical transport through CuO bundles network. We study the effect of annealing and effect of light irradiation on the conductance of CuO bundles network to find the optimum conditions for its application.

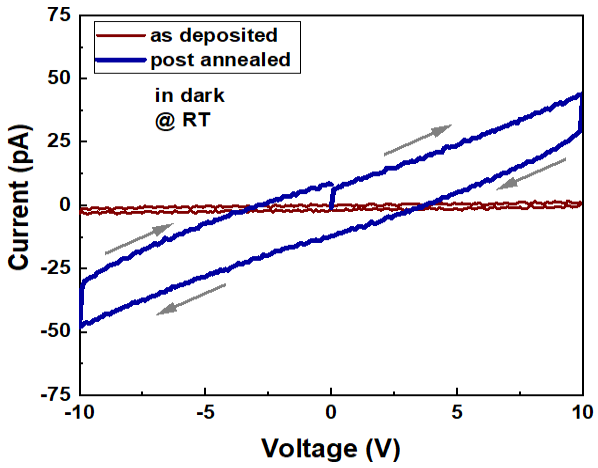

Figure 4.1: Current-Voltage characteristics (IV) of as deposited and post annealed CuO bundles deposited on interdigitated electrodes at room temperature (RT) in dark.

IV characteristics are measured and presented in Figure 4.1 and 4.2. The hysteresis observed in the IV trace is due to capacitive effects. From Figure 4.1, we can observe that annealing treatment increases the current passing through the CuO bundles device even when there were no observable structural changes in XRD spectrum. A popular reason for this increase in current is considered to be the removal of surface contamination or reinforcement of polycrystalline nature of CuO bundles [113]. This reason is however not consistent with the absence of change in the surface chemical composition observed by XPS (section 3.1.2), nor the weak change in peak width in XRD (section 3.1.2). Other reasons could be the removal of Schottky junctions at the contacts with the electrodes, which is usually formed on CuO due to its large work function [114], or of the junctions between CuO bundles, which can act as potential barriers for the current [115, 116, 69, 20].

Figure 4.2 shows the effect of light irradiation on IV characteristics of CuO bundles device for as deposited and post annealed. At RT, Figure 4.2 a), we observe that current through the device under light irradiation is higher than current through the device in dark. This indicates that CuO bundles show photoconductivity, effect where light irradiation generates charge carriers which participate in the conduction through the device. This observation is also backed up by the absorbance spectrum observed for CuO bundles (presented in section 3.1.2 Figure 3.12) where CuO bundles showed absorption in visible spectrum. Photoconductivity can originate from intrinsic (band-to-band) or extrinsic (defect-to-band) transitions in a semiconductor. When incident photon energies are greater than the band gap of the semiconductor, intrinsic band-to-band transitions dominate the absorption. This photon absorption creates an electron-hole pair which are now mobile charge carriers. These photon generated charge

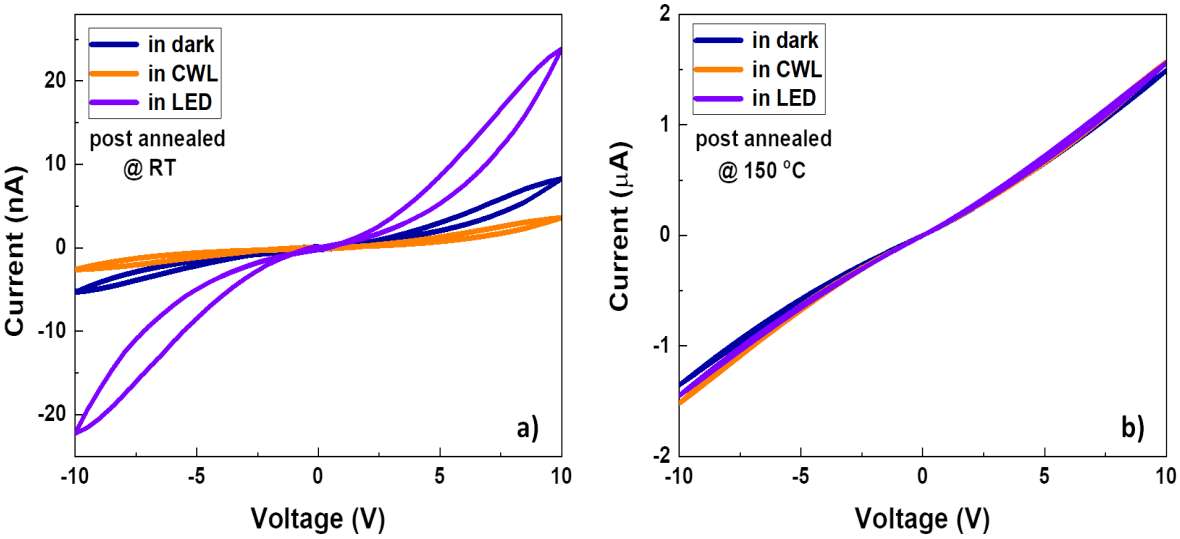

Figure 4.2: Current-Voltage characteristics (IV) of post annealed CuO bundles deposited on interdigitated electrodes a) at room temperature (RT), b) at 150 °C comparing effect of light irradiation.

carriers can thus affect the electrical properties of a semiconductor material [117]. With CuO, since the energy of light irradiated is equal to or greater than band gap, we assume band-to-band transitions lead to photoconductivity. In the particular device shown here at RT, current in presence of CWL is seen to be lower than that in dark. However, this trend was not repeated, and should be considered an anomaly.

At 150 °C, Figure 4.2 (b), an overall increase in current through the CuO bundles is seen which could be attributed to thermally generated charge carrier taking part in conduction. However, effect of photoconductivity on conductance is much weaker than what is observed at RT. A potential explanation for this observation is thermal excitation generates more charge carriers at 150 °C than photoconductive effect that take part in conductance. Hence, the current flowing through the device in dark and in both lighting conditions is almost the same at 150 °C operating temperature (Figure 4.2 (b)).

The main takeaway points from this section are as follows:

1. CuO bundles show ohmic electrical characteristics indicating that they can fulfil the transducer function of a sensor.

2. CuO bundles are photoconductive, but the effect is strongly visible at low operating temperature only.

4.3 Oxygen adsoprtion-desorption

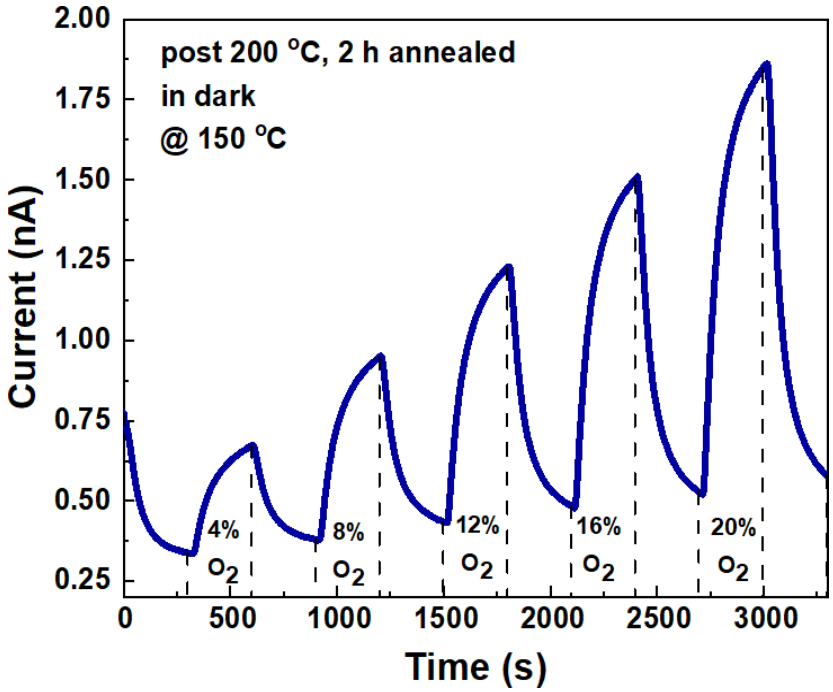

Figure 4.3: Demonstration of change in current through post annealed CuO bundles due to oxygen adsorption and desorption measured at 150 °C operating temperature in dark with a 10 V bias.

As mentioned before, oxygen adsorption and desorption plays an important role in determining gas sensing characteristics of a sensor. Thus we first study the response and recovery of the CuO bundles to oxygen with nitrogen as a carrier gas. Figure 4.3 demonstrates that upon exposure to different concentrations of oxygen at an operating temperature of 150 °C, post annealed CuO bundles show a change in current that corresponds to oxygen concentration, i.e, amplitude of current change increases for increasing oxygen concentration. Since the oxygen exposure was for a short period of time (300s), the CuO bundles sensor could not achieve a near steady state. Also, due to short period of nitrogen exposure after each oxygen exposure, the CuO bundles sensor did not get sufficient time for a full recovery of base current. This leads to a slight base line shift in the current observed in the Figure 4.3. This establishes that current passing through a network of CuO bundles is modulated by surface adsorption and desorption of oxygen, which is a requirement of qualification for a sensor material.

To closely study the effect of annealing on oxygen adsorption-desorption characteristics for CuO bundles, response to 20.9% O_2 in N_2 is measured and plotted for as deposited and post annealed CuO bundles at RT and at 150 °C in Figure 4.4 a) and b) respectively. Using equation 1.6 from section 1.1.1, SR for as

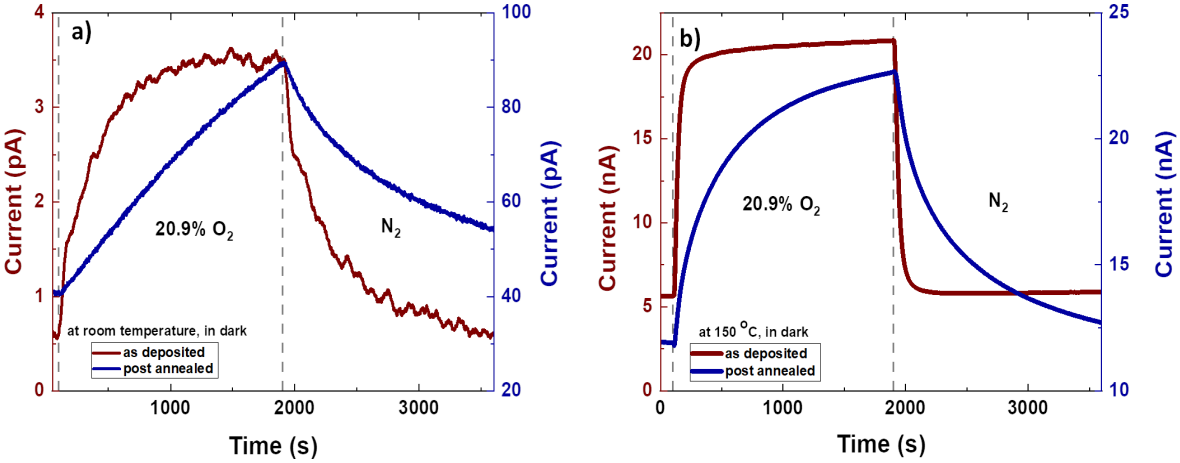

Figure 4.4: A comparative study of effect of annealing on sensor response and recovery of CuO bundles network, as deposited and post annealed, in dark to 20.9% O_2 a) at room temperature, b) at 150 °C operating temperature. The maroon line and left Y axis represent measurements corresponding to as deposited device while blue line and right Y axis indicate measurements on post annealed sample.

deposited CuO bundles to 20.9% O_2 is calculated to be 6.08 at RT and 3.69 at 150 °C, while for post annealed CuO bundles is calculated to be 2.17 at RT and 1.8 at 150 °C. We observed that even though annealing increases the current flowing through the device, it does not improve the SR. Also, operating at higher temperatures, is seen to reduce SR for CuO bundles for this particular device. We also observe that even though SR is not improved, operation at higher temperature, 150°C, improves the response and recovery time of the CuO bundles as deposited CuO bundles have an approximate response time of 725 s and recovery time of 1500 s at RT while only 200 s and 140 s at 150 °C, respectively. For post annealed device, the current does not reach a steady state value in the exposure time at RT, but at operating temperature of 150 °C, the response time is 745 s while the recovery time is 1400 s. The decrease in the response time can be understood by the thermal activation of the sensing mechanism, as will be explained in more detail below. More surprisingly, the as-deposited CuO bundles network shows faster response than the annealed one at all operating temperatures.

It is to be noted that the error bar for calculated response and recovery times is between 0.5% to 3%.

Figure 4.5 analyses effect of light on response of CuO bundles to oxygen adsorption and desorption. At RT, this device failed to show change in current on 20.9% O_2 exposure, but overall current flowing through CuO bundles increases on visible light exposure due to photoconductivity. At an operating temperature of 150 °C, however, CWL light is seen to negatively influence SR, while LED is seen to positively influence SR in presence of 20.9% O_2. This trend was not uniform through multiple devices when tested, and thus

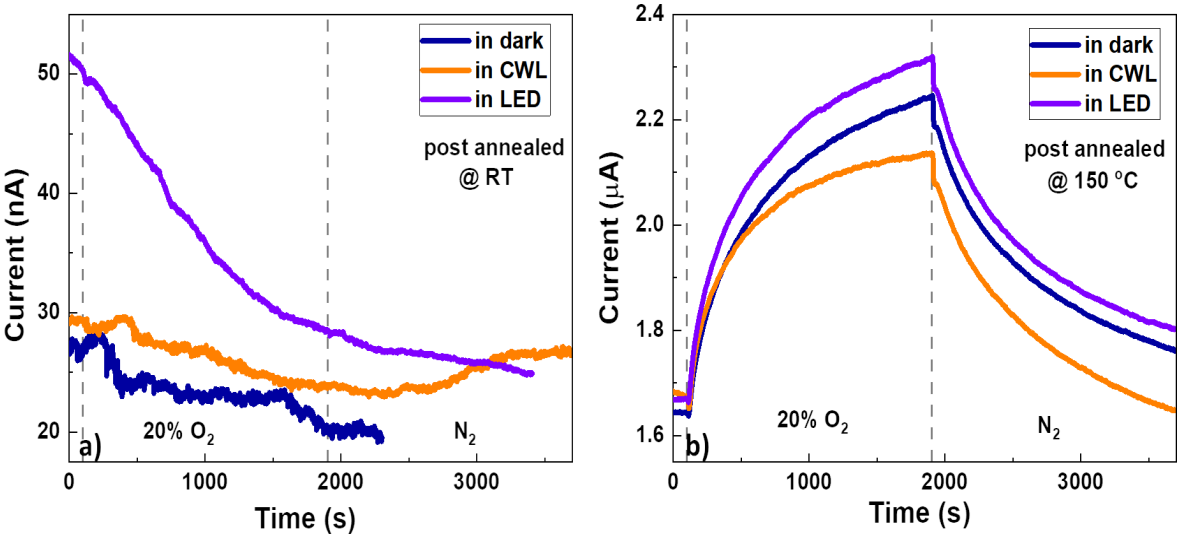

Figure 4.5: A comparative study of effect of light irradiation on sensor response and recovery of post annealed CuO bundles network to 20.9% O_2 a) at room temperature, b) at 150 °C operating temperature. For this particular device, no sensing at room temperature was observed.

cannot be generalised.

To quantitatively analyse the response and recovery of CuO bundles network to oxygen exposure, the curves were separately fitted with exponential functions. For each curve, we first attempted to fit the response and recovery with a single exponential function, mainly using, for the response:

$$I_{resp} = I_0 \left\{ 1 + A_{resp} \left[1 - \exp\left(\frac{-t}{\tau_{resp}} \right) \right] \right\} \tag{4.1}$$

and, for the recovery:

$$I_{reco} = I_0 \left\{ 1 + A_{reco} \exp\left(\frac{-t}{\tau_{reco}} \right) \right\} \tag{4.2}$$

where I_0 is the steady-state current under nitrogen flow. However, for some conditions, this attempt to fit the curve with a single exponential failed (see Figure 4.6 a) and b)). For this reason, for these specific conditions, we performed fits with suitable functions containing two exponential terms. For the response curve, we use:

$$I_{resp} = I_0 \left\{ 1 + A_{1resp} \left[1 - \exp\left(\frac{-t}{\tau_{1resp}} \right) \right] + A_{2resp} \left[1 - \exp\left(\frac{-t}{\tau_{2resp}} \right) \right] \right\} \tag{4.3}$$

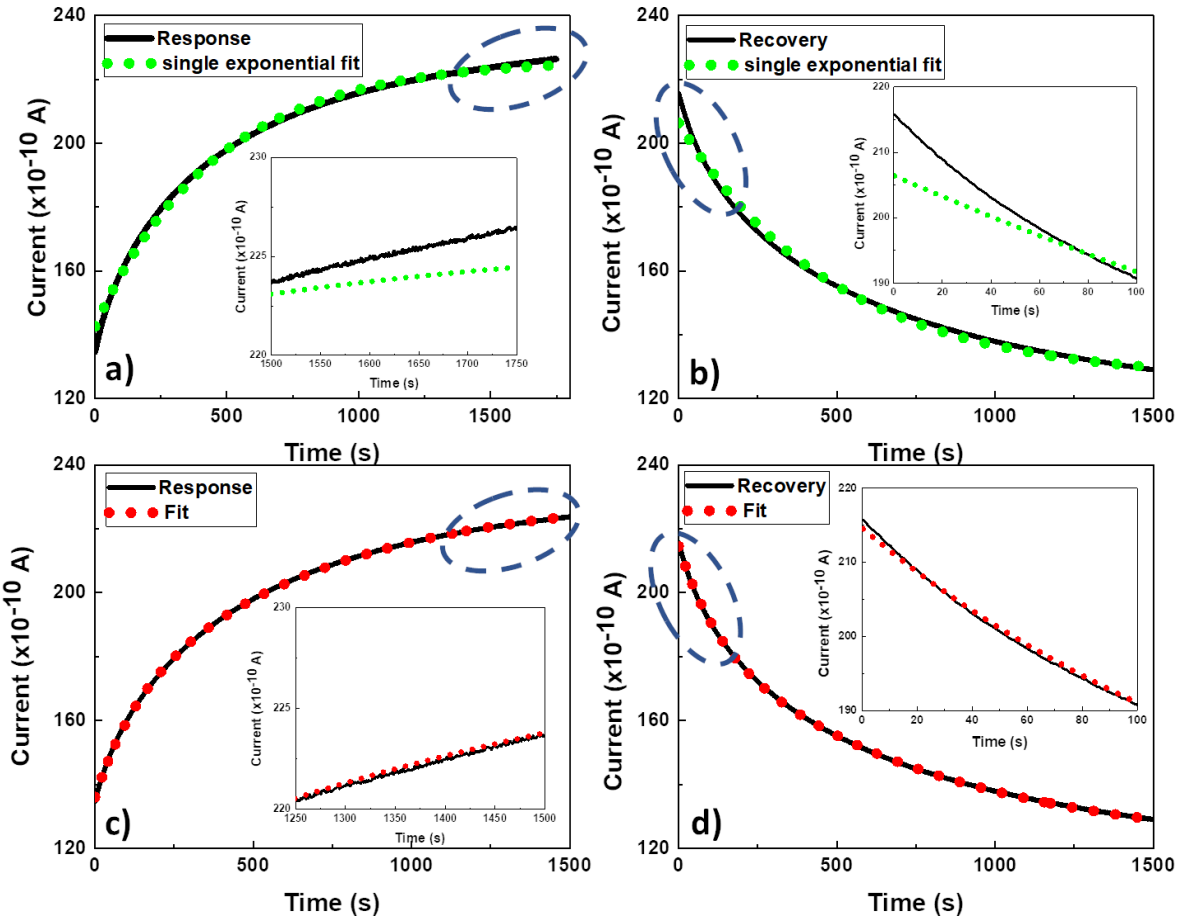

Figure 4.6: Example of curve fitting of a) and c) response curve, b) and d) recovery curve of post annealed CuO bundles network to 20.9% O_2 in N_2 in dark at 150 °C operating temperature using equation for a), equation for b), equation for c) and equation for d). The insets show zoomed in regions of respective original curves for regions marked with dashed outline.

while for the recovery curve, we use:

$$I_{reco} = I_0 \left\{ 1 + A_{1reco} \exp\left(\frac{-t}{\tau_{1reco}}\right) + A_{2reco} \exp\left(\frac{-t}{\tau_{2reco}}\right) \right\} \tag{4.4}$$

The strong improvement of the fitting with two exponential terms, as seen in Figure 4.6 c) and d), is an indication that there are two different processes occurring in the CuO bundles device on exposure to O_2, corresponding to the two exponential terms, as will be discussed later. An example of the fit with two exponential terms is shown in Figure 4.6 c) and d) for post annealed CuO bundles device responding to 20.9% O_2 at 150 °C in dark. The device was exposed to N_2 prior to exposure of 20.9 %

Sample	Operating Temperature °C	Response					Recovery				
		A_{1resp} -	τ_{1resp} s	A_{2resp} -	τ_{2resp} s	t_{90} s	A_{1reco} -	τ_{1reco} s	A_{2reco} -	τ_{2reco} s	t_{10} s
as deposited	25 (RT)	2.18	306	-	-	704	4.78	419	-	-	964
	50	4.6	1757	1.43	131	3850	2.14	703	2.14	143	1130
	100	1.36	428	7.1	99	340	1.05	298	3.16	80	316
	150	3	35	-	-	80	6.33	39	-	-	90
post annealed	25 (RT)	2.72	2866	-	-	6592	0.96	1682	0.29	257	3430
	50	0.46	1437	-	-	3305	0.45	2406	0.07	300	5190
	100	0.11	596	-	-	1370	0.24	1203	-	-	2760
	115	0.35	973	-	-	2238	0.29	1359	0.05	128	2900
	135	0.58	956	0.1	124	2050	0.5	1025	0.13	130	2120
	150	0.52	641	0.18	123	1290	0.57	762	0.22	120	970

Table 4.1: Time constants for fits on response and recovery curves of as deposited and post annealed CuO bundles to 20.9% O_2 at various operating temperatures in dark

Sample	Operating Temperature °C	Response					Recovery				
		A_{1resp} -	τ_{1resp} s	A_{2resp} -	τ_{2resp} s	t_{90} s	A_{1reco} -	τ_{1reco} s	A_{2reco} -	τ_{2reco} s	t_{10} s
as deposited	25 (RT)	1.82	395	-	-	909	4.86	587	-	-	1350
	50	1.5	637	-	-	1465	1.36	474	-	-	1090
	100	1.3	484	0.47	125	970	0.77	630	0.62	131	1075
	150	1.1	475	4.44	37	330	3.68	46	-	-	106
post annealed	25 (RT)	0.37	2567	-	-	5904	0.17	1892	-	-	4352
	50	0.21	923	-	-	2123	0.54	2793	0.07	288	6090
	100	0.17	730	-	-	1679	0.25	1061	-	-	2440
	115	0.25	822	-	-	1891	0.37	1387	0.07	137	2940
	135	0.59	961	0.12	132	2040	0.5	974	0.13	126	2020
	150	0.58	710	0.19	126	1450	0.58	770	0.23	119	1520

Table 4.2: Time constants for fits on response and recovery curves of as deposited and post annealed CuO bundles to 20.9% O_2 at various operating temperatures in CWL

O_2. From these fits, we extract the values for the time constants τ_i ($i = 1resp$, $2resp$, $1reco$, $2reco$) and the relative magnitudes A_i, which are reported in Table 4.1 and 4.2 for CuO bundles exposed to 20.9% O_2 at various operating temperatures.

The quantitative analysis first confirms that the t_{90} response and t_{10} recovery times of as-deposited samples are 2 to 16 times smaller than for annealed samples, with an exception case of t_{90} 50 °C in dark. It clearly indicates that annealing changes the dominating sensing mechanisms in these devices, although no major change has been observed in the crystal structure in XRD and only a week change is observed in the surface states in XPS analysis. One hypothesis could be the role of junctions between the CuO bundles in the network, as was already emphasized in metal oxide nanowire networks for explaining the increase of sensitivity in as deposited samples [115, 116, 69, 20]. We speculate that the sensitivity is dominated by the junctions, which act as grain boundaries, for as-deposited samples,

while annealing removes the potential barriers at the junctions, which also explains the large increase of the device conductance observed after annealing.

Based on values tabulated in table 4.1 and 4.2, we make two major observations. First, there is no common trend based on variation in temperature for having one or two time constants. This might mean that the process contributing to the time constants are not directly temperature activated or are not temperature dependent. Since there is a mixture of one and two time constants, we cannot plot an Arrhenius plot to confirm the temperature dependency or in-dependency of these processes. Second, the effect of light on oxygen adsorption-desorption is not clear as in IV. Based on the values of t_{90} response and t_{10} recovery times obtained in table 4.1 and 4.2, we see no clear difference. It might not be interesting to further investigate the effect of light on CuO bundles exposed to other gasses.

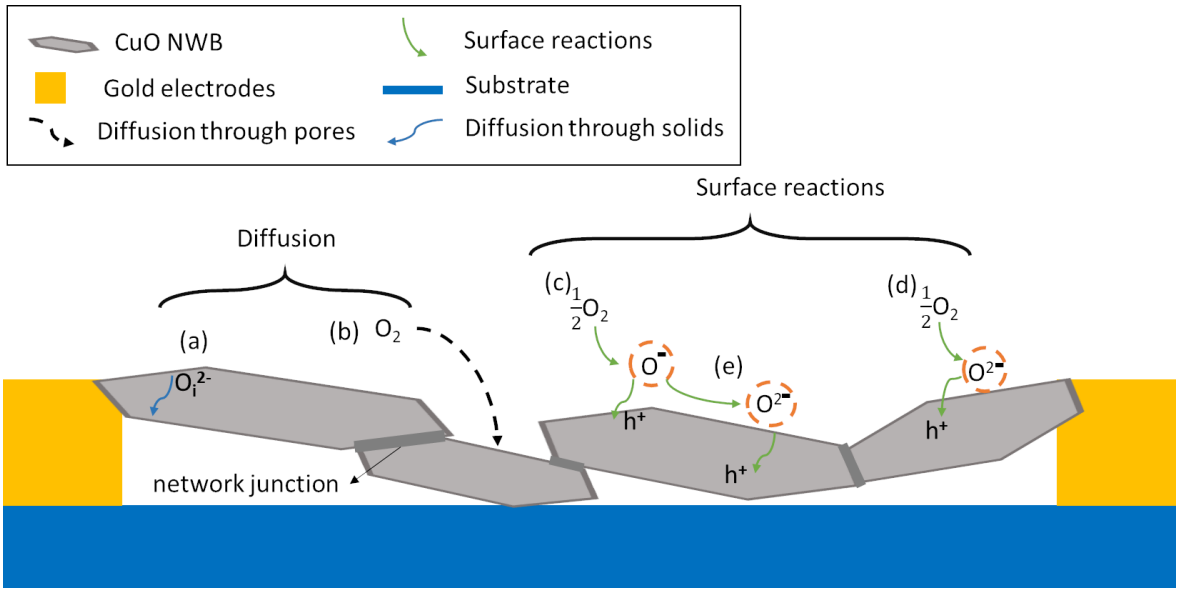

Figure 4.7: Schematic representing possible different mechanisms contributing to response and recovery in CuO bundles network sensor.

In order to better explain the response and recovery of CuO bundles network, and in particular the observed time constants and the faster response for as-deposited devices, we discuss here the envisioned mechanisms driving this response and recovery. In the current understanding of the sensing mechanisms of MOx nanostructures, the response occurs through two processes, (1) the diffusion of the gas towards the transducer and (2) the reaction occurring between the oxygen molecules in the gas phase and the atoms on the surface of the MOx material [118, 27, 119]. Following this knowledge, we make the hypothesis that the observation of two time constants in the response or recovery of CuO

bundles network to oxygen can be attributed to the following:

- both, diffusion taking place through the material and surface reaction or adsorption-desorption of oxygen species having different kinetics,
- different diffusion mechanisms occurring in the sensor,
- different oxygen species that are adsorbed on the surface of the sensor having different adsorption kinetics.

The mechanisms are schematically presented in Figure 4.7. The figure shows how CuO bundles form electrical network between the electrodes. Junctions between the CuO bundles are a part of this network and will also adsorb oxygen species. The possible reactions are displayed in the schematic and largely divided into two, diffusion and surface reactions. Figure 4.7 (a) represents diffusion of oxygen defects, mainly oxygen interstitials, O_i^{2-} for CuO, into the bulk material or diffusion in bulk, while Figure 4.7 (b) represents diffusion of oxygen species through pores of the network. Figure 4.7 (c), (d) and (e) represent the possible oxygen species that are adsorbed which will be discussed below in detail. In the following, we will discuss the relevance of each of these mechanisms as compared to the observations made in CuO bundles.

For nanostructured films, the diffusion can either occur in the pores of the nanostructures, or in the solid material itself. The diffusion through the pores depends on the pore size. When the pore size is below 2 nm, also known as micropores, surface diffusion dominates. When pore size is between 2 nm to 50 nm, pores are known as mesopores and free-particle (Knudsen) diffusion takes place in such sensors. This is the most popular diffusion studied in thin film MOx sensors in literature. If pore size is more than 50 nm, the pores are known as macropores and it is assumed that molecular diffusion takes place in such sensors. Quite often, the pore size is not uniform in sensor films and two of these diffusion mechanisms could occur simultaneously. Molecular diffusion is usually rapid so that the target gas can reach secondary particles very easily [27]. At last, diffusion of oxygen defects into the solid sensing material has also been evoked as the origin of the finite response time of gas sensing materials [111].

Let us consider that the two time constants observed for for as-deposited CuO bundles at 100 °C, and for post-annealed ones at RT and 150 °C, correspond to two different diffusion mechanisms. CuO bundles studied in this work are deposited by drop casting on a set of interdigitated gold electrodes. They form a network between these electrodes which allows for conduction. As stated earlier, the CuO bundles are roughly 500 nm - 1 μm in width and 2 - 4 μm in length. Judging from multiple SEM images, the pore size between CuO bundles film formed will also be in the μm range. Thus,

we can assume than we primarily have macropores in CuO bundles network and molecular diffusion could be taking place when gasses interact with the sensor material. However, CuO bundles formed are essentially an agglomeration of $Cu(OH)_2$ nanowires due to heating while the $Cu(OH)_2$ nanowires are formed by nanocrystals with average size of 160 nm, aligning together. The pores in between the nanocrystals could be smaller than the nanocrystals themselves. In that case, on a secondary level, there could be presence of mesopores and macropores in the CuO bundles which could lead to Knudsen diffusion and molecular diffusion, or a limit between both [120, 121, 122, 123, 119].

These mechanisms can be distinguished by the magnitude of their respective diffusion coefficients. Diffusion coefficients of the processes mentioned above can be evaluated to $0.2 - 0.4$ cm^2s^{-1} for the molecular diffusion of O_2 in N_2 and at a temperature between 20 and 150 °C [124], few 10^{-5} cm^2s^{-1} for Knudsen diffusion [125], 10^{-4} to 10^{-6} cm^2s^{-1} for surface diffusion [126], and 10^{-17} to 10^{-13} cm^2s^{-1} for the bulk diffusion of oxygen defects in metal oxide materials in a temperature range between 20 and 150 °C [127]. Assuming 1 D diffusion through a plane sheet, the diffusion coefficient can be related to a typical diffusion time by the following formula [128],

$$D = \frac{L^2}{\tau(\pi)^2} \tag{4.5}$$

where D is the diffusion coefficient, L is the thickness of the plane sheet, or thin film in our case, and τ is the corresponding time constant. Using the values of τ derived from curve fitting for response curve observed for 20.9% of oxygen exposure at 150 °C in dark and assuming L to be of the order of $200 - 500$ nm, corresponding to the crystallite size and to the width of the CuO bundles, we obtain $D_1 = 0.1 - 0.7 \times 10^{-11}$ cm^2s^{-1} for as-deposited devices, $D_1 = 0.6 - 4 \times 10^{-13}$ cm^2s^{-1} and $D_2 = 0.3 - 2 \times 10^{-12}$ cm^2s^{-1} for annealed devices. These values indicate that the observed τ would most probably correspond to diffusion of oxygen defects through the solid, i.e through the sensor material.

The faster response of the as deposited device as compared to the annealed one can then be understood within the diffusion model. Assuming that the response of as-deposited samples is dominated by the junctions, diffusion at the junction is expected to be faster than in the bulk due to the smaller length to be covered and larger amount of defects at the junctions. However, the values derived for diffusion constant for CuO bundles make it clear that, for the operating conditions when two time constants are observed, only one time constant can be attributed to diffusion through solids, while the other time constant will correspond to another process.

Considering the oxygen adsorption/desorption mechanism, it is well known in the literature that,

at different temperatures, different oxygen species absorb on the surface of MOx. Using temperature programmed desorption on SnO_2, Yamazoe et al. have shown that oxygen adsorbs as $O_{2,ads}$ at low temperature, then $O^-_{2,ads}$ is dominating at 150 °C, and then O^-_{ads} or O^{2-}_{ads} are dominating at 400 °C [129]. The temperature ranges are strongly dependent on the material, and, indeed, it has been demonstrated for p-type NiO that the following reaction occurs at all temperature ranges [130]:

$$O_2 + 2\,e^- \rightleftharpoons 2\,O^-_{ads} \tag{4.6}$$

and is found to be irreversible at RT for p-type NiO. At temperature higher than RT, the following reaction occurs [130]:

$$\frac{1}{2}\,O_2 + 2\,e^- \rightleftharpoons O^{2-}_{ads} \tag{4.7}$$

Bielañski and Najbar found that this reaction occurred at 150 °C to 235 °C for NiO films. These species also undergo inter-conversion, for example in the following equation [130]:

$$O^-_{ads} + e^- \rightleftharpoons O^{2-}_{ads} \tag{4.8}$$

The conversion of O^- to O^{2-} based on equation 4.8 is a temperature dependent reaction, very slow at RT, and is found to be faster at higher temperatures. This was proven with an example of adsorption measurements on NiO surface. At 150 °C, after 120 min of oxygen exposure, 44% of O^- that was absorbed was seen to convert to O^{2-}, while at 235 °C, there was 21.7% O^{2-} after only 8 min [130].

The reaction occurring between the gas molecules and the sensor material is reversible, where the forward reaction (response) is assumed to be second order, while the reverse reaction (recovery) is first order [119, 27, 131]. In the case of the response to oxygen, for a given material, at a given temperature and oxygen partial pressure, it is possible to relate the response and recovery times to effective rate constants [132], $k_{eff,ads} = 1/\tau_{resp}$ and $k_{eff,des} = 1/\tau_{reco}$.

Let us consider that the time constants are related to different oxygen species adsorbed on the surface of CuO bundles. Considering that CuO, a p-type MOx, behaves similar to NiO, at 150 °C there can be presence of O^-_{ads} and O^{2-}_{ads}, with increasing concentration of O^{2-}_{ads} and decreasing concentration of O^-_{ads} when increasing the temperature. Based on the work of Bielaski et al. , there could also be conversion of one species to another at high temperature operation of the sensors which affects the reaction speeds, and thus, the values of the time constants [130]..

Korotcenkov et al. worked on In_2O_3 sensors for ozone detection and found that fitting of the response and recovery curves translated to five distinct time constants corresponding to five different

processes, namely, dissociative adsorption / desorption of oxygen, dissociative adsorption / desorption of water and intercrystallite oxygen diffusion [111]. At an operating temperature of 150 °C, they observed time constant of the order of 10 s for response and 100 s for recovery of ultra thin In_2O_3 films exposed to 1 ppm of Ozone in dry and wet atmospheres. Makeeva et al. have determined the rate constants of oxygen adsorption on thick nanocrystralline SnO_2 films [132]. They obtain values of time constants from 1600 s to 85 s in the temperature range from 225 to 400 °C.

The values we obtain, from 35 s to 6592 s in the temperature range of RT to 150°C, for all response and recovery time constants are thus comparable to experimental data obtained for MOx gas sensors, and we could then easily consider that the observed response and/or recovery are limited by surface reactions with different oxygen species. To understand the faster response and recovery of the as-deposited device as compared to annealed one, we note that the change in the surface, mainly close to the junctions, can explain the change in speed, and that it is also compatible with the weak change observed in XPS.

Here, it is also important that we discuss about influence of -OH groups on sensing. XPS analysis presented in Figure 3.11 explicitly shows presence of Cu bonded to -OH groups on the surface of CuO bundles, even after annealing. The role of -OH groups is not very well studied in metal oxide gas sensors. However, Michel et al. observed -OH groups on SnO_2 surface even after high vacuum high temperature annealing. They could not comment on the role of -OH groups in sensing due to lack of availability of a sensing surface that does not have -OH groups, but commented that the presence of -OH groups causes signal drifts seen in chemiresistive sensors[133]. Golovanov et al. observed different degrees of -OH groups on different facets of SnO_2 and explained a mechanism where -OH groups affect gas sensing properties if the oxygen in -OH group is lattice-bound [134]. However, based on experiments performed here and literature alone, it is difficult to separate the role of -OH groups in gas sensing of CuO bundles.

4.4 Gas sensing

It is essential to analyse response of CuO bundles to other gasses, eg. reducing gasses. Further subsections present performance of CuO bundles in presence of reducing gasses H_2 and CO and its analysis. All the measurements presented hereafter, are done on a post annealed CuO bundles device, unless otherwise mentioned.

4.4.1 Hydrogen (H_2):

H_2 is a standard reducing gas, which when in contact with a p-type MOx, removes adsorbed oxygen from the surface, causing an expected reduction in the overall current flowing through the device as shown earlier in Figure 1.3 in chapter on fundamentals. A response and recovery curve obtained from post annealed CuO bundles exposed to 2% H_2 in N_2 at at various operating temperatures in dark and in LED is shown in Figure 4.8 a) and c), respectively. Observing the CuO bundles at RT in Figure 4.8 a) and c), we see that CuO bundles show a series of transient current variation before showing the expected reducing response. A focus on first 400 minutes of H_2 exposure can be observed more clearly in Figure 4.8 b) and d). Here we choose to work with LED light instead of CWL due to the difference in its incident power density.

At RT, CuO bundles do not respond to presence of 2% H_2 in dark and the current is seen drift to a lower value over time. However, in LED light, CuO bundles show a slight reduction of current on introduction of 2% H_2 in the long term response, followed by a slight increase in current for the rest of the exposure time. As similar trend is also seen in response curves for an operating temperature of 100 °C in dark and 100 °C, 125 °C in LED. This trend of drifting current changes when operating temperature is increased to 125 °C in dark and 150 °C in LED light and beyond.

The CuO bundles sensors is seen to show a response reaching steady state within 1000 s for operating temperature of 200 °C in dark and 600s for operating temperature of 200 °C in LED light. There are two things that can be noted here, effect of operating temperature and effect of light irradiation on SR of CuO bundles to 2% H_2. Higher operating temperature ensures an expected response, where 200 °C seems to be the optimum working temperature, considering the criteria for optimum is fast p-type response and recovery. Light irradiation seems to qualitatively change how CuO bundles respond to presence of 2% H_2 at various temperature. Based on the slope of the recovery curve, recovery of CuO bundles is seen to be faster and complete when it is operated at temperatures above 175 °C, both in dark and in LED light, whereas intermediate temperatures have slower recovery.

Let us take a closer look at the current transients appearing in the first 200s of 2% H_2 exposure. The common trend for each of the operating temperature, except RT where no response is observed, both dark and in LED light, is as follows: the current through the device drops first, then rises to a peak and then continues dropping to give the as expected long term sensor response to 2% H_2. When operating temperature is increased beyond 100 °C, this trend tends to shift upwards in terms of amplitude of current, reaches a maximum and then starts to drop again. In dark the maximum current peak is seen at 175 °C, while in LED light it is seen at 125 °C. This maximum also affects the response time of the sensor. For temperatures when the maximum is higher than others, the long term response attains saturation slower,

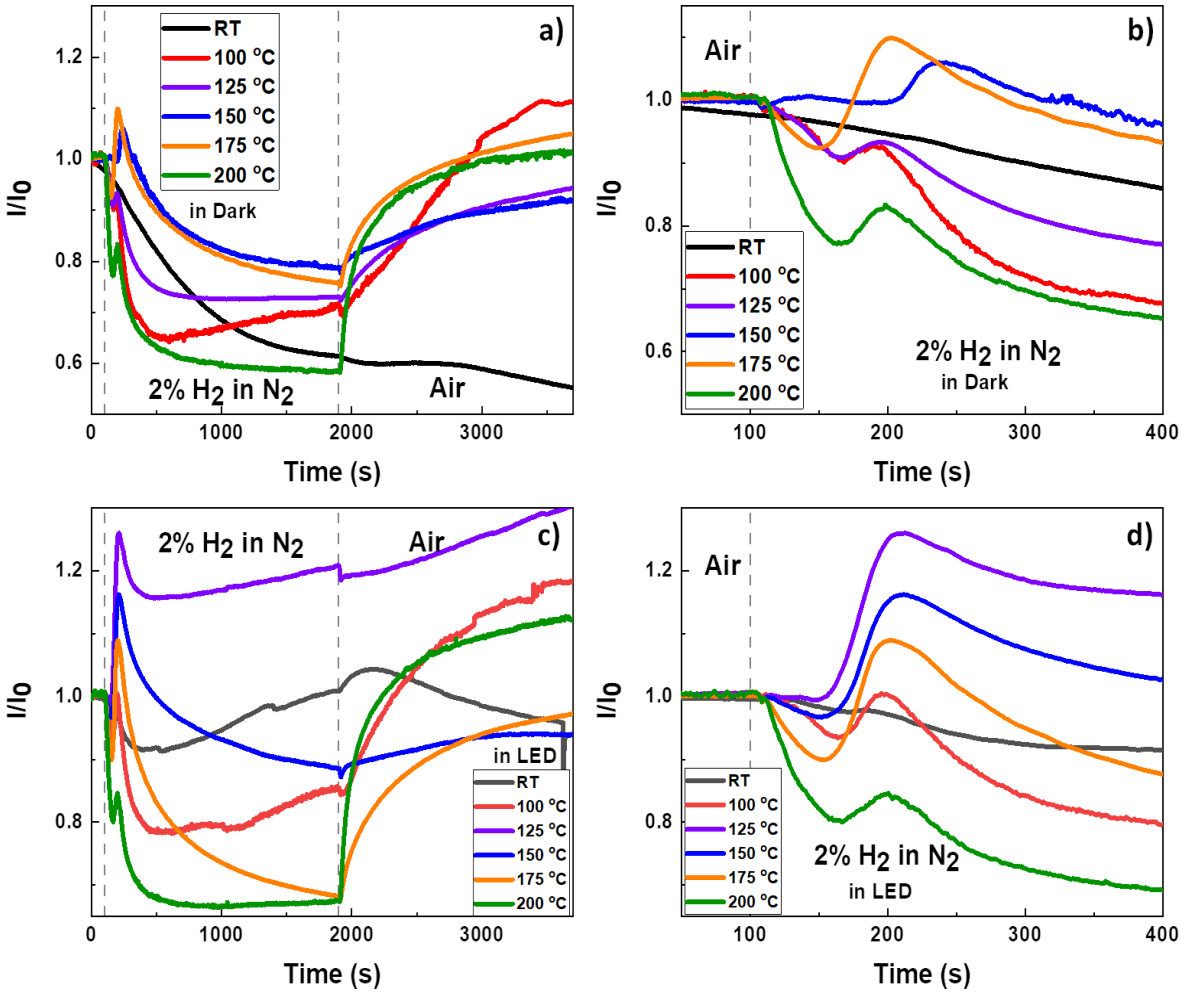

Figure 4.8: Response and recovery of post annealed CuO bundles exposed to 2% H_2 in N_2 at various operating temperatures a) in dark and c) in LED. CuO bundles were exposed to synthetic air before and after H_2 exposure. b) and d) show a closer look at first 400 s of response for the same working and atmospheric conditions, highlighting the nature of the transients.

indicating that the transient affects the time scale of response.

Korotcenkov *et al.* worked with In_2O_3 sensor sensing 0.1% of H_2, 1000 ppm of CO and 1 ppm of Ozone, where they observed conductivity transients in first few seconds of gas exposure at 280 °C. 280 °C was close to the transition temperature when the sensor response transitioned from p-type to n-type [110]. In another work, Korotcenkov *et al.* worked with In_2O_3 sensor sensing Ozone only, where they calculated five time constants corresponding to the transients observed in conductivity and attributed them to different process occurring on the surface of the sensors [111]. Based on the our knowledge of the literature, such transient observations or related analysis has not been done before on p-type MOx sensing reducing gasses.

H_2, when in atmosphere near CuO surface will react with either of the adsorbed oxygen species through following reactions. These are described for CO sensing on In_2O_3 surface by Korotcenkov *et al.* [110]:

$$H_2 + O_S^- \longrightarrow H_2O \uparrow + e^- \tag{4.9}$$

$$2H_2 + O_I^{2-} \longrightarrow 2H_2O \uparrow + 2e^- \tag{4.10}$$

$$2H_2 + (O_2)_{ads} + e^- \longrightarrow 2H_2O \uparrow + 2O_S^- \tag{4.11}$$

The excess electron given back to CuO as a product of the reaction, will reduce its conductivity as we see in the long term response curves observed. Here O_S^- is chemisorbed oxygen species, while O_I^{2-} is a lattice oxygen that interacts with the gas.

Korotcenkov *et al.* believed that the transient in conductivity occurred due to possible rapid oxygen incorporation into In_2O_3 lattice, causing a complicated shape. They stated that the reactions mentioned in 4.9, 4.10 and 4.11 are competing mechanisms at the start of sensing. After certain time of competition, they attain an equilibrium where only one reaction dominates the effect on conductivity [110, 111]. If we follow through with the same analogy, 4.10 and 4.9 are electron donating or will cause reduction in current through CuO bundles, while 4.11 is electron accepting or will cause increase in current through CuO bundles. It is also known, that for MOx, energy barrier for reaction with chemisorbed oxygen species will be lesser that the energy barrier for reaction with lattice oxygen [110]. Thus, in the case of CuO bundles reacting to presence of 2% H_2, the sequence of reactions constituting the transient in conduction will be as follow: 4.9 causing the first reduction in current, followed by 4.11 causing an increase in current and finally 4.10 dominating and constituting the main part of long term response.

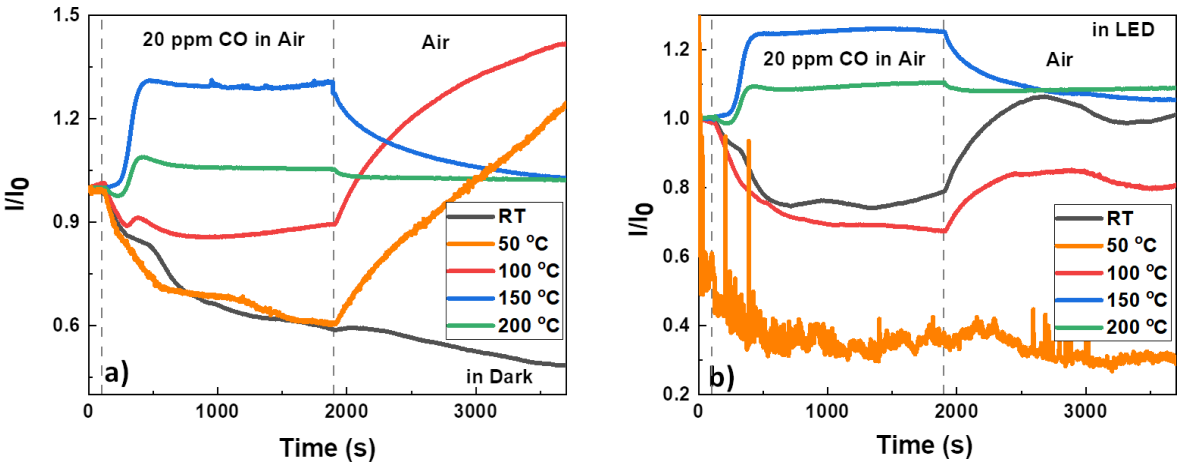

Figure 4.9: Response and recovery of post annealed CuO bundles exposed to 20 ppm of CO in air at various operating temperatures a) in dark and b) in LED light.

4.4.2 Carbon Monoxide (CO):

CO is a hazardous reducing gas with long term exposure limit of 20 ppm. Hence, we tested performance of CuO bundles sensors in 20 ppm of CO in air, in dark and in LED light at various temperatures. The observed curves are plotted in Figure 4.9 a) and b), respectively.

The response observed for CO is much different than that observed for H_2, even though both are reducing gasses. CuO bundles change the response to CO from decreasing current to increasing current on increasing the operating temperature equal to or above 150 °C, both in dark and in LED light.

This change of nature of response was first reported by Korotcenkov *et al.* for In_2O_3 based sensor. They identified the change of nature of response based on operating temperature in In_2O_3 sensors responding to reducing H_2 and CO. In_2O_3, an n-type MOx, displayed response with decreasing current to 0.1% of H_2 up to operating temperatures of 210 °C. For operating temperatures beyond 210 °C, In_2O_3 sensor displayed response with increasing current to as expected 0.1% of H_2 [110]. Similar temperature dependent change in response type is also reported for n-type WO_3 by Maity *et al.* [112]. However, such a change of nature of response is reported only for a few n-type MOx mentioned above.

CO, when in atmosphere near CuO surface will react with either of the adsorbed oxygen species through following reactions, similar to H_2. The following equations are adapted directly from Korotcenkov *et al.* [110]:

$$CO + O_S^- \longrightarrow CO_2 \uparrow + e^- \tag{4.12}$$

$$CO + O_I^{2-} \longrightarrow CO_2 \uparrow + 2e^- \tag{4.13}$$

$$\mathrm{CO} + (\mathrm{O_2})_{\mathrm{ads}} + \mathrm{e}^- \xrightarrow{\mathrm{H_2O}} \mathrm{CO_2} \uparrow + \mathrm{O_S}^- \tag{4.14}$$

The excess electron given back to CuO as a product of the reaction, is expected to reduce its conductivity.

Using the same analogy used for understanding H_2 response, let us try to understand the sequence of the competing reactions that give us the response observed. For operating temperatures lower than 150 °C, CuO bundles give response by decreasing current for reducing CO gas. So at these lower operating temperature the sequence of reactions dominating could be as follows: first, 4.12 causes a slight reduction in current followed by 4.14 for a very short time causing a small increase in current, finally 4.13 which leads to the long term response. This is similar to the sensing mechanism discussed for H_2. However, for operating temperatures greater than equal to 150 °C, CuO bundles give response with increasing current for reducing CO gas. So at these higher operating temperatures, the sequence of reactions dominating could be as follows: first, 4.12 causes a very slight reduction in current followed by 4.14 causing an increase in current, finally 4.14 and 4.13 seem to attain an equilibrium where current does not vary in the long term.

For even higher operating temperature 200 °C, the increasing current SR is seen to reduce as compared to that of 150 °C in terms of steady state amplitude. The reason for this could be that contribution from 4.14 is lower at 200 °C than at 150 °C. It is common in MOx sensors to have optimum operating temperature where highest SR is achieved [76]. It is found that, in general, with a given reducing gas CO here, there is a peak in the sensitivity if the operating temperature is too low, the reaction of 4.14 is too slow to give a high sensitivity. On the other hand if the operating temperature is too high, the overall oxidation reaction proceeds so rapidly that the concentration of reducing gas CO at the surface of MOx becomes diffusion limited. Morrison stated an example saying CO and H_2 can be burned at a very low temperature, even at RT, and if the sensor operating temperature is raised too high above RT, the gases burn too rapidly and are not detected [81]. Since the response of the sensor inverts on the basis of the operating temperature, it is difficult to quantitative compare the SR and find an optimum working temperature. On a positive note, such inversion which depends on gas type can be an advantage for temperature based selective sensor application.

Recovery of CuO bundles in air confirms the nature of response obtained in presence of CO. However, we observe that drifts dominate the recovery of the sensor in dark as well as in LED light. It must be noted that the curves at 50 °C in LED should not be considered as clearly, there is a contact issue which causes the noisy current shown here.

4.5 Conclusion

In this chapter, we analysed the CuO bundles network as a potential material to be used for gas sensing applications. To determine this, we analysed electrical transport, oxygen adsorption-desorption and performance of CuO bundles in presence of reducing gasses. The following points enlist new findings in each of these aspects.

1. IV characteristics of CuO bundles showed that annealing improved the overall current through the device, either due to removal of contamination or Schottky barriers or improvement in grain boundaries at junctions between nanostructures. Photo conductivity was observed at lower operating temperatures, while at higher temperatures it was either not present or weak compared to effect of excess charge carriers due to high operating temperature. This established that CuO bundles can carryout the transducer function of a gas sensor.

2. CuO bundles network displayed reversible oxygen adsorption desorption at all operating temperatures as well as in as deposited and post annealed conditions. As deposited CuO bundles showed faster response and recovery kinetics than post annealed one, which was attributed to role of junctions formed in the sensor network. Detailed time constant and diffusion constant analysis helped us understand that during sensing process there could be diffusion of oxygen interstitials or surface reactions related to oxygen adsorption desorption. Along with other things, this established that CuO bundles can carryout the receptor function of a gas sensor, too.

3. Finally, testing performance of CuO bundles network in presence of H_2 and CO, lead us to understand that gas sensing is a complex phenomenon. This is to be noted that during H_2 sensing curve measurements, the environment in the chamber changed from air, i.e presence of oxygen, to H_2 in N_2, void of oxygen. While during CO sensing curve measurements, the environment changed from air to CO in air, with a continuous presence of similar concentration of oxygen. During H_2 sensing, CuO bundles displayed conduction transients in the first 200 s of H_2 exposure, followed by an expected reducing response. We also provided a hypothesis as to what reactions could be dominating to cause the transient. During CO exposure, the response was seen to change from p-type to n-type as operating temperature of the sensor was increased. These are rarely reported phenomena, highlighting the novelty of this work.

Chapter 5

ZnO NRs + CuO platelets heterostructure

In chapter 3, it was established that ZnO NRs + $Cu_2(OH)_3Cl$ platelets form a heterostructure. Here, we discuss the functional characterisation, i.e electronic and gas sensing performance of the heterostructure. We present the electrical characteristics of the post annealed heterostructure in comparison with post annealed ZnO NRs, at various operating temperatures and in presence and absence of light. In chapter 3, we observed that ZnO NRs did not show any absorption in visible light where as heterostructure did. The analysis of IV characteristics in light however, revealed that heterostructure showed no trace of photoconductivity even at low temperatures while current through ZnO NRs was modulated due to presence and absence of light. In the following section, we present hypotheses for such an observation.

Gas sensing characteristics of post annealed heterostructure are presented in comparison with post annealed ZnO NRs and CuO bundles, since these are the two closest nanostructures for comparison and can act as benchmark to asses performance of the heterostructure. We observe that the heterostructure has a p-type response to oxidising and reducing gasses. But, the nature response is not exactly similar to either ZnO NRs or CuO bundles. The fact that all the three materials respond differently to same gasses at different working conditions, can be leveraged for an e-nose application, as will be explained in the following sections.

In the following section, only post annealed samples, mentioned as CuO@ZnO heterostructure, are used.

5.1 Electrical characteristics

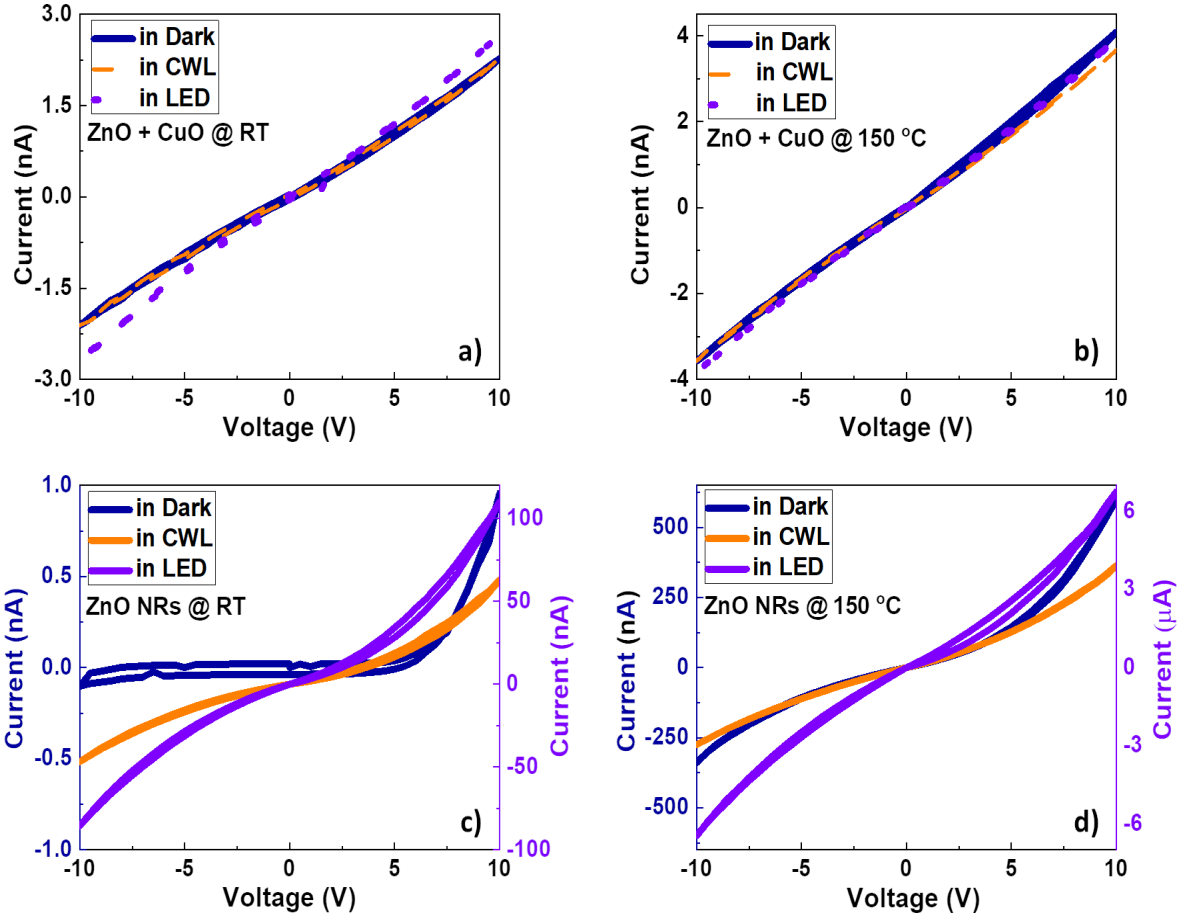

Figure 5.1: IV characteristics of CuO@ZnO heterostructure a) at RT, b) at 150 °C and ZnO NRs c) at RT, d) at 150 °C in dark, in cool white light and in white LED. In all the double y axes plots here, left y axis is for current in dark while right y axis is for current in light, CWL and LED.

IV characteristics of CuO@ZnO heterostructure and ZnO NRs are studied at different operating temperatures and in different lighting conditions. The corresponding plots are shown in Figure 5.1. Let us consider IV characteristics of the heterostructure first, shown in Figure 5.1 a) and b). Current through the heterostructure seemed unaffected by presence or absence of visible light both at RT and at 150 °C operating temperature. This is surprising because the CuO@ZnO heterostructure showed considerable adsorption in the visible wavelength range (figure 3.21). We can assume that light adsorption did not create enough electron hole pairs in the heterostructure so as to affect the flow of charge carriers through them, or the generated electron hole pairs could not participate in conduction due to recombination or

trapping [2, 65]. The current through the heterostructure also seems unaffected by the operating temperature. The current scale at RT and at 150 °C is similar, making this unusual in MOx heterostructures.

The current through the ZnO NRs has a strongly rectifying behaviour, indicating presence of Schottky junctions which dominate the current through the device. The current through ZnO NRs increases with increasing light intensity, both at RT and at 150 °C operating temperature inspite of the fact that ZnO NRs did not show absorption in 400 nm - 700 nm wavelength range. On the other hand it might not be so strange to observe conduction through ZnO NRs being affected by visible light irradiation. We saw that ZnO NRs synthesised in this work showed any adsorption in the visible range roughly around 380 nm, which inline with the fact that researchers have also found pure ZnO based nanostructures absorbing visible light around 380 nm and showing a corresponding photocurrent [135, 136]. It could also be possible that the visible light used to irradiate the ZnO NRs have a component below the wavelength of 400 nm, which causes the change in current on light irradiation. The data sheet of the cool white light shows a small component at 380 nm [137] while that of white LED does not show comment on wavelengths below 400 nm [138].

5.2 Oxygen adsorption-desorption

To study the adsorption - desorption characteristics of CuO@ZnO heterostructure and ZnO NRs, we exposed the devices to 20.9% O_2 followed by N_2 and recorded the response and recovery in Figure 5.2. It is interesting to note here that CuO@ZnO heterostructure behaves like a p-type material showing increase in current on oxygen exposure while ZnO NRs show a n-type response with reduction in current at oxygen exposure. We can propose two hypothesis in support of p-type behaviour of the heterostructure. One, CuO@ZnO form a core shell type of structure where the adsorption-desorption and the conduction primarily takes place through the CuO shell. This could also explain the overall low current observed in the heterostructure as compared to ZnO NRs. in the second hypothesis, we can assume that the heterostructures form network junctions between one another, where only CuO platelets are in contact. Thus the path of current going from one heterostructure to another will be crossing ZnO-CuO-ZnO or n-p-n. Since the nature of the response is p-type and the network junction is also p-type, we can say that the heterostructure network displays a junction based sensitivity. However, we do not sufficient evidence to prove either of these hypotheses.

The CuO@ZnO heterostructure did not show any sensor response at RT and no effect of light at RT nor at 150 °C operating temperature. This is consistent with IV characteristics shown in Figure 5.1 a) and

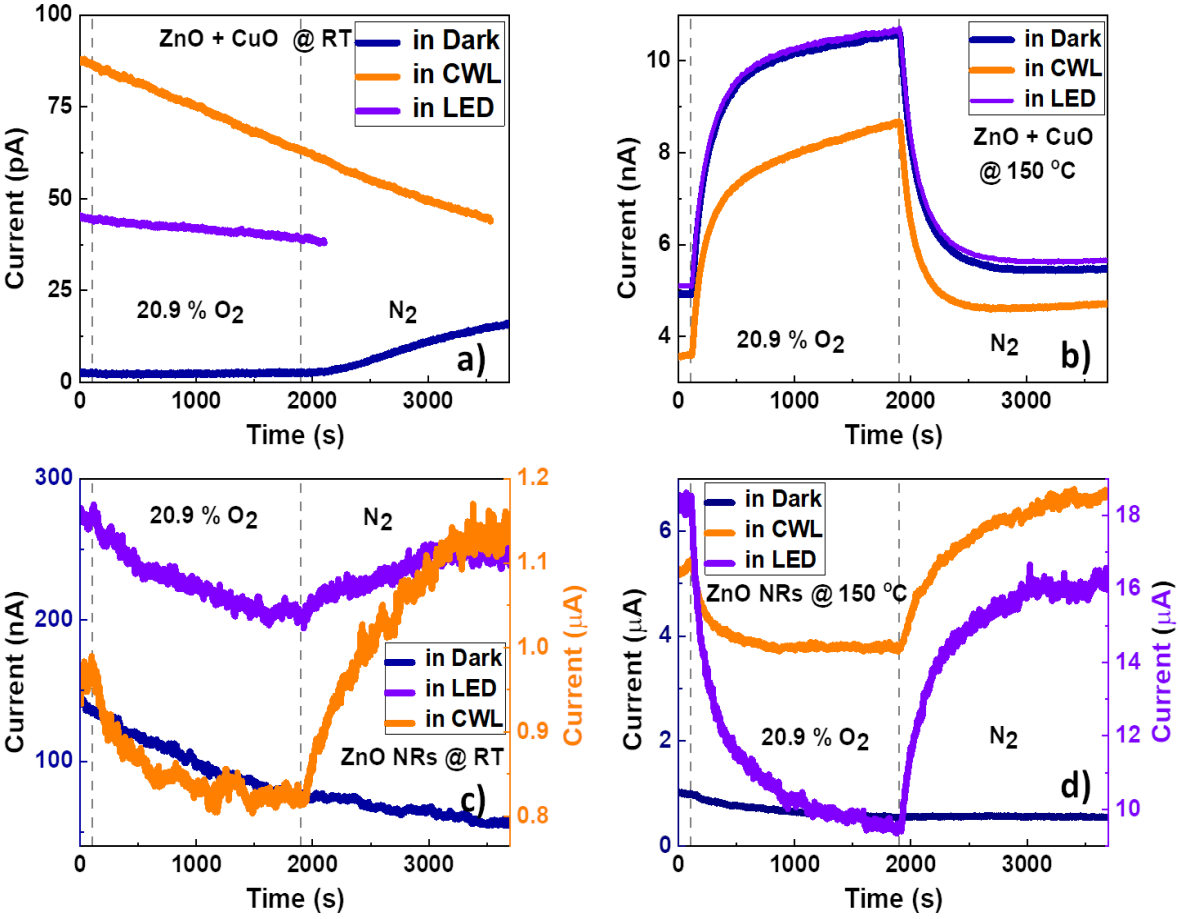

Figure 5.2: Response and recovery of CuO@ZnO heterostructure a) at RT, b) at 150 °C and ZnO NRs c)at RT, d) at 150 °C on exposure to 20.9% O_2 in dark, in cool white light and in white LED.

b). ZnO NRs, even when showed no absorption in visible wavelength range, showed influence of light in IV (Figure 5.1c) and d)), and similarly show effect of light in sensor response too. At RT, ZnO NRs seem to show better sensor response in CWL while at 150 ◦C they perform better under white LED.

Sensor response of CuO@ZnO heterostructure and ZnO NRs is tabulated in table 5.1. Even though overall current flowing in the heterostructure is lower than ZnO NRs, they show a better SR at 150 ◦C, albeit by a very small margin.

Material, Operating temperature	in Dark	in CWL	in LED
CuO@ZnO heterostructure at RT	-	-	-
CuO@ZnO heterostructure at 150 °C	2.14	2.41	2.09
ZnO NRs at RT	-	1.18	1.37
ZnO NRs at 150 °C	-	1.35	1.91

Table 5.1: Sensor response of post annealed CuO@ZnO heterostructure and ZnO NRs to 20.9% O_2 at RT and 150 ∘C operating temperature in dark, CWL and LED

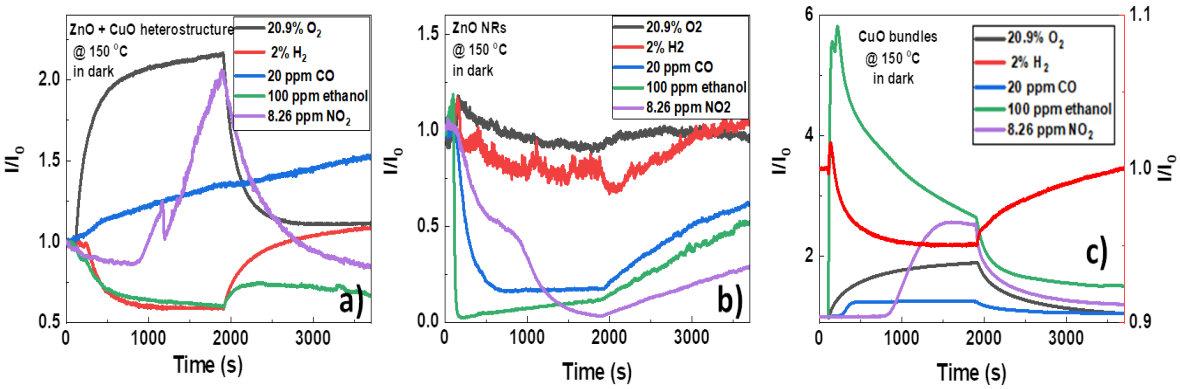

Figure 5.3: Gas sensing performance of a) CuO@ZnO heterostructure, b) ZnO NRs and c) CuO bundles at an operating temperature of 150 °C in dark. The sensors were exposed to 20.9% O_2 with N_2 as recovery environment gas, 2% H_2 in N_2, 20 ppm CO, 100 ppm ethanol, 8.26 ppm NO_2 with synthetic air as recovery environment gas.

5.3 Gas sensing characteristics

To test performance of CuO@ZnO heterostructure in presence of various gasses we expose it to 20.9% O_2 with N_2 as recovery environment gas, 2% H_2 in N_2, 20 ppm CO, 100 ppm ethanol, 8.26 ppm NO_2 with synthetic air as recovery environment gas at an operating temperature of 150 °C in dark. The results are presented in Figure 5.3 a) in comparison with performance of ZnO NRs and CuO bundles to all the same gasses in similar working conditions in Figure 5.3 b) and c), respectively. Gas sensing characteristics of the heterostructure are not tested at RT since it did not show any oxygen adsorption-desorption at RT (Figure 5.2 a)) or in presence of light as it did not show any effect of light on IV characteristics or oxygen adsorption-desorption (Figure 5.1 a) and b), Figure 5.2 a)).

Let us discuss about gas sensing performance of ZnO NRs and CuO bundles first. ZnO NRs show same response of reduction in current to oxidising gasses like O_2, NO_2 and to reducing gasses like H_2, CO and ethanol. This is neither an expected observation nor is it heavily reported in literature. However, Lee *et al.* , observed a similar response from SnO_2 nanoparticles synthesised with a particular recipe towards NO_2

and H_2. They hypothesised that this could occur either due to presence of potassium on the SnO_2 surface left over from the synthesis reactants or due to the fact that the material was treated at low temperature [139]. We can only assume that a similar analogy may apply to these ZnO NRs. The response of ZnO NRs to O_2 and H_2 is noisy, very low and has some current drift. Let there be an imaginary threshold of 20% change in current to consider a response as acceptable. The response of ZnO NRs to O_2 and H_2 does not cross this threshold and thus cannot be considered as a response at all.

Another striking observation that we can make is with regards to response of ZnO NRs to 100 ppm ethanol. We see that ZnO NRs respond very fast to presence of 100 ppm ethanol, however, the long term response experiences drift. Fast response of ZnO nanostructures to ethanol, in dark or under UV illumination, has been reported in literature [140, 141, 142]. For example, Chen *et al.* reported a response time of 6 s and recovery time of 94 s for UV light activated ZnO microspheres sensor operated at 80 °C [140]. This explains the fast, short term response of ZnO NFs to 100 ppm ethanol. However, we cannot compare the long term response measured for 1800 s to literature due to unavailability of similar parameters.

The STEL of NO_2 is known to be 5 ppm while LTEL is 3 ppm. However, we could not achieve this concentration in the chamber with the gas sensing setup currently available. The least concentration we could attain was 8.26 ppm at an increased flow rate of 300 sccm. All the other gas sensing results presented in this thesis have a total gas flow of 100 sccm. Thus, the delay observed in all sensors, CuO@ZnO heterostructure, ZnO NFs and CuO bundles, responding to 8.26 ppm of NO_2 is due to the flow rate and should be ignored. Similar to the slow response of ZnO NFs to 8.26 ppm NO_2, a slow response was also observed by Chizhov *et al.* when nanocrystalline ZnO were exposed to 1 ppm NO_2 at RT over 720 s [143], contrary to a fast response observed by Su *et al.* for UV activated ZnO porous film at TR to 1 ppm NO_2 [144]. It is thus possible that the slow response observed here is due to unavailability of UV light irradiation.

Same goes for CuO bundles. Gas sensing properties of CuO bundles in presence of O_2, H_2 and CO are already discussed in detail in chapter 4, while in presence of NO_2 are described in the appendix and in presence of ethanol are mentioned here for the sake of comparison. Similar to ZnO NRs, CuO bundles showed a very fast response to 100 ppm ethanol followed by a drifting decrease in current in the long term response. A similar drifting response over a time scale of 50 s, was observed by Wang *et al.* when CuO NRs were exposed to concentrations of ethanol higher than 500 ppm at an operating temperature of 300 °C [38]. They attempted an explanation of the sensing mechanism using the surface accumulation model instead of the depletion model generally used for n-type MOx, where conduction takes place through the surface accumulation layer formed on CuO NRs. They explained that drift in long term response occurs

due to sensor saturation, sensor being void of any adsorbed oxygen species that can react with ethanol [38].

Here, the response of CuO bundles to 8.26 ppm of NO_2 confirms the oxidising gas response, i.e. increase in current in presence of oxidising gas, other than O_2. The large delay observed for change in current is attributed to high amount of gas flow, 300 sccm as described earlier, and extremely low concentration of NO_2 that could hinder the detection process.

Comparing Figure 5.3 a), b) and c), we can clearly see that the in the heterostructure, one material is not dominating the SR, but rather there is a synergistic effect of both materials leading to SR different than both the constituent materials. Heterostructure clearly shows a p-type response to oxidising and reducing gasses, while for 20 ppm CO, it shows a response below the threshold, unlike CuO bundles.

Xu *et al.* worked with CuO@ZnO NRs based triethylamine sensors where CuO was in the form of nanoparticles on the ZnO NRs forming a heterostructure. CuO@ZnO heterostructure showed a response type similar to ZnO NRs without CuO nanoparticles, only with enhanced SR of the sensor towards the target gas [54]. A similar observation can be made from works of Yang *et al.* , and Rai *et al.* , where addition of a MOx and formation of a heterostructure maintained the response type but enhanced the overall SR to a target gas [55, 56]. Based on literature , one can expect n-type ZnO NRs to be the nanostructure through which conduction occurs and thus expect the heterostructure to have a response type similar to ZnO NRs [54, 55, 56]. However, in our results, the heterostructure showed a response closer to p-type MOx.

There can be three possible explanations for the p-type response of CuO@ZnO heterostructure, namely, (1) formation of a core-shell structure due to excessive coverage of CuO platelets on the ZnO NRs surface and conduction occurring through the p-type CuO shell, or (2) domination of p-type network junctions on the conduction of majority charge carriers, or (3) p-type doping of ZnO due to CuO nanostructures. Supporting and opposing arguments for each hypothesis are presented below.

(1) Formation of a core-shell structure due to excessive coverage of CuO platelets on the ZnO NRs surface and conduction occurring through the p-type CuO shell: The SEM image of heterostructure in Figure 3.20 c) shows a relatively dense coverage of $Cu_2(OH)_3Cl$ platelets on ZnO NR surface. The dense coverage could lead to a core-shell structure where a conduction pathway is formed through the CuO shell of the heterostructure leading to p-type response. Work of Kaur *et al.* shows that complete coverage of n-type ZnO NWs on the surface of p-type NiO NWs leads to a n-type response for the thus formed NiO/ZnO heterostructure. However, as shown in Figure 5.4, a dense network of $Cu_2(OH)_3Cl$-CuO platelets treated in the same conditions as the heterostructure did not show significant conduction through them. This opposes the hypothesis of a conduction in a CuO shell, which would result in a p-type response.

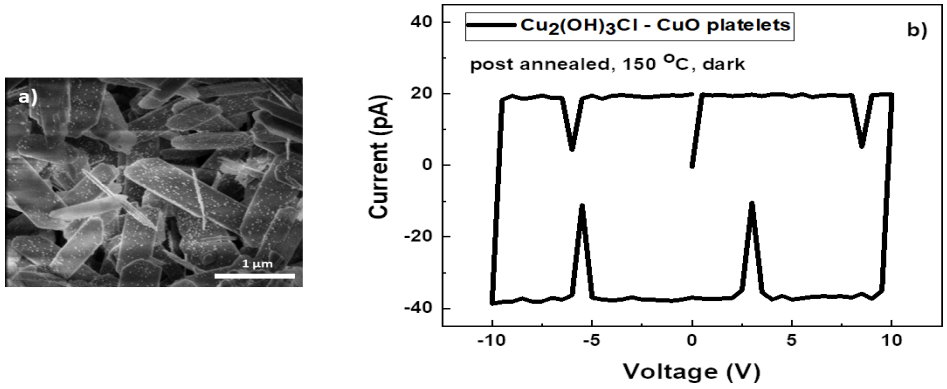

Figure 5.4: a) SEM image of dense network of $Cu_2(OH)_3Cl$-CuO platelets annealed at 200 °C, 2 h b) IV characteristics of post annealed dense network of $Cu_2(OH)_3Cl$-CuO platelets operated at 150 °C in dark showing no conduction through them

(2) Domination of p-type network junctions on the conduction of majority charge carriers: Heterostructures, prepared in solution, are dropcasted on a substrate with gold electrodes as discussed in device fabrication section of chapter 2. This leads to the formation of a network of heterostructure between electrodes, which acts as a conduction path for majority charge carriers. In this network of heterostructures, there are junctions formed between two heterostructures that come in contact. Since p-type CuO is on the outside of the heterostructure, the network junctions would be n (ZnO) - p (CuO) - n (ZnO) type in nature. Thus the majority charge carriers that constitute current through the device have to pass through multiple n-p-n-type junctions from one electrode to the other. The p-type junctions could dominate the conduction through the sensing device to result in an overall p-type response from the heterostructure [145, 146]. To confirm this hypothesis, gas sensing experiments based on isolated single heterostructure would be helpful. This is elaborated in the outlook for this thesis.

(3) p-type doping of ZnO due to CuO nanostructures: The above two hypothesis are based on the assumption that ZnO is n-type while CuO is p-type semiconductor in the heterostructure. We infer that increase in current due to oxygen adsorption means that the majority charge carriers in the heterostructure are holes. It is also possible that presence of high number of CuO (p-type) material on surface of ZnO and undergoing annealing treatment dopes ZnO to be p-type. This hypothesis can also be confirmed or disproved through gas sensing experiment of an isolated single heterostructure, as elaborated in the outlook section of the next chapter.

Table 5.2 tabulates the responses shown in Figure 5.3 for ease of understanding. Here responses are not mentioned as n-type / p-type or oxidising/reducing to avoid confusion. O_2 and H_2 can be considered a s standard oxidising and reducing gas, respectively, mentioned only for representation. A direct application

Material	20.9% O_2	2% H_2	20 ppm CO	100 ppm ethanol	8.26 ppm NO_2
CuO@ZnO	↑	↓	→	↓	↑
ZnO NRs	→	→	↓	↓	↓
CuO bundles	↑	↓	↑	↑	↑

Table 5.2: Indication of type of response of CuO@ZnO heterostructure, ZnO NRs and CuO bundles on exposure to 20.9% O_2 in N_2, 2% H_2 in N_2 , 20 ppm CO, 100 ppm ethanol, 8.26 ppm NO_2 with synthetic air as reference and diluting gas, at an operating temperature of 150 °C in dark. Up arrow indicates increase in current, down arrow indicates decrease in current while a right arrow indicates response that is below the threshold for detection.

of table 5.2 would be for calibration of an e-nose. For example, consider CuO@ZnO heterostructure, ZnO NRs and CuO bundles are deposited on a substrate one after other, each connected to electrodes separately. The device is then operated at 150 °C in dark exposed to a mixture of gasses from the group shown in table 5.2. Observing the nature of responses from all three sensor materials will enable qualitative identification of gasses, which would not be very easy when using only a single material as a gas sensor.

For example upon exposure to an any one gas from the table 5.2 mentioned above, when all the three materials show reduction in current, we can identify the gas H_2. When heterostructure and ZnO NRs show reduction in current but CuO bundles show increase in current, we have ethanol, while when ZnO NRs show reduction in current, CuO bundles show increase in current but heterostructure shows no relative response, we have CO in the test chamber. For O_2 and NO_2, where the nature of change is current through the three materials is the same, quantitative calibration of the SR will help in qualitative differentiation too. However, this qualitative and quantitative identification by the three sensor materials as e-nose is only valid for the gasses shown here. It cannot be generalised to other oxidising or reducing gasses.

Table 5.2 shows nature of response at operating temperature of 150 °C only. But we have seen in chapter 4, that CuO bundles show an inversion of response type to 20 ppm CO in air when operating temperature is modulated. This temperature dependence of nature of response can also be used in an e-nose application for qualitative identification and confirmation of presence of a certain gas in the atmosphere.

5.4 Conclusion

This chapter described functional characterisation of novel CuO@ZnO heterostructure. The first step in determining the functional properties of the heterostructure is to study its IV characteristics. This is the followed by studying the oxygen adsorption-desorption and gas sensing properties of the heterostructure. At each step, the heterostructure characteristics are compared with those of ZnO NRs under similar operating

conditions, as ZnO NRs form the base of the heterostructure. Gas sensing properties of heterostructure are presented in comparison with CuO bundles as well, as CuO bundles is the reference CuO material we have tested during this work. The main conclusions that we can draw from these characterisations are mentioned below.

1. Electrical characterisation of heterostructure, done through IV, revealed that heterostructure either does not show photoconductivity or the photoconductive effect is very low and cannot be observed contributing to the conduction through the network. On the other hand, current through ZnO NRs network is affected by visible light irradiation, which could be due to a component of light specifically at 380 nm the corresponds to the bandgap of the ZnO NFs. We also observed that the current through the heterostructure was not affected by operating temperature either, which is surprising nonetheless. Current through ZnO NRs was highly rectifying, indicating that the junctions formed in the network were affecting the overall conduction.

2. Oxygen adsorption-desorption characteristics of the heterostructure were also largely unaffected while those of ZnO NRs were affected by the visible light irradiation, similar to IV. Heterostructures showed no change in current due to oxygen adsorption-desorption at RT. Based on the nature of change in current observed due to oxygen adsorption-desorption at 150 °C, heterostructures showed p-type response while ZnO showed n-type response. We presented three hypothesis for this observation which require further investigation for confirmation. The three hypothesis are as follows: formation of a core-shell structure where primary adsorption-desorption and conduction happens through a p-type shell, network junction driven sensing where junctions between the heterostructures are of the n-p-n nature, and p-type doped ZnO.

3. Lastly, in gas sensing properties of heterostructures, we present a comparative analysis with ZnO NRs and CuO bundles. This comparison leads us to understand that the heterostructure does not behave like either ZnO NRs or CuO bundles, indicating that there a synergistic effect between both the materials that lead to different sensing performance from the heterostructure. An example of e nose application is presented where qualitative differentiation of gasses can be achieved using the three materials in combination.

Chapter 6

Conclusion and Oulook

6.1 Conclusion

This thesis investigates synthesis and application of MOx nanostructures and heterostructure for low power gas sensing. Let us revisit the objectives we started this thesis with and relate the conclusions drawn from this work to the objectives. In process, we also assess challenges overcome and the novelty of the work done in this thesis.

1. A deeper understanding of what constitutes response and recovery in metal oxide chemiresistive gas sensors

For metal oxide (MOx) chemiresistive gas sensors, oxygen adsorption and desorption reactions on a material's surface play a major role in the sensor kinetics. Studies on response and recovery curves of n-type MOx chemiresistive gas sensors have found that detailed analysis allow to extract parameters like time constants, reaction constants and diffusion coefficients. These derived parameters give more information on the processes occurring during gas sensing. However, such analysis is scarcely preformed for understanding p-type MOx sensors. In this work, we fabricate CuO bundles via a modified low temperature liquid phase synthesis and characterise them using SEM, XRD and XPS. Devices made from CuO bundles network are investigated for their electrical, oxygen adsorption - desorption and gas sensing properties.

It was observed that the sensor has faster response and recovery in as deposited condition in comparison to annealed sensor which can be attributed to sensing at junctions formed between the NWB, overpowering effect of diffusion through the material. A detailed inspection of response and

recovery curves enabled us to derive the above mentioned parameters for CuO bundles. Investigation of the derived parameters, role of network junctions and a hydroxylated CuO surface lead us to discuss the hypotheses for the contributing processes, namely, the diffusion process of gas species and the surface reaction of oxygen with the CuO surface. For as deposited and post annealed CuO NWB, we identify up to two processes in the response and recovery. Based on calculations and comparison with literature, the longer and/or two time constants observed could be attributed to diffusion through solid and/or to adsorption/desorption of oxygen species. In some cases where the time constant was larger than the gas exposure time, it is possible that the second process could not occur in the given time frame and thus only one large time constant is observed.

On exposure of 2% H_2 and 20 ppm CO with synthetic air as a recovery gas, CuO bundles showed conductance transients and inversion of type of response based on operating temperature. These findings are new as compared to p-type MOx and have only been reported before for a few n-type MOx. The cause of conductance transients and temperature dependent inversion of response type was concluded to be competing oxygen adsorption-desorption reactions detailed in chapter 4.

In conclusion, the work done on CuO bundles, specially the method of analysis presented here, can be applicable to studies on gas sensors and will develop a deeper understanding of the sensing mechanism, and to a better optimization of their response and recovery times. Along with this, awareness about the oxygen adsorption-desorption on CuO bundles will allow researchers to better tune the performance of a gas sensors based on this material.

2. Synthesise heterostructure in nanoscale and its characterisation

To synthesise a heterostructure we chose ZnO, due to its conductance and gas sensing properties, and CuO, as it absorbs light in the visible wavelength range.

In the process of obtaining stable CuO nanostructures we discovered $Cu(OH)_2$ NWs, $Cu_2(OH)_3Cl$ nanoplatelets, $Cu_2(OH)_3Cl$ crystals, and Cu_2O truncated cubes, all of which act as intermediate structures to CuO nanostructures. We developed a template-free bottom-up synthesis and shape control of copper hydroxide based nanostructures grown in liquid phase, from 1D NWs to 2D layered nanoplatelets and 3D crystals. Precise control over the pH of the solution and the reaction temperature lead to intended tuning of the morphology and chemical composition of the nanostructures.

We discussed the effects of precursors on the formation of $Cu(OH)_2$ NWs. It is found that the concentration of the base, NaOH, plays a major role in formation of $Cu(OH)_2$ NWs. With the help of formation energy and energy above hull, we inferred that $Cu(OH)_2$ is a metastable material, which

will change its morphology and composition on varying the reaction parameters. We also studied that $Cu_2(OH)_3Cl$ nanoplatelets could be formed due to excess of Cl ions in the solution. The change of $Cu_2(OH)_3Cl$ nanoplatelets to nanocrystals could be explained by space group transformations, Goldsmith's simplexity rule and Ostwald's step rule. Finally, we have been successful in stabilising and extracting the intermediate phase of botallackite ($Cu_2(OH)_3Cl$) in solution for at least 48 hours.

We overcame the challenge of different reaction parameters of individual nanostructures of ZnO and CuO by designing two approaches to prepare a heterostructure. One, synthesise ZnO NRs that are stable in the pH and temperature range of the target CuO nanostructure. Then, add ZnO NRs in the solution before CuO nanostructure precursor and follow the synthesis procedure so that CuO nanostructures grow on the preexisting ZnO NRs. In the second approach, we start with a CuO based nanostructure which is stable in pH and temperature range of ZnO nanostructure and follow the stepped synthesis. The synthesis procedures used to fabricate all the nanostructures were either modified versions of the one available in literature or original work.

For the ZnO NRs + $Cu_2(OH)_3Cl$ nanoplatelets heterostructure developed by the first approach, $Cu_2(OH)_3Cl$ nanoplatelets seem to align naturally onto ZnO NRs surface. Multiple characterisations confirm the formation of the heterostructure. However, for the ZnO NFs + CuO truncated cubes material developed via the second approach, we do not see presence of CuO in morphological and elemental characterisation but only in optical characterisation. Thus, it is concluded not to be a heterostructure.

3. To achieve low power gas sensing with the help of heterostructure and light activation

CuO@ZnO heterostructure showed no change in current due to oxygen adsorption-desorption at RT. However, contradictory to traditional MOx sensors that operate at temperatures as high as 300 °C - 400 °C, heterostructure had oxygen -adsorption-desorption translated as change in conductance as well as gas sensing at 150 °C in dark.

Based on the nature of change in current observed due to oxygen adsorption-desorption at 150 °C, we can conclude, heterostructures showed p-type response. The possible hypothesis for a pytpe response are formation of a network junction driven sensing where junctions between the heterostructures are of the n-p-n nature and p-type doped ZnO. Lastly, a comparative analysis of gas sensing properties of heterostructure, ZnO NRs and CuO bundles leads us to understand that the heterostructure does not behave like either ZnO NRs or CuO bundles, indicating that there a synergistic effect between both the materials that lead to different sensing performance from the heterostructure. An example of e nose application is presented where qualitative differentiation of gasses can be achieved using the three materials in combination.

Light irradiation seem not to affect conductance of CuO bundles and heterostructure when tested at 150 °C. Thus CuO bundles and heterostructure either do not show photoconductivity or the photoconductive effect is very low and cannot be observed contributing to the conduction through the network. Also, it is possible that at 150 °C the number of charge carriers generated due to heat were much larger than those due to light irradiation.

6.2 Outlook

Since research never truly ends, here is an outlook based on the results obtained in this work that can lead to further research. The outlook can largely be divided into two categories. One, short-term clear sub-projects that have a definite aim and a plan that fulfills the aim. Two, a broader spectrum of possible applications of the conclusions drawn from this work.

Let us start with short-term outlook. These propositions can lead to interesting results, however, are not in the scope of this thesis.

1. Humidity is known to degrade sensing response of MOx sensors in general, however, p-type MOx are known to be less sensitive to humidity than n-type MOx in literature. A study of long term stability of CuO bundles either in real time or through accelerated aging process would be interesting to deeply understand the effect of humidity on sensing capacity of CuO bundles network in as deposited and post annealed conditions.
2. CuO@ZnO heterostructure is a new gas sensing material shown to be capable of its unique sensing properties in this thesis. Single heterostructure can be isolated for functional characterisation to isolate sensing characteristics of heterostructure from effect of network junction. This can also help identify if the ZnO, as a part of heterostructure, is doped as p-type or not.
3. Insitu XPS and gas sensing characterisation of heterostructure network will allow us to observed closely the oxygen species that adsorb on the surface of the heterostructure at different operating temperatures. This information will strengthen our understanding of the sensing mechanisms that contribute to the particular response and recovery of heterostructure network to different gasses shown in this work.

The broader outlook for the conclusions drawn from this thesis involves conceptualising fabrication of a heterostructure and envisioning how these materials translate to devices. Some of the ideas are as follows.

1. ZnO NFs + CuO truncated cubes did not form a heterostructure as ZnO does not have a natural tendency to grow on the faces of CuO truncated cubes. Steps can be taken to induce this 'affinity

for natural growth'. One of such steps is an attempt to match at least one of the lattice parameters of CuO to that of rods of ZnO NFs. If we observe the dimensions closely, we see that in the current scenario, CuO truncated cubes have side larger that diameter of rod growing to form a ZnO NFs. Matching of these dimension along with a coating of CuO truncated cubes with ZnO nanoparticle seeds on may promote growth of ZnO on the sides of CuO truncated cube.

2. We discussed a possible application of e nose using CuO@ZnO heterostructure, ZnO NRs and CuO bundles. The e-nose can be made a sophisticated device by incorporating these materials on micro hot plates. Micro hot plates will allow the materials to be operated at different temperatures in a small scale device that consumes low power in heating as compared to traditional hot plate devices. Since the sensing materials can be operated at different temperatures on the same device and the operating temperature can also be modified electronically, we can benefit from the temperature sensitive response characteristics.

References

[1] Chao-Nan Wang et al. "Advances in doped ZnO nanostructures for gas sensor". In: The Chemical Record 20.12 (2020), pp. 1553–1567.

[2] Derek R Miller, Sheikh A Akbar, and Patricia A Morris. "Nanoscale metal oxide-based heterojunctions for gas sensing: a review". In: Sensors and Actuators B: Chemical 204 (2014), pp. 250–272.

[3] Ghenadii Korotcenkov. Handbook of gas sensor materials Volume 1. Springer, 2013.

[4] Anupriya J. T. Naik. "Hetero-junction and Nanomaterial SystemsforMetal Oxide Semiconductor basedGas Sensing". PhD thesis. University College of London, 2015.

[5] Rahul Kumar et al. "Room-temperature gas sensors under photoactivation: from metal oxides to 2D materials". In: Nano-Micro Letters 12.1 (2020), pp. 1–37.

[6] Jordi Samà Monsonís. "New Fabrication Methodologiesfor the Development of Low Power Gas SensorsBased on Semiconducting Nanowires". PhD thesis. Universitat de Barcelona.

[7] Renaud Leturcq, Rutuja Bhusari, and Emanuele Barborini. "Physical mechanisms underpinning conductometric gas sensing propertiesof metal oxide nanostructures". In: Advances in Physics (2022).

[8] N Barsan. "Conduction models in gas-sensing SnO2 layers: grain-size effects and ambient atmosphere influence". In: Sensors and Actuators B: Chemical 17.3 (1994), pp. 241–246.

[9] Nicolae Barsan and Udo Weimar. "Conduction model of metal oxide gas sensors". In: Journal of electroceramics 7.3 (2001), pp. 143–167.

[10] Elisabetta Comini et al. "Stable and highly sensitive gas sensors based on semiconducting oxide nanobelts". In: Applied physics letters 81.10 (2002), pp. 1869–1871.

[11] TI Barry and FS Stone. "The reactions of oxygen at dark and irradiated zinc oxide surfaces". In: Proceedings of the Royal Society of London. Series A. Mathematical and Physical Sciences 255.1280 (1960), pp. 124–144.

[12] Shan-Wei Fan, Arvind K Srivastava, and Vinayak P Dravid. "UV-activated room-temperature gas sensing mechanism of polycrystalline ZnO". In: Applied Physics Letters 95.14 (2009), p. 142106.

[13] Jacques Ghijsen et al. "Electronic structure of Cu 2 O and CuO". In: Physical Review B 38.16 (1988), p. 11322.

[14] Ang Wei, Liuhua Pan, and Wei Huang. "Recent progress in the ZnO nanostructure-based sensors". In: Materials Science and Engineering: B 176.18 (2011), pp. 1409–1421.

[15] TM Xuan, GL Yin, MY Ge, et al. "Research progress on Nano-ZnO gas sensors". In: Materials Review 29.1 (2015), pp. 132–136.

[16] Rafiq Ahmad et al. "Recent progress and perspectives of gas sensors based on vertically oriented ZnO nanomaterials". In: Advances in colloid and interface science 270 (2019), pp. 1–27.

[17] Yanli Kang et al. "Review of ZnO-based nanomaterials in gas sensors". In: Solid State Ionics 360 (2021), p. 115544.

[18] Miaoling Que et al. "Progress in ZnO Nanosensors". In: Sensors 21.16 (2021), p. 5502.

[19] Nohora CAICEDO. "Cycled-growth and transport modelling of ZnO nanowires network towards low-temperature gas sensing". PhD thesis. CEA, Grenoble, 2017.

[20] Nohora Caicedo et al. "Detection mechanism in highly sensitive ZnO nanowires network gas sensors". In: Sensors and Actuators B: Chemical 297 (2019), p. 126602.

[21] Manjeet Kumar et al. "Nano lily-buds garden like ZnO nanostructures based gas sensor for H2 detection". In: Materials Letters 240 (2019), pp. 13–16.

[22] Xiaomei Wang et al. "Highly sensitive, temperature-dependent gas sensor based on hierarchical ZnO nanorod arrays". In: Journal of Materials Chemistry C 3.43 (2015), pp. 11397–11405.

[23] Naila Zubair and Khalida Akhtar. "High performance room temperature gas sensor based on novel morphology of zinc oxide nanostructures". In: Transactions of Nonferrous Metals Society of China 29.1 (2019), pp. 143–156.

[24] Marlene N Cardoza-Contreras et al. "Single ZnO nanowire-based gas sensors to detect low concentrations of hydrogen". In: Sensors 15.12 (2015), pp. 30539–30544.

[25] Hua-Wen Huang et al. "Tunable macro–mesoporous ZnO nanostructures for highly sensitive ethanol and acetone gas sensors". In: RSC advances 5.123 (2015), pp. 101910–101916.

[26] Meiying Ge et al. "Controllable synthesis of hierarchical assembled porous ZnO microspheres for acetone gas sensor". In: Sensors and Actuators B: Chemical 220 (2015), pp. 356–361.

[27] Noboru Yamazoe, Go Sakai, and Kengo Shimanoe. "Oxide semiconductor gas sensors". In: Catalysis Surveys from Asia 7.1 (2003), pp. 63–75.

[28] Xiaowei Li et al. "Octahedral-Like CuO/In2O3 Mesocages with Double-Shell Architectures: Rational Preparation and Application in Hydrogen Sulfide Detection". In: ACS Applied Materials & Interfaces 9.51 (2017). PMID: 29211444, pp. 44632–44640. DOI: 10.1021/acsami.7b15488. eprint: https://doi.org/10.1021/acsami.7b15488. URL: https://doi.org/10.1021/acsami.7b15488.

[29] Ewelina Grabowska et al. "Metal oxide photocatalysts". In: (2018).

[30] Ahmad Sabirin Zoolfakar et al. "Nanostructured copper oxide semiconductors: a perspective on materials, synthesis methods and applications". In: journal of materials chemistry c 2.27 (2014), pp. 5247–5270.

[31] O Akhavan et al. "CuO/Cu (OH) 2 hierarchical nanostructures as bactericidal photocatalysts". In: Journal of Materials Chemistry 21.26 (2011), pp. 9634–9640.

[32] Madalina Elena Grigore et al. "Methods of synthesis, properties and biomedical applications of CuO nanoparticles". In: Pharmaceuticals 9.4 (2016), p. 75.

[33] Stephan Steinhauer et al. "Local CuO nanowire growth on microhotplates: In situ electrical measurements and gas sensing application". In: ACS Sensors 1.5 (2016), pp. 503–507. DOI: 10.1021/acssensors.6b00042. eprint: https://pubs.acs.org/doi/abs/10.1021/acssensors.6b00042?casa_token=NbqqA9n7q98AAAAA:YKYU-dbj8-CPTsCnk9NIJGudC9xrd3tyhAj01XgNOaVY89M_4FQzJMMruxA5TiAsAbSJvcltzzeBsq0u.

[34] Liwei Wang et al. "CuO nanoparticle decorated ZnO nanorod sensor for low-temperature H2S detection". In: Materials Science and Engineering: C 32.7 (2012), pp. 2079–2085.

[35] Qiaobao Zhang et al. "CuO nanostructures: synthesis, characterization, growth mechanisms, fundamental properties, and applications". In: Progress in Materials Science 60 (2014), pp. 208–337.

[36] Dengji Li et al. "Ultra-highly sensitive and selective H2S gas sensor based on CuO with sub-ppb detection limit". In: International Journal of Hydrogen Energy 44.7 (2019), pp. 3985–3992. DOI: 10.1016/j.ijhydene.2018.12.083. eprint: https://pdf.sciencedirectassets.com/271472/1-s2.0-S0360319919X00051/1-s2.0-S0360319918340473/main.pdf?X-Amz-Security-Token=IQoJb3JpZ2luX2VjEJn%2F%2F%2F%2F%2F%2F%2F%2F%2F%2FwEaCXVzLWVhc3QtMSJHMEUCIQCq%2FJ8cuowhD2FrWjgv%2BnY%2Fz72Ci0WJ4HnwPDQIK%2BtimgIgILxXj8%2BGjn4Jyc7zCYUgVoClIiqhvpDiYWYHvZ1jONEqvQMI0f%2F%2F%2F%2F%2F%2F%2F%2F%2FARADGgwwNTkwMDM1NDY4NjUiDJh5h8TEUbF%2B8517rCqRA0nkY5Xs6dVsZed2XER48x7w7P%2B2S%2BnD%2F7FaejXPCkFG3J12Chk2rTJqEgxzJp7I2plewvyaoPUViYwBpQsa%2Bk5BrznGtiHt5j5ghA8qWKMmoR8Qi5dzVzz1o1%2Fa7iuc9nQd7toGPEEfq1BGAUbgBuTiS%2FWebdk%2FS7k984RwhHf6Hnx%

2F8dMQcbFuQ6CtDqG4Mz7FEzL5Yv8 % 2F1nvSESV03PXCYZv56kd % 2BZP06q5NlfGpFgC8uAKGo3T4cIukwFVV0d1iGRUR7yZUtiIknfFzccC71ZQH0RVuvKL29vAUTPF% 2BcoHLK9 % 2BZecHqInHKYE35yJb9bvG3sbkAi9 % 2FO5mRsB0ke0AMjgdGUaCLL3PH3f % 2B1zg4rwrha6g % 2BF % 2B0nqn1AqwHFvNLVojSB9QmIf8J9HcTvmIJQCoBfL3 % 2ByGr % 2BoDEz0QSQlFy1ESNrcMxhnP572bq22SWX84iK364MkfTtjFjGwvPN1eRFObCwXHHxw7PF41TFGgQQUUzG0 2Fgu0HHfsAEIQCVVpqW9jZWVwWTCNQEzMtOjmCMhkidu3SP7tWfMPES % 2B8KoIKMuHKSnXTrP7tonTPJdQsZN % 2BCxGwVRUBCp8ba4Lih9jUry4qg % 2BLDek9kq7R6B1RMc0cZE0BxQRefqdT8dm % 2F1n3o1oSZ % 2Bxo % 2BdOVHULyJGMRMua37u8HKmjZx9vc4f4qpFRywvQJSKNqd9tEFDVRN7ySeBig0PoBnidMNRxEBFmXX4iQo2 2BnZHzSPGk0vgkZe4UFhjxs0J3te4Azlg%2FA9KCzsNGUh0VBEzrWkxzMDw%3D%3D&X-Amz-Algorithm=AWS4-HMAC-SHA256&X-Amz-Date=20200508T093326Z&X-Amz-SignedHeaders=host&X-Amz-Expires=300&X-Amz-Credential=ASIAQ3PHCVTY4GF2LZ6B%2F20200508%2Fus-east-1%2Fs3%2Faws4_request&X-Amz-Signature=853ec914aa51bf7a9c6f167d1e3a111752e88f68300c2201c719fcdb9c538b2d&hash=e5fbe22b45f0dcb524342511d1ad7f8f3815b7fba814fd5ca4041cad4b50925a&host=68042c943591013ac2b2430a89b270f6af2c76d8dfd086a07176afe7c76c2c61&pii=S0360319918340473&tid=spdf-f39cf5e9-d9b5-401a-b884-eab9dd66bfd6&sid=57300773309496471709300548502 2cdd886gxrqb&type=client.

[37] ME Mazhar et al. "Kelvin probe as an effective tool to develop sensitive p-type CuO gas sensors". In: Sensors and Actuators B: Chemical 222 (2016), pp. 1257–1263. DOI: 10.1016/j.snb.2015.05.050. eprint: https://www.sciencedirect.com/science/article/abs/pii/S0925400515006693#aep-article-footnote-id10.

[38] C Wang et al. "Surface accumulation conduction controlled sensing characteristic of p-type CuO nanorods induced by oxygen adsorption". In: Nanotechnology 18.14 (2007), p. 145506. DOI: 10.1088/0957-4484/18/14/145506. eprint: https://iopscience.iop.org/article/10.1088/0957-4484/18/14/145506.

[39] Jiajun Chen et al. "H2S detection by vertically aligned CuO nanowire array sensors". In: The Journal of Physical Chemistry C 112.41 (2008), pp. 16017–16021. DOI: 10.1021/jp805919t. URL: https://pubs.acs.org/doi/abs/10.1021/jp805919t.

[40] Nguyen Duc Hoa et al. "Synthesis of porous CuO nanowires and its application to hydrogen detection". In: Sensors and Actuators B: Chemical 146.1 (2010), pp. 266–272.

[41] Lin Hou et al. "CO gas sensors based on p-type CuO nanotubes and CuO nanocubes: Morphology and surface structure effects on the sensing performance". In: Talanta 188 (2018), pp. 41–49. DOI: 10.1016/j.talanta.2018.05.059. eprint: https://www-sciencedirect-com.proxy.bnl.lu/science/article/pii/S0039914018305514?via%3Dihub.

[42] Oleg Lupan et al. "Influence of CuO nanostructures morphology on hydrogen gas sensing performances". In: Microelectronic Engineering 164 (2016), pp. 63–70. DOI: 10.1016/j.mee.2016.07.008. eprint: https://www.sciencedirect.com/science/article/abs/pii/S0167931716303689.

[43] Laurent Schlur et al. "Cu (OH) 2 and CuO nanorod synthesis on piezoresistive cantilevers for the selective detection of nitrogen dioxide". In: Sensors 18.4 (2018), p. 1108.

[44] DP Volanti et al. "Monitoring a CuO gas sensor at work: an advanced in situ X-ray absorption spectroscopy study". In: Physical Chemistry Chemical Physics 17.28 (2015), pp. 18761–18767. DOI: 10.1039/C5CP02150B. URL: https://pubs.rsc.org/en/content/articlelanding/2015/cp/c5cp02150b#!divAbstract.

[45] Qiaobao Zhang et al. "Synthesis, characterization, and application of nano cupric oxide". In:
Nanostructures: Properties, Production Methods and Applications: properties, production methods and a
Nova Science Publishers, Inc., 2013, pp. 111–150.

[46] Ho Soonmin and Emmanuel Ajenifuja. "A short review of recent advances in copper oxide nanostructured thin films". In: Research Journal of Chemistry and Environment Vol 23 (2019), p. 6.

[47] Hyo-Joong Kim and Jong-Heun Lee. "Highly sensitive and selective gas sensors using p-type oxide semiconductors: Overview". In: Sensors and Actuators B: Chemical 192 (2014), pp. 607–627.

[48] Qi Lei et al. "Three-dimensional hierarchical CuO gas sensor modified by Au nanoparticles". In: Journal of Semiconductors 40.2 (2019), p. 022101.

[49] Ying Li et al. "Microwave-assisted hydrothermal synthesis of copper oxide-based gas-sensitive nanostructures". In: Rare Metals (2020), pp. 1–17.

[50] Wen Zeng, Tianmo Liu, and Zhongchang Wang. "Sensitivity improvement of TiO2-doped SnO2 to volatile organic compounds". In: Physica E: Low-dimensional Systems and Nanostructures 43.2 (2010), pp. 633–638.

[51] Bin Wu et al. "Visible-light activated ZnO/CdSe heterostructure-based gas sensors with low operating temperature". In: Applied Surface Science 360 (2016), pp. 652–657.

[52] Mark Mashock et al. "Modulating gas sensing properties of CuO nanowires through creation of discrete nanosized p–n junctions on their surfaces". In: ACS applied materials & interfaces 4.8 (2012), pp. 4192–4199.

[53] Hyung-Sik Woo et al. "Highly sensitive and selective trimethylamine sensor using one-dimensional ZnO–Cr2O3 hetero-nanostructures". In: Nanotechnology 23.24 (2012), p. 245501.

[54] Qi Xu et al. "Near room-temperature triethylamine sensor constructed with CuO/ZnO PN heterostructural nanorods directly on flat electrode". In: Sensors and Actuators B: Chemical 225 (2016), pp. 16–23.

[55] Xueli Yang et al. "One step synthesis of branched SnO2/ZnO heterostructures and their enhanced gas-sensing properties". In: Sensors and Actuators B: Chemical 281 (2019), pp. 415–423.

[56] Prabhakar Rai et al. "Functionalization of ZnO nanorods by CuO nanospikes for gas sensor applications". In: RSC Advances 4.45 (2014), pp. 23604–23609.

[57] Noboru Yamazoe and Kengo Shimanoe. "Theory of power laws for semiconductor gas sensors". In: Sensors and Actuators B: Chemical 128.2 (2008), pp. 566–573.

[58] Seymen Aygün and David Cann. "Response kinetics of doped CuO/ZnO heterocontacts". In: The Journal of Physical Chemistry B 109.16 (2005), pp. 7878–7882.

[59] Lili Wang et al. "Hybrid Co3O4/SnO2 core–shell nanospheres as real-time rapid-response sensors for ammonia gas". In: ACS applied materials & interfaces 8.10 (2016), pp. 6539–6545.

[60] Sun-Jung Kim et al. "One-pot hydrothermal synthesis of CuO–ZnO composite hollow spheres for selective H2S detection". In: Sensors and Actuators B: Chemical 168 (2012), pp. 83–89.

[61] G Korotcenkov and BK Cho. "Metal oxide composites in conductometric gas sensors: Achievements and challenges". In: Sensors and Actuators B: Chemical 244 (2017), pp. 182–210.

[62] Liang Peng et al. "Size-and photoelectric characteristics-dependent formaldehyde sensitivity of ZnO irradiated with UV light". In: Sensors and Actuators B: Chemical 148.1 (2010), pp. 66–73.

[63] Xin Geng, Chao Zhang, and Marc Debliquy. "Cadmium sulfide activated zinc oxide coatings deposited by liquid plasma spray for room temperature nitrogen dioxide detection under visible light illumination". In: Ceramics International 42.4 (2016), pp. 4845–4852.

[64] Kundan Kumar and Anirban Chowdhury. "Use of novel nanostructured photocatalysts for the environmental sustainability of wastewater treatments". In: (2020).

[65] Jing Wang et al. "Light-activated room-temperature gas sensors based on metal oxide nanostructures: A review on recent advances". In: Ceramics International (2020).

[66] Xingsong Su et al. ""Close network" effect of a ZnO micro/nanoporous array allows high UV-irradiated NO 2 sensing performance". In: RSC advances 7.34 (2017), pp. 21054–21060.

[67] E Comini et al. "Light enhanced gas sensing properties of indium oxide and tin dioxide sensors". In: Sensors and Actuators B: Chemical 65.1-3 (2000), pp. 260–263.

[68] Benjamin J Hansen et al. "Transport, analyte detection, and opto-electronic response of p-type CuO nanowires". In: The Journal of Physical Chemistry C 114.6 (2010), pp. 2440–2447.

[69] Sunghoon Park et al. "Synergistic effects of a combination of Cr2O3-functionalization and UV-irradiation techniques on the ethanol gas sensing performance of ZnO nanorod gas sensors". In: ACS applied materials & interfaces 8.4 (2016), pp. 2805–2811.

[70] N Ababii et al. "H 2 gas sensing properties of a ZnO/CuO and ZnO/CuO/Cu 2 O Heterostructures". In: Society of Photo-Optical Instrumentation Engineers (SPIE) Conference Series. Vol. 10105. 2017, 101052A.

[71] YH Navale et al. "Enhanced NO2 sensing aptness of ZnO nanowire/CuO nanoparticle heterostructure-based gas sensors". In: Ceramics International 45.2 (2019), pp. 1513–1522.

[72] Li-Yang Hong et al. "Low concentration NO gas sensing under ambient environment using Cu2O nanoparticle modified ZnO nanowires". In: Materials Letters 185 (2016), pp. 243–246.

[73] Mathias Hoppe et al. "(CuO-Cu2O)/ZnO: Al heterojunctions for volatile organic compound detection". In: Sensors and Actuators B: Chemical 255 (2018), pp. 1362–1375.

[74] Wen-Chung Lu et al. "Au/Cu2O/ZnO ternary nanocomposite for low concentration NO2 gas sensing at room temperature". In: Materials Letters 256 (2019), p. 126657.

[75] N Caicedo et al. "Aspect ratio improvement of ZnO nanowires grown in liquid phase by using step-by-step sequential growth". In: CrystEngComm 18.29 (2016), pp. 5502–5511.

[76] Niranjan S Ramgir et al. "Room temperature H2S sensor based on Au modified ZnO nanowires". In: Sensors and Actuators B: Chemical 186 (2013), pp. 718–726.

[77] Sheng Xu and Zhong Lin Wang. "One-dimensional ZnO nanostructures: solution growth and functional properties". In: Nano Research 4.11 (2011), pp. 1013–1098.

[78] Yu Ling-min et al. "Shape controlled cluster growth of ZnO nanoflowers using sol–gel method". In: Micro & Nano Letters 7.10 (2012), pp. 1046–1048.

[79] Vedentam Srikant and David R Clarke. "On the optical band gap of zinc oxide". In: Journal of Applied Physics 83.10 (1998), pp. 5447–5451.

[80] Christof Wöll. "The chemistry and physics of zinc oxide surfaces". In: Progress in surface science 82.2-3 (2007), pp. 55–120.

[81] S Roy Morrison. "Selectivity in semiconductor gas sensors". In: Sensors and actuators 12.4 (1987), pp. 425–440.

[82] Mark C Biesinger et al. "Resolving surface chemical states in XPS analysis of first row transition metals, oxides and hydroxides: Sc, Ti, V, Cu and Zn". In: Applied surface science 257.3 (2010), pp. 887–898.

[83] Rutuja Bhusari et al. "Morphology control of copper hydroxide based nanostructures in liquid phase synthesis". In: Journal of Crystal Growth 570 (2021), p. 126225.

[84] Rutuja Bhusari et al. "Oxygen adsorption and desorption kinetics in gas sensorsbased on CuO nanowire bundle networks". In: submitted (2022).

[85] Haolan Xu et al. "Hierarchical-oriented attachment: from one-dimensional Cu (OH) 2 nanowires to two-dimensional CuO nanoleaves". In: Crystal Growth and Design 7.12 (2007), pp. 2720–2724. DOI: 10 . 1021 / cg060727k. URL: https://pubs.acs.org/doi/full/10.1021/cg060727k.

[86] Christian Engelbrekt et al. "Selective synthesis of clinoatacamite Cu 2 (OH) 3 Cl and tenorite CuO nanoparticles by pH control". In: Journal of nanoparticle research 16.8 (2014), p. 2562.

[87] Mark C Biesinger. "Advanced analysis of copper X-ray photoelectron spectra". In: Surface and Interface Analysis 49.13 (2017), pp. 1325–1334.

[88] John F Moulder. Handbook of X-ray photoelectron spectroscopy. Eden Prairie, 1995, pp. 230–232.

[89] S Poulston et al. "Surface oxidation and reduction of CuO and Cu2O studied using XPS and XAES". In: Surface and Interface Analysis: An International Journal devoted to the development and application of t 24.12 (1996), pp. 811–820.

[90] Linda S Dake, David E King, and Alvin W Czanderna. "Ion scattering and X-ray photoelectron spectroscopy of copper overlayers vacuum deposited onto mercaptohexadecanoic acid self-assembled monolayers". In: Solid state sciences 2.8 (2000), pp. 781–789.

[91] Yanxia Li et al. "Molecularly imprinted fluorescent and colorimetric sensor based on TiO 2@ Cu (OH) 2 nanoparticle autocatalysis for protein recognition". In: Journal of Materials Chemistry B 1.9 (2013), pp. 1256–1262. DOI: 10.1039/C2TB00398H. URL: https://pubs.rsc.org/en/content/articlelanding/2013/TB/C2TB00398H#!divAbstract.

[92] R Pappalardo. "Absorption spectra of Cu2+ in different crystal coordinations". In: Journal of Molecular Spectroscopy 6 (1961), pp. 554–571.

[93] Liangmiao Zhang et al. "Facile synthesis of leaf-like Cu (OH) 2 and its conversion into CuO with nanopores". In: Acta Physico-Chimica Sinica 24.12 (2008), pp. 2257–2262.

[94] KV Gurav et al. "Room temperature chemical synthesis of Cu (OH) 2 thin films for supercapacitor application". In: Journal of alloys and compounds 573 (2013), pp. 27–31. DOI: 10.1016/j.jallcom.2013.03.193. URL: https://www.sciencedirect.com/science/article/abs/pii/S092583881300724X.

[95] Ningning Ba et al. "3D rod-like copper oxide with nanowire hierarchical structure: Ultrasound assisted synthesis from Cu2 (OH) 3NO3 precursor, optical properties and formation mechanism". In: Solid State Sciences 53 (2016), pp. 23–29.

[96] Yan-Hong Luo et al. "Formation of positively charged copper hydroxide nanostrands and their structural characterization". In: Chemistry of materials 18.7 (2006), pp. 1795–1802. DOI: 10.1021/cm052270s. URL: https://pubs.acs.org/doi/abs/10.1021/cm052270s.

[97] Anubhav Jain et al. "The Materials Project: A materials genome approach to accelerating materials innovation". In: APL Materials 1.1 (2013), p. 011002. ISSN: 2166532X. DOI: 10.1063/1.4812323. URL: http://link.aip.org/link/AMPADS/v1/i1/p011002/s1%5C&Agg=doi.

[98] Ankit Agrawal et al. "A formation energy predictor for crystalline materials using ensemble data mining". In: 2016 IEEE 16th International Conference on Data Mining Workshops (ICDMW). IEEE. 2016, pp. 1276–1279.

[99] Sergey V Krivovichev, Frank C Hawthorne, and Peter A Williams. "Structural complexity and crystallization: the Ostwald sequence of phases in the Cu 2 (OH) 3 Cl system (botallackite–atacamite–clinoatacamite)". In: Structural Chemistry 28.1 (2017), pp. 153–159. DOI: 10.1007/s11224-016-0792-z. URL: https://link.springer.com/article/10.1007/s11224-016-0792-z.

[100] Julian R Goldsmith. "A" simplexity principle" and its relation to" ease" of crystallization". In: The Journal of Geology 61.5 (1953), pp. 439–451.

[101] AM Pollard, RG Thomas, and PA Williams. "Synthesis and stabilities of the basic copper (II) chlorides atacamite, paratacamite and botallackite". In: Mineralogical Magazine 53.373 (1989), pp. 557–563.

[102] Thomas Malcherek and Jochen Schlüter. "Structures of the pseudo-trigonal polymorphs of Cu2 (OH) 3Cl". In: Acta Crystallographica Section B: Structural Science 65.3 (2009), pp. 334–341.

[103] Shiqiang Zhou et al. "Design of hollow dodecahedral Cu2O nanocages for ethanol gas sensing". In: Materials Letters 247 (2019), pp. 15–18.

[104] Shixiu Cao et al. "Hydrothermal synthesis, characterization and gas sensing properties of novel Cu2O open hollow nanospheres". In: Ceramics International 43.5 (2017), pp. 4721–4724.

[105] Chun-Hong Kuo and Michael H Huang. "Facile synthesis of Cu2O nanocrystals with systematic shape evolution from cubic to octahedral structures". In: The Journal of Physical Chemistry C 112.47 (2008), pp. 18355–18360.

[106] Anneli Önsten et al. "Probing the valence band structure of Cu 2 O using high-energy angle-resolved photoelectron spectroscopy". In: Physical Review B 76.11 (2007), p. 115127.

[107] MTS Nair et al. "Chemically deposited copper oxide thin films: structural, optical and electrical characteristics". In: Applied Surface Science 150.1-4 (1999), pp. 143–151.

[108] W Gao et al. "Oxidation behaviour of Cu thin films on Si wafer at 175–400 C". In: Materials Letters 51.1 (2001), pp. 78–84.

[109] Caihong Wang. "Triethylamine sensing properties of ZnO nanostructures prepared by hydrothermal method at different pH values". In: Chemical Physics Letters 749 (2020), p. 137471.

[110] G Korotcenkov et al. "Kinetics of indium oxide-based thin film gas sensor response: The role of "redox" and adsorption/desorption processes in gas sensing effects". In: Thin Solid Films 515.7-8 (2007), pp. 3987–3996.

[111] Ghenadii Korotcenkov et al. "The nature of processes controlling the kinetics of indium oxide-based thin film gas sensor response". In: Sensors and Actuators B: Chemical 128.1 (2007), pp. 51–63.

[112] A Maity, A Ghosh, and SB Majumder. "Understanding the anomalous conduction behavior in 'n'type tungsten oxide thin film during hydrogen gas sensing: Kinetic analyses of conductance transients". In: Sensors and Actuators B: Chemical 220 (2015), pp. 949–957.

[113] Elisabetta Comini. "Metal oxide nanowire chemical sensors: innovation and quality of life". In: Materials Today 19.10 (2016), pp. 559–567.

[114] Bharti Singh and BR Mehta. "Relationship between nature of metal-oxide contacts and resistive switching properties of copper oxide thin film based devices". In: Thin Solid Films 569 (2014), pp. 35–43.

[115] Daihua Zhang et al. "Detection of NO2 down to ppb levels using individual and multiple In2O3 nanowire devices". In: Nano letters 4.10 (2004), pp. 1919–1924.

[116] M-W Ahn et al. "On-chip fabrication of ZnO-nanowire gas sensor with high gas sensitivity". In: Sensors and Actuators B: Chemical 138.1 (2009), pp. 168–173.

[117] Bahaa EA Saleh and Malvin Carl Teich. Fundamentals of photonics. john Wiley & sons, 2019.

[118] Go Sakai et al. "Theory of gas-diffusion controlled sensitivity for thin film semiconductor gas sensor". In: Sensors and Actuators B: Chemical 80.2 (2001), pp. 125–131.

[119] Abhishek Ghosh and SB Majumder. "Modeling the sensing characteristics of chemi-resistive thin film semi-conducting gas sensors". In: Physical Chemistry Chemical Physics 19.34 (2017), pp. 23431–23443.

[120] K Mukherjee and SB Majumder. "Analyses of response and recovery kinetics of zinc ferrite as hydrogen gas sensor". In: Journal of Applied Physics 106.6 (2009), p. 064912.

[121] K Mukherjee and SB Majumder. "Analyses of conductance transients to address the selectivity issue of zinc ferrite gas sensors". In: Electrochemical and Solid State Letters 13.4 (2010), J25.

[122] K Mukherjee, DC Bharti, and SB Majumder. "Solution synthesis and kinetic analyses of the gas sensing characteristics of magnesium ferrite particles". In: Sensors and Actuators B: Chemical 146.1 (2010), pp. 91–97.

[123] K Mukherjee and SB Majumder. "Reducing gas sensing behavior of nano-crystalline magnesium–zinc ferrite powders". In: Talanta 81.4-5 (2010), pp. 1826–1832.

[124] Thomas Raphael Marrero and Edward Allen Mason. "Gaseous diffusion coefficients". In: Journal of Physical and Chemical Reference Data 1.1 (1972), pp. 3–118.

[125] Clifford K Ho and Stephen W Webb. Gas transport in porous media. Vol. 20. Springer, 2006.

[126] Igor Medveď and Robert Černỳ. "Surface diffusion in porous media: A critical review". In: Microporous and Mesoporous Materials 142.2-3 (2011), pp. 405–422.

[127] B Kamp, R Merkle, and J Maier. "Chemical diffusion of oxygen in tin dioxide". In: Sensors and Actuators B: Chemical 77.1-2 (2001), pp. 534–542.

[128] J. Crank. The Mathematics of Diffusion. Clarendon Press, Oxford, 1975.

[129] Noboru Yamazoe et al. "Interactions of tin oxide surface with O2, H2O and H2". In: Surface Science 86 (1979), pp. 335–344.

[130] A Bielański and M Najbar. "Adsorption species of oxygen on the surfaces of transition metal oxides". In: Journal of Catalysis 25.3 (1972), pp. 398–406.

[131] Peter Boeker, Oliver Wallenfang, and Gerhard Horner. "Mechanistic model of diffusion and reaction in thin sensor layers—the DIRMAS model". In: Sensors and Actuators B: Chemical 83.1-3 (2002), pp. 202–208.

[132] EA Makeeva, MN Rumyantseva, and AM Gas' kov. "Kinetics of interaction of thick nanocrystalline SnO 2 films with oxygen". In: Inorganic materials 40.2 (2004), pp. 161–165.

[133] H-J Michel et al. "Adsorbates and their effects on gas sensing properties of sputtered SnO2 films". In: Applied surface science 126.1-2 (1998), pp. 57–64.

[134] V Golovanov et al. "The Influence of Structural Factors on Sensitivity of SnO~ 2-Based Gas Sensors to CO in Humid Atmosphere". In: UKRAINS'KYI FIZYCHNYI ZHURNAL 50.4 (2005), p. 373.

[135] Lina Han et al. "Study on formaldehyde gas-sensing of In 2 O 3-sensitized ZnO nanoflowers under visible light irradiation at room temperature". In: Journal of Materials Chemistry 22.25 (2012), pp. 12915–12920.

[136] Qiang Geng et al. "Gas sensing property of ZnO under visible light irradiation at room temperature". In: Sensors and Actuators B: Chemical 188 (2013), pp. 293–297.

[137] Philips. T5 Preheat F8T5/CW PH 25PK. Tech. rep. Philips Lighting, 2019. URL: https://www.usa.lighting.philips.com/api/assets/v1/file/PhilipsLighting/content/fp928001003321-pss-en_us/928001003321_NA.en_US.PROF.FP.pdf.

[138] Thorlabs. Mounted LED, 6500 K MCWHL6. datasheet MTN015246 -S01, Rev A. Thorlabs, Oct. 2019.

[139] Szu-Hsuan Lee et al. "Finely tuned SnO2 nanoparticles for efficient detection of reducing and oxidizing gases: the influence of alkali metal cation on gas-sensing properties". In: ACS applied materials & interfaces 10.12 (2018), pp. 10173–10184.

[140] Yi Chen et al. "UV activated hollow ZnO microspheres for selective ethanol sensors at low temperatures". In: Sensors and Actuators B: Chemical 232 (2016), pp. 158–164.

[141] Ekasiddh Wongrat et al. "Low temperature ethanol response enhancement of ZnO nanostructures sensor decorated with gold nanoparticles exposed to UV illumination". In: Sensors and Actuators A: Physical 251 (2016), pp. 188–197.

[142] Lina Han et al. "Influence of annealing temperature on the photoelectric gas sensing of Fe-doped ZnO under visible light irradiation". In: Sensors and Actuators B: Chemical 177 (2013), pp. 34–40.

[143] AS Chizhov et al. "Visible light activated room temperature gas sensors based on nanocrystalline ZnO sensitized with CdSe quantum dots". In: Sensors and Actuators B: Chemical 205 (2014), pp. 305–312.

[144] Xingsong Su et al. "Structure and thickness-dependent gas sensing responses to NO2 under UV irradiation for the multilayered ZnO micro/nanostructured porous thin films". In: Journal of colloid and interface science 503 (2017), pp. 150–158.

[145] PJM Isherwood. "Copper zinc oxide: Investigation into a p-type mixed metal oxide system". In: Vacuum 139 (2017), pp. 173–177.

[146] Bernabé Marí et al. “p-Type behaviour of electrodeposited ZnO: Cu films”. In: Journal of Solid State Electrochemistry 16.6 (2012), pp. 2261–2265.

Appendices

1. CuO bundles - gas sensing - nitrogen dioxide (NO_2):

NO_2, being an oxidising gas, is expected to cause similar change in current passing through CuO bundles sensors as when they are exposed to oxygen. The LTEL is 3 ppm while STEL for NO_2 is 5 ppm. Given the configurations of the gas mixing system we have installed and the concentration of the gas bottle available, we can only reach a minimum concentration of 8.26 ppm with a total flow rate of 307.5 sccm. Figure 6.1 a) and b) shows a response and recovery curve of post annealed CuO bundles to 8.26 ppm and 20 ppm NO_2 in air at 150 °C operating temperature in dark, respectively. The response curve is as expected for a p-type MOx would behave in presence of an oxidising gas. However, the response is largely delayed, especially in Figure 6.1 a). This could be because of the high flow rate and extremely low concentration of NO_2.

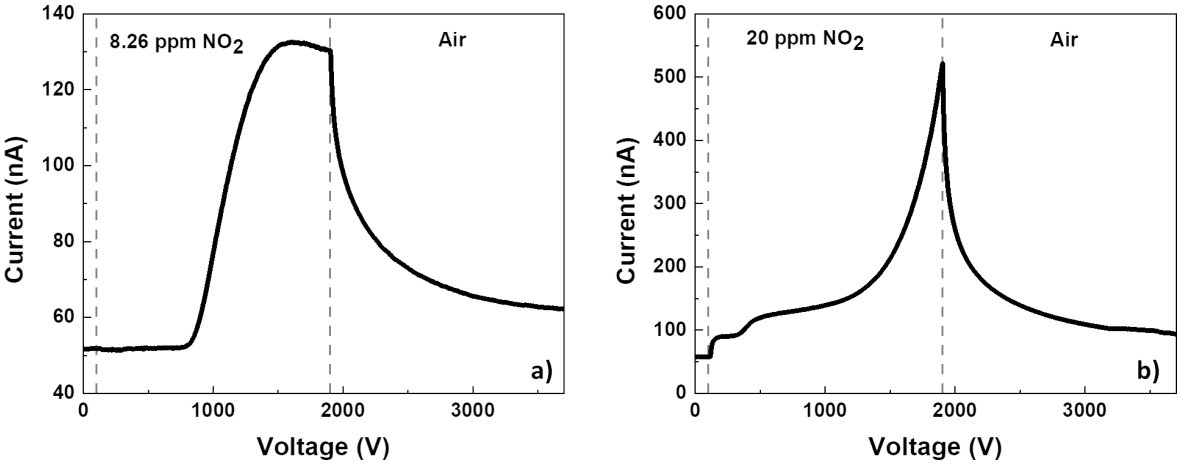

Figure 6.1: Sensor response to a) 8.26 ppm and b) 20 ppm NO_2 in synthetic air.

Figure 6.1 b) shows a two stepped response curve to 20 ppm NO_2 followed by an exponential increase in current which did not reach saturation in 1800 s. Though this is an unusual response, it is not explored further due to two reasons. First, 20 ppm NO_2 concentration at which such a response is observed is four times the STEL. Any sensor detecting such high values of concentration of a hazardous gas is not interesting in terms of its application. It simply means that the CuO bundles network is not a candidate for being used a NO_2 sensor. Second, The observations shown in figure 6.1 were made at a flow rate greater than 300 sccm. This means that the test chamber, which has a volume of 50 cc, has its environment renewed at least every 6 seconds. This is a very short time given to the sensor to detect the gas before the air is completely renewed. Thus the observations showed not be relied upon to the correct response to low concentrations of NO_2.

2. Cu_2O truncated cubes

Synthesis and characterisation of Cu_2O truncated cubes was presented in chapter 3 section 3.1.3. Here, we focus on electrical characteristics, namely current voltage (IV) measurements and gas sensing properties of the devices consisting Cu_2O truncated cubes network. The device preparation is described in chapter 2 section 2.1.3

IV characteristics

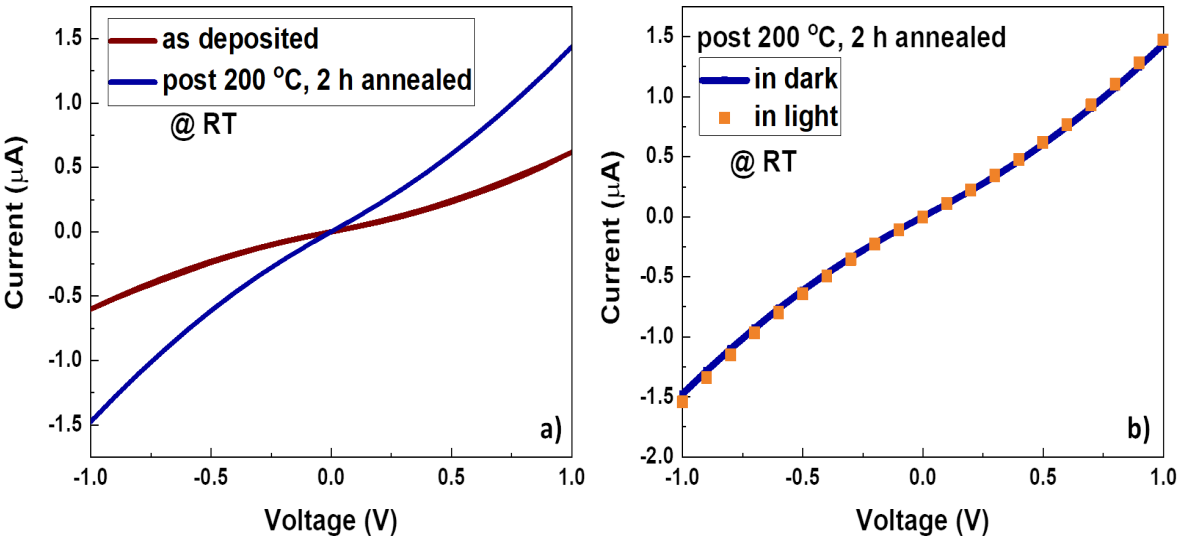

Figure 6.2: Current voltage characteristics of Cu_2O truncated cubes a) a comparison between as deposited and post annealed Cu_2O truncated cubes measured at room temperature in dark, b) a comparison between IV of post annealed Cu_2O truncated cubes measured at room temperature in dark and in light.

IV characteristics of Cu_2O truncated cubes were observed at various operating conditions as shown in Figure 6.2. Voltage was swept from 0 V to 1 V, 1 V to -1 V and back to 0 V with a step size of 100 mV and current through the device was plotted. Figure 6.2 a) presents a comparison between IV characteristics of as deposited and post annealed Cu_2O truncated cubes measured at room temperature in dark, showing that annealing slightly improves the flow of the current through the device. Annealing temperature of 200 °C is chosen based on SEM and XRD analysis shown in Figure 3.16 and 3.17, respectively, which shows that even after annealing, Cu_2O truncated cubes retain their morphology and structural properties. The annealing step is to ensure removal of Schottky barriers that may be present between metal-semiconductor contacts.

Figure 6.2 b) presents a comparison between IV characteristics of post annealed Cu_2O truncated cubes measured at room temperature in dark and in CWL to see if Cu_2O tc show photoconductivity. However, as observed, visible light irradiation does not affect the IV characteristics of Cu_2O truncated cubes. This is because Cu_2O truncated cubes do not show any absorption in visible light wavelength range from 400 nm to 700 nm, also seen in Figure 3.17 b).

Gas sensing properties

As explained before, oxygen adsorption and desorption plays and important role in determining gas sensing characteristics of a sensor. We first study the response and recovery of the Cu_2O truncated cubes to O_2 with N_2 as a carrier gas. Figure 6.3 demonstrates that upon exposure to different concentrations of O_2 with N_2 at an operating temperature of 150 °C, post annealed Cu_2O truncated cubes show a change in current that corresponds to O_2 concentration, i.e, current increases for increasing O_2 concentration in the atmosphere. Since the oxygen exposure was for a short period of time (300s), similar to CuO bundles, the Cu_2O truncated cubes sensor could not achieve a saturation in current. Also due to short period of nitrogen exposure after each oxygen exposure, the Cu_2O truncated cubes sensor did not get sufficient time for achieving a full recovery of base current. This leads to a much larger base line shift in the current, clearly observed in the Figure 6.3. Like CuO bundles described before, this establishes that current passing through a network of Cu_2O truncated cubes is modulated by surface adsorption and desorption of oxygen, which is a requirement of qualification for a sensor material.

Effect of annealing is also studied on the gas sensing characteristics of Cu_2O truncated cubes and is shown in Figure 6.4. For both, RT and 150 °C operating temperature, annealing is seen to reduce the current flowing through the device along with a slight reduction in the response to 20.9% O_2. The reduction in the overall current flowing through the device could be due to overall improvement in the crystal structure of Cu_2O in turn reducing the number of defects which contribute to the concentration of charge carriers. Reduction in number of defects due to annealing may also explain reduction in sensor response observed. Like CuO bundles, Cu_2O truncated cubes showed an overall high current at higher operating temperature of 150 °C than RT for both, as deposited and post annealed samples. On observing the Figure 6.4, we can also see that the Cu_2O truncated cubes device has an incomplete recovery. One can argue that if given more time to recover, the current in the device can reach to an original state in the carrier gas. However, observing recovery curves in Figure 6.4 b), we see that the current starts to increase slightly in long term, than expected decrease. This could be an indication that the device recovered as much as it could and some amount of oxygen that was adsorbed during sensing response was trapped in

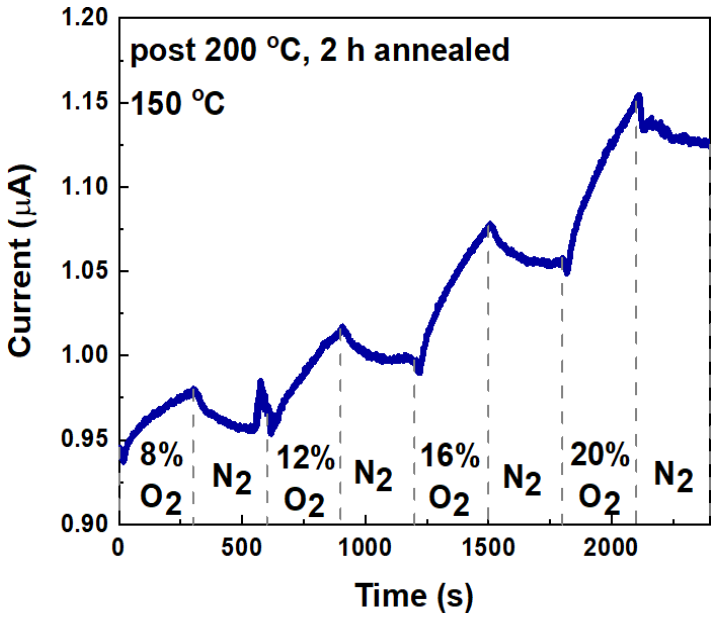

Figure 6.3: Demonstration of change in current through post annealed Cu_2O truncated cubes due to oxygen adsorption and desorption measured at 150 °C operating temperature with a 10 V bias.

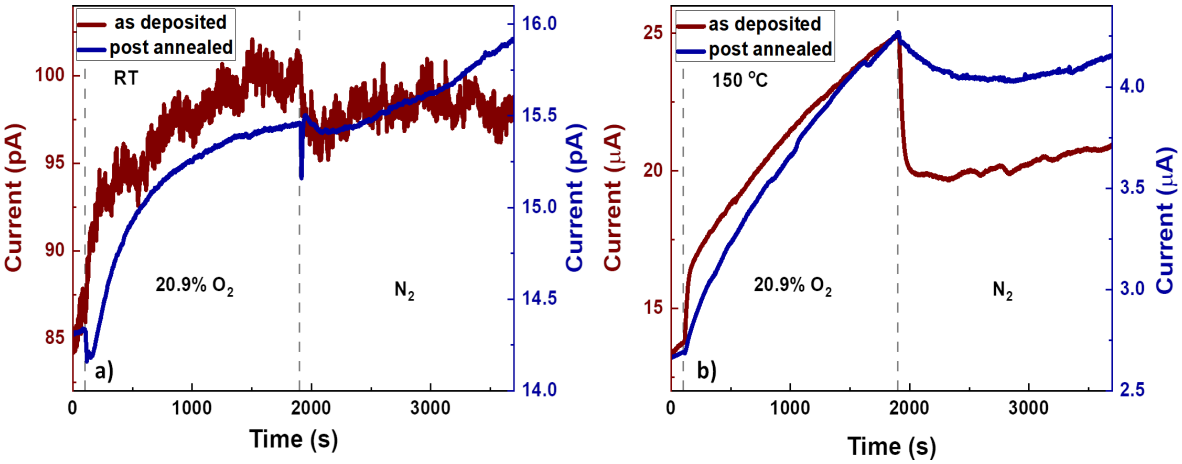

Figure 6.4: Figure demonstrating response and recovery to 20.9% O_2 of as deposited and post annealed Cu_2O truncated cubes measured at a) RT and b) 150 °C at a voltage bias of 10 V.

the material causing a permanent shift in the current flowing through the device.

Incomplete recovery and trapping of adsorbed oxygen indicate that Cu_2O truncated cubes, in the current form, are not ideal for gas sensing application.

3. Abbreviations

AFM - Atomic force microscopy

CWL - Cool white light

eV - electron volt

e-nose - Electronic nose

E_g - bang gap

FWHM - Full Width Half Maximum

I - Current

I_{air} current flowing through the gas sensor in air or base gas

IR - Infra red

I_g - saturation current flowing through the gas sensor in presence of target gas

LED -Light Emitting Diode

LTEL - Long term exposure limit

MFC - Mass Flow Controller

MOx - Metal oxides

mL - milliletres

MLA - mask less aligner

nA - nano amperes

NFs - Nano flowers

nm - nano meter

NPs - Nano particles

NRs - Nano rods

NW - nanowires

PDF - Powder diffraction pattern

ppb - parts per billion

ppm - parts per million

R - Resistance

RT - room temperature

SR - sensor response

SEM - Scanning electron microscope

STEL - Short term exposure limit

sccm - standard cubic centimeter per minute

TEM - Transmission electron microscopy

UV - Ultra violet

V - Voltage

W - Watt

XPS - X-ray Photoelectron Spectroscopy

XRD - X-ray diffraction

t_{90} - response time

t_{10} - recovery time

4. Chemical abbreviations

CuO - Copper oxide

ZnO - Zinc oxide

In_2O_3 - Indium Oxide

$CuSO_4$ - copper sulphate

$Cu(NO)_3$ - copper nitrate

$ZnCl_2$ - Zinc chloride

HMTA - hexamethylenetetramine

$CuCl_2$ - copper chloride

SDS - sodium dodecyl sulfate

$NH_2OH \cdot HCl$ - hydroxylamine hydrochloride

NH_4OH - ammonia

HCl - hydrochloric acid

$CdSe$ - Cadmium selenide

CdS - Cadmium sulphide

Cr_2O_3 - Chromium oxide

Ti - titanium

Au - Gold

SnO_2 - Tin oxide

WO_3 - Alumina oxide

TiO_2 - Tungsten oxide

NO_2 - Nitrogen oxide

NH_3 - Ammonia

H_2O - water vapour

H_2 - hydrogen

CO - carbon monoxide

H_2S - hydrogen sulphide

Cu_2O - Cuprous oxide

CuS - Copper sulphide

Co_3O_4 - Cobalt oxide